

**CHALCOGENIDE INTEGRATED
HOLLOW-CORE OPTICAL FIBERS FOR
INFRARED LIGHT GUIDANCE**

A THESIS SUBMITTED TO
THE GRADUATE SCHOOL OF ENGINEERING AND SCIENCE
OF BILKENT UNIVERSITY
IN PARTIAL FULFILLMENT OF THE REQUIREMENTS FOR
THE DEGREE OF
MASTER OF SCIENCE
IN
MATERIALS SCIENCE AND NANOTECHNOLOGY

By
Asfandyar Khan
December 2022

CHALCOGENIDE INTEGRATED HOLLOW-CORE OPTICAL
FIBERS FOR INFRARED LIGHT GUIDANCE

By Asfandyar Khan

December 2022

We certify that we have read this thesis and that in our opinion it is fully adequate,
in scope and in quality, as a thesis for the degree of Master of Science.

Abdullah Demir(Advisor)

Mustafa Ordu(Co-Advisor)

Bülend Ortaç

Hakan Altan

Approved for the Graduate School of Engineering and Science:

Orhan Arıkan
Director of the Graduate School

ABSTRACT

CHALCOGENIDE INTEGRATED HOLLOW-CORE OPTICAL FIBERS FOR INFRARED LIGHT GUIDANCE

Asfandyar Khan

M.S. in Materials Science and Nanotechnology

Advisor: Abdullah Demir

Co-Advisor: Mustafa Ordu

December 2022

The low-loss light transmission and broad bandwidth of hollow-core negative curvature fibers (NCFs) have a variety of applications in infrared (IR) light guidance, such as chemical detection, biomedical surgery, and laser delivery. Although silica is a material of choice for light guidance in the visible and near-IR spectra, transmission losses increase drastically in the mid-IR region; thus, other mid-IR transparent materials, such as chalcogenide glasses, are potentially preferred to guide the light. In this thesis, various cladding designs of arsenic trisulfide (As_2S_3) and arsenic triselenide (As_2Se_3) chalcogenide NCFs are numerically explored for low-loss transmission in the mid-IR region. A detailed numerical investigation in the optimization of As_2S_3 NCFs with tubular and elliptical cladding elements was performed, and a low-loss ellipse-nested tubular NCF design is proposed for mid-IR guidance. The effect on the transmission loss due to cladding elements of the proposed low-loss As_2Se_3 ellipse-nested tubular fiber design was investigated. Confinement and total loss of all fiber designs were numerically studied, and the single-mode light guidance performance of the proposed low-loss fiber design was explored. The bending loss performance of the fiber was analyzed in the targeted spectrum, and a dispersion control study was carried out to investigate the effect of the primary design parameters on the dispersion performance. A fabrication tolerance study was performed to investigate the effects of common fabrication issues on the proposed design's guidance properties. In the second part of the thesis, NCFs with silica, chalcogenide, and chalcogenide-coated silica cladding elements were numerically investigated for low-loss near and mid-IR transmission. As_2S_3 coated silica NCF was compared to simple silica and simple As_2S_3 fiber to understand the effect of the As_2S_3 coating on the transmission loss of silica NCF. Fabrication of silica NCF through the stack-and-draw technique followed

by micro-coating with As_2S_3 solution was performed to improve the transmission performance of the As_2S_3 coated silica glass-based NCF. Further modifications in the fabrication of the NCFs were realized for a thorough comparison with the numerical investigations.

Keywords: Hollow-core negative curvature fibers (NCFs), Infrared (IR), Chalcogenide, Arsenic trisulfide (As_2S_3), Arsenic triselenide (As_2Se_3), Silica.

ÖZET

KIZILÖTESİ IŞIK İLETİMİ İÇİN KALKOJEN EKİLİ DELİK ÇEKİRDEKLİ OPTİK FİBERLER

Asfandyar Khan

Malzeme Bilimi ve Nanoteknoloji, Yüksek Lisans

Tez Danışmanı: Abdullah Demir

İkinci Tez Danışmanı: Mustafa Ordu

Aralık 2022

Düşük kayıplı ışık iletimi ve geniş bant açıklıklı delik çekirdekli negatif eğrilikli fiberler (NCF'ler), kızılötesi ışık iletiminde kimyasal algılama, biyomedikal cerrahi ve lazer iletimi gibi çeşitli uygulamalara sahiptir. Silika, görünür ve yakın kızılötesi spektrumlarında düşük kayıplı ışık iletimi için tercih edilen bir malzeme olmasına rağmen, orta kızılötesi bölgesindeki iletim kayıpları yüksektir. Bu nedenle kalkojen camlar gibi diğer orta kızılötesi şeffaf malzemeler bu bölgede ışığı iletmek için tercih edilmektedir. Bu çalışmada, orta kızılötesi bölgesinde düşük kayıplı iletim için arsenik trisülfid (As_2S_3) ve arsenik triselenit (As_2Se_3) kalkojen NCF'lerin çeşitli tasarımları, sayısal olarak gerçekleştirildi. Tezin ilk bölümünde, As_2S_3 NCF'lerin boru biçimli ve eliptik kaplama elemanları ile optimizasyonunda ayrıntılı bir sayısal araştırma yapılarak orta kızılötesi iletimi için düşük kayıplı elips yuvalanmış boru biçimli bir NCF tasarımı önerildi. Önerilen düşük kayıplı As_2Se_3 elipsin iç içe boru şeklindeki fiber tasarımının kaplama elemanlarından kaynaklanan iletim kaybı üzerindeki etkisi incelendi. Tüm fiber tasarımlarının sınırlandırılması ve toplam kayıp sayısal olarak çalışılarak önerilen düşük kayıplı fiber tasarımının tek modlu ışık iletime performansı araştırıldı. Önerilen tasarımın eğilme kaybı performansı hedeflenen spektrumda analiz edildi. Birincil tasarım parametrelerin dispersiyon performansı üzerindeki etkisini araştırmak için bir dispersiyon kontrol çalışması yapıldı. Önerilen tasarımın üretime uygunluğunu belirlemek için bir üretim tolerans çalışması yapıldı. İkinci bölümde, silika, kalkojen ve kalkojen kaplı silika kaplama elemanları içeren NCF'lerin düşük kayıplı yakın ve orta kızılötesi iletimi için sayısal olarak incelendi. As_2S_3 kaplamanın silika NCF'nin iletim kaybı üzerindeki etkisini anlamak için As_2S_3 kaplı silika NCF, basit silika ve basit As_2S_3 fiber ile karşılaştırıldı. As_2S_3 kaplı silika cam bazlı NCF'nin iletim performansını geliştirmek için dizme ve çekme tekniğiyle

ve ardından As_2S_3 çözeltisiyle mikro kaplama yoluyla silika NCF'nin üretimi gerçekleştirildi. Sayısal araştırmalarla kapsamlı bir karşılaştırma için NCF'nin üretiminde değişiklikler yapıldı.

Anahtar sözcükler: Delik çekirdekli negatif eğrilikli fiberler (NCF'ler), Kızılötesi (IR), kalkojen, Arsenik trisülfür (As_2S_3), Arsenik triselenit (As_2S_3), Silika..

Acknowledgement

Foremost, I would like to express my sincere gratitude to my supervisor, Dr. Mustafa Ordu, for his continuous support, guidance, and enthusiasm throughout my Master's studies. I sincerely thank him for trusting me and taking me into Contemporary Fibers Laboratory (CFL) at a time when I had very limited knowledge in the field of optical fibers, and later for his guidance and important feedback whenever we had a scientific problem, and for the motivation whenever I was in need. I learned the science of optical fibers from him, and I found him someone from whom I learned the ability to work in a group with people from different backgrounds and disciplines and the ability to have a good balance of work and social life.

I would like to thank my thesis committee: Asst. Prof. Abdullah Demir, Asst. Prof. Bülend Ortaç and Prof. Hakan Altan, for their constructive comments and feedback. I especially would like to thank Asst. Prof. Bülend Ortaç and his group members for their continuous support and help during the fiber fabrication part of this thesis work. They have been sincerely helpful throughout my research work by providing the necessary equipment, guidance, and help needed for fiber fabrication.

I would like to acknowledge the support from UNAM, Bilkent University, and TÜBİTAK for providing an amazing research environment and financial support to carry out my Master's research work successfully. I sincerely thank all my fellow CFL group members; Md Kawsar Ahmed, Md Mehdi Hasan, Mahmudur Rahman, Ali Bagheri Behboud, Md Sazid Bin Sadeque, Muhammad Zain Siddiqui, Abdul Aziz Khan, Mustafa Waqar Syed, Arda Kurucu, Berke Özyalın, Ceren Dilsiz, Mahmut Şahin, Cihat Kürşat Kalkan, Ilgın Albasar, Manahil Noor, Murat Barış, Deniz Berk Onuralp and Gökten Yılmaz for an amazing time we had together, and for their sincere help whenever it was needed. I especially would like to thank Md Sazid Bin Sadeque for being a supportive partner in this project.

I want to thank all my friends back in school and at Bilkent University, who

always supported me, trusted me, and who were always there whenever I needed them. I would like to especially thank Azhar, Abbas, Saad, Talha, Azad, Adeel, Uzair, Mohsin, Yahya, Sanghar, Muzaffar, Nigel, Majeed, Faisal, Waqar Khan, Sahto, Abir, Warraich, Ahsan, Mansoor, Hilal, Ahmed Katia, Talha, Omar, Faruk, Waqar, Reham, Robab, and Maryam for their wonderful friendship and making this stay at Bilkent University more fun. I would like to mention dear Madelyn for the constant support and trust throughout my time here. I know I will always look up to these friends whenever I need them, and I know that they will always be there.

Above all, I would like to thank my dear parents, Sannaullah and Bibi Sabira, and my siblings, especially my brother, Zabiullah, for always supporting me, standing beside me, and always being there whenever I needed them. Whatever I have achieved so far, it would not have been possible without them, especially my dear mother. I thank you all for everything.

Contents

- 1 Introduction** **1**
- 1.1 Negative Curvature Fibers (NCFs) 3
- 1.2 Applications of NCFs 6
 - 1.2.1 Telecommunication System 7
 - 1.2.2 Gas Sensing and Mid-Infrared Fiber Lasers 7
 - 1.2.3 High-power Beam Delivery 8
 - 1.2.4 Micromachining 8
 - 1.2.5 Surgical Procedures 8
- 1.3 Mid-Infrared NCFs 9
 - 1.3.1 Comparison of Silica and Soft-glasses Based NCFs 9
 - 1.3.2 Historical Progress 11
- 1.4 Objective 13
- 2 Theoretical Basis and Simulation Method** **15**

2.1	Guidance Mechanism	15
2.1.1	Antiresonant Reflection	16
2.1.2	Inhibited Coupling	17
2.2	Simulation Method	17
2.2.1	Model Validation	20
2.3	Numerical Studies	21
3	Arsenic trisulfide (As_2S_3) NCFs	22
3.1	Introduction	22
3.2	Fiber Design	23
3.3	Numerical Results and Discussions	24
3.3.1	Design Optimization	24
3.3.2	Confinement and Total Loss	27
3.3.3	Single-Mode Performance	31
3.3.4	Fabrication Feasibility	34
4	Arsenic triselenide (As_2Se_3) NCFs	36
4.1	Introduction	36
4.2	Fiber Design	37
4.3	Numerical Results and Discussions	38

<i>CONTENTS</i>	xi
4.3.1 Design Optimization	38
4.3.2 Confinement and Total Loss	41
4.3.3 Single Mode Performance	43
4.3.4 Dispersion Control	45
4.3.5 Bending Loss	47
4.3.6 Fabrication Feasibility	48
5 Chalcogenide-Coated Silica NCF	51
5.1 Introduction	51
5.1.1 Guidance Mechanism	52
5.1.2 Numerical Results and Discussions	53
5.2 Fiber Fabrication	58
5.2.1 Preform Preparation	59
5.2.2 Cane Drawing	60
5.2.3 Fiber Drawing	63
5.3 Chalcogenide Coating	64
5.4 Fabrication Challenges and Solutions	65
6 Conclusion	68
A Code	86

List of Figures

1.1	A schematic illustration of two types of HCF: (a) PBGF (b) and Kagome HCF.	2
1.2	Schematics showing three different kinds of possible core-cladding curvature boundaries with their mode profile. Adapted from [27] .	3
1.3	(a) A simple six-tube NCF with a gap between the cladding tubes. (b) a hollow-core NANF showing nodeless nested cladding tubes [39].	5
1.4	An electron microscope image of one of the earliest fabricated chalcogenide glass NCF. Reprinted with permission from [49]. . .	5
1.5	A schematic summarizing various applications of HCFs and their properties [12].	6
1.6	Bulk glass transmittance spectra comparison of silica, fluorides, selenide, sulfide, and tellurides between 1 μm to 27 μm . Adapted from [87].	10
1.7	An illustration showing the historical overview and evolution of different NCF designs in the mid-IR spectrum [26, 34, 38, 45, 48, 49, 50, 86, 90, 93, 101].	11

2.1 Schematics showing the electric field profiles of (a) fundamental core mode, (b) cladding tube modes, and (c) dielectric modes. 16

2.2 A schematic illustration of a six-tube silica NCF showing the (a) cylindrical PML surrounding the fiber cladding structure and (b) a custom meshed NCF showing different optimized mesh parameters employed in different fiber regions. (c) A simulated fiber structure showing the electric field confinement in the fiber core. 18

2.3 Convergence studies for (a) the mesh size parameter and (b) the PML thickness. 19

2.4 Comparison of the calculated confinement and measured loss performance of a silica glass NCF with our numerical model results. Adapted from [22]. 20

3.1 The schematic cross-sectional images of the proposed chalcogenide NCFs with (a) tubular (black outline) and (b) elliptical cladding elements (red outline) and their primary design parameters. Six sets of elements were used for both elliptical and tubular cladding NCFs while maintaining the same core diameter (\varnothing_{core}) and strut thickness (t) for all the designs. 24

3.2 (a) The effect of \varnothing_{nest} to the confinement loss of TNTF for several sizes of \varnothing_{tube} at $10.6 \mu\text{m}$. (b) The change in the confinement loss of the ENTF with the major and minor axis of elliptical nested elements. 25

3.3 (a) Relationship of the confinement loss and ellipticity of cladding elements of SEF. (b) Confinement loss versus nested ellipse minor axis of ENEF with selected major axis. 26

3.4 (a) The comparison of confinement losses for STF, TNTF, and ENTF. The overall performance of the ENTF is more favorable than the other fibers. (b) Electric field contour plots for STF (left) and ENTF (right) show that ENTF strongly confines the field within the core region with the help of additional elliptical nested elements. (c) Contour plots showing the field confinement and light leakage at different wavelengths for ENTF design. 28

3.5 A confinement loss comparison for SEF (cyan), TNEF (navy), and ENEF (blue). ENEF shows the best overall performance and lowest confinement loss at the 10.6 μm among the elliptical cladding designs. 29

3.6 comparison of the confinement loss and total loss (confinement and material losses) of the ENTF at the targeted spectrum. 31

3.7 (a) Confinement loss of the ENTF for the FM and four HOMs. The HOMER is calculated as high as 100. (b) Electric field mode profiles of the FM and three HOMs at 10.6 μm 32

3.8 The effect of changing \varnothing_{core} on the confinement loss of the FM and three HOMs of STF at 10.6 μm 33

3.9 Fabrication errors for (a) the angular position of the cladding elements and (b) the rotation of nested cladding elements. A considerable increase in confinement loss was found when the symmetry of the ENTF was broken. The insets schematically show the fabrication error. 35

4.1	Cross-sectional schematic of the proposed As ₂ Se ₃ chalcogenide 5-, 6- and 7-ENTF with annotated primary design parameters. A constant core diameter (\varnothing_{core}) of 150 μm and strut thickness (t) of 3.2 μm was used for all the elements in the fibers. Here, \varnothing_{tube} is the cladding tube diameter, and a and b are the nested ellipses' major and minor axes.	38
4.2	Parametric optimization of 5-ENTF. Contour plots show (a) the relationship between the γ versus a , and (b) γ versus η . The optimized ranges for the design parameters are indicated with the white dotted lines.	39
4.3	Confinement and total losses comparison for 5-ENTF, 6-ENTF, and 7-ENTF at the targeted spectrum. 5-ENTF offers the best light guidance with lower confinement and total losses than other fibers. The shaded region shows the spectrum where confinement losses are the dominant loss mechanism. The arrow shows the change in the confinement losses when the material absorption is considered for 5-ENTF.	41
4.4	Comparison of the confinement loss of STF, TNTF, ENTf, and DENTF in the proposed mid-IR spectrum.	42
4.5	(a) The confinement losses of the FM and the first four HOMs with the electric field profiles at 10.6 μm are shown on the top. The suppression over the HOMs is found to be around 600. (b) The change in the confinement losses of the FM and HOMs of 5-ENTF with different η of the nested ellipse at 10.6 μm	44

4.6 (a) n_{eff} of the proposed 5-ENTF with different values of the t . (b) GVD curves of the proposed fiber with strut thickness (t) of 3.2 μm to and 3.3 μm . The zero-dispersion point is indicated with the black dotted line, whereas the change in GVD is shown with the black dashed arrow when the strut thickness is changed from 3.2 μm to 3.2 μm . (c) GVD curves of 5-ENTF structure with different γ and (d) major axis of the nested ellipse (a). 46

4.7 (a) The change in bending loss with different bending radii of the proposed 5-ENTF at 10.6 μm . The bending loss decrease with a constant rate after the critical bending radius (R_{cr}) of 28 cm. (b) Confinement loss comparison of the straight fiber with 28 cm and 50 cm bending radii. 48

4.8 Fabrication feasibility study of the proposed 5-ENTF for (a) different sizes of one of the nested ellipses and (b) changing the size of one set of the cladding elements. Both the fabrication error studies investigated are shown schematically in the insets. The dashed rectangular regions indicate the tolerance regions for the proposed 5-ENTF design. 49

5.1 Schematics of the As_2S_3 chalcogenide glass-coated silica NCF with (a) one-sided and (b) double-sided coating of the silica cladding tubes. 52

5.2 A schematic of a one-sided As_2S_3 coated silica hollow-core capillary showing the path the guided light takes at the air-silica glass interface. 53

5.3 A comparison of the total loss of simple As_2S_3 , simple silica, and one-sided As_2S_3 coated silica STF in the proposed mid-IR region. 54

5.4	A comparison of the total loss for TNTF design with simple As_2S_3 , simple silica, and one-sided As_2S_3 coated silica fiber in the proposed mid-IR region.	55
5.5	Total loss comparison of simple As_2S_3 , simple silica, and one and double-sided As_2S_3 coated silica STF in the proposed mid-IR region. The overall total loss of double-sided coated structures is higher than the one-sided structures in the proposed region. . . .	56
5.6	Total loss comparison of simple silica, simple As_2S_3 and As_2S_3 coated silica STF with different coated thicknesses.	57
5.7	A schematic showing different steps employed in the stack-and-draw fabrication technique for NCF.	58
5.8	A schematic of a 6-tube stacked preform. Supporting capillaries are only used at both ends of the preform, as indicated in the schematic, and are not present in much of the preform length. . .	59
5.9	Cross-section images of 6-tube silica glass stacked preform showing the cladding capillaries and the support capillaries used to stack the preform structure firmly.	60
5.10	A schematic showing different parts and components of a fiber drawing tower.	61
5.11	Microscopic images of the unsuccessful (red outline) and successful (green outline) canes drawn from the stacked preform. The center support tube was inserted all along the fiber length to avoid the collapse of the cladding structure.	62
5.12	A schematic cross-section illustrating the pressure applied to the cladding capillaries and core of the cane to draw the final fiber in the draw tower.	63

5.13 A microscopic image of the final fiber drawn from the cane. The cane was first inserted in an outer jacket to provide mechanical strength during the fiber draw. 64

5.14 (a) A microscopic image showing the coating of As_2S_3 solution on the inside of the silica cladding tubes. (b) EDX analysis of the coated solution showing the elemental composition and atomic % of As and S. 65

5.15 Microscopic images showing different fabrication challenges which can potentially occur during the cane and fiber draw of a silica NCF. 65

List of Tables

1.1	A comparison of the recently proposed NCFs at the targeted mid-IR region [26, 34, 38, 45, 48, 49, 50, 84, 86, 90, 91, 92, 93, 103, 104].	12
3.1	Optimized primary design parameters for all the proposed chalcogenide NCFs at 10.6 μm . The parameters are given in micrometer (μm).	27
4.1	The optimized primary design parameters for 5-ENTF, 6-ENTF, and 7-ENTF at 10.6 μm .	40

Chapter 1

Introduction

The conventional solid-core silica optical fibers (SC-SOFs) have been widely used as waveguides for light transmission and have applications in different areas such as telecommunications, guiding high-power lasers, and different sensing purposes, etc. [1, 2]. They consist of a high refractive index material in the fiber core with a low refractive index cladding. Light is guided using the mechanism of total internal reflection in such SC-SOFs. The net effective index of the guided modes in SC-SOFs is between the refractive indices of the material in the fiber core, and the cladding [3]. Hollow-core fibers (HCFs) have attracted massive interest as an alternative way to guide light due to their excellent optical properties and their ability to overcome the limitation posed by conventional solid-core fibers. HCFs have low dispersion, low latency, low nonlinearity, wide bandwidth, and a high optical damage threshold compared to SC-SOFs and thus makes them an ideal type of optical waveguide for many different applications [4, 5, 6, 7]. Since the hollow core region in HCFs mostly consists of air or is sometimes filled with gases or other fluids, with its refractive index almost equal to one, light guidance in HCFs cannot be explained by the conventional guidance mechanisms as in SC-SOFs [8, 9]. In the literature, different theories regarding the light guidance in HCFs have been reported, such as the photonic bandgap effect, the antiresonant reflection guidance mechanism based on the antiresonant reflection optical waveguide (ARROW) model, and the inhibited coupling light guidance

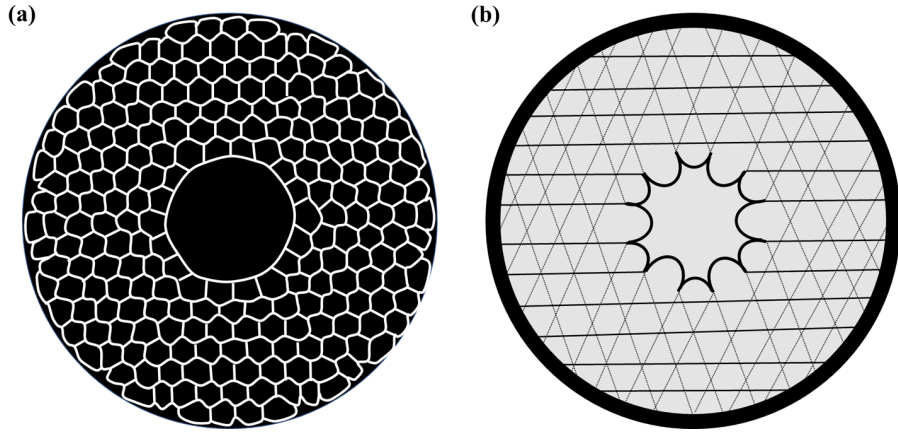


Figure 1.1: A schematic illustration of two types of HCF: (a) PBGF (b) and Kagome HCF.

mechanism [2, 8, 9].

A photonic bandgap fiber (PBGF) consists of a periodic variation of high and low refractive index materials to guide the light in the hollow-core region of the fiber [3]. A bandgap means that light with some specific frequencies cannot propagate because, in PBFGs, the periodic distribution of cladding's refractive index can only guide light in the fiber core, which has a frequency in the frequency range of the bandgap [10]. Light is confined and guided in PBGFs through the photonic bandgap effect and can offer low-loss light transmission with lower nonlinearity, lower latency, and higher damage threshold than SC-SOFs [6, 7, 11]. Figure 1.1 (a) shows a schematic of a PBGF. PBGFs attracted massive interest in the 1990s, with the first hollow-core single-mode PBGF fabricated in 1999, mainly due to their exciting optical properties to overcome the limitations posed by conventional step-index fibers [10, 12]. Although PBGFs have narrow transmission bandwidth, they reduced the transmission loss more than the conventional step-index fibers; but the surface modes at the intersection nodes of the micro-structured cladding membranes limit any further reduction of the transmission loss in PBGFs [13]. These early advances toward a PBGF type of HCFs greatly influenced the field of microstructured optical fibers in the following years.

In addition to the photonic bandgap effect, antiresonant reflection is another

mechanism for light guidance in microstructured fibers with a low-index core and can offer low-loss transmission in a considerably wider bandwidth than the PBGFs [9, 14]. The antiresonant reflection confines light based on the ARROW model, in which each high-index layer circling the low-index core works as a Fabry-Pérot resonator [15]. This mechanism for light guidance was first demonstrated in the Kagome HCF, which consists of a kagome lattice structure of silica membranes acting as the antiresonant reflection layer and thus confining light inside the fiber's hollow-core [4, 16]. Although Kagome fibers have transmission loss higher than the PBGFs, they can offer broadband guidance with tunable dispersion [17, 18, 19]. Figure 1.1 (b) shows a schematic illustration of Kagome HCF [19].

1.1 Negative Curvature Fibers (NCFs)

Further research work on Kagome HCFs led to the conclusion that a negative curvature around the hollow-core region of the fiber can prevent light leakage leading to the development of the most promising type of antiresonant HCFs: negative curvature fibers (NCFs) [9, 20, 21, 22, 23, 24, 25, 26]. Figure 1.2 shows the schematics for three different kinds of curvature which can exist in the cladding of HCFs with a depiction of the mode profile in the fiber core [27]. In negative curvature, the core radial unit vector and the cladding boundary surface normal vector are directed in the opposite direction to each other [20, 24, 25, 27].

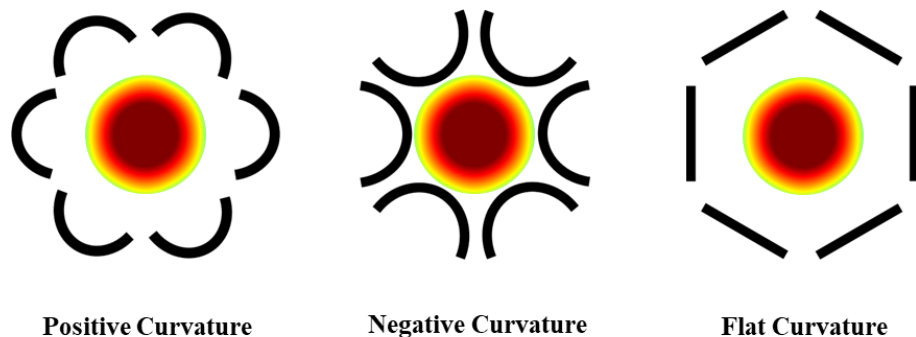


Figure 1.2: Schematics showing three different kinds of possible core-cladding curvature boundaries with their mode profile. Adapted from [27]

Along with reduced transmission loss and many other attractive optical properties of NCFs compared to PBGFs, their simplified fabrication made this category of antiresonant fibers an ideal choice for future development in this field [23, 28, 29]. Careful optimization of the fiber cladding design parameters can result in NCF with extremely low transmission loss. Various simple and advanced NCF structures have been investigated and proposed in the literature [23, 30, 31, 32, 33, 34, 35, 36]. A schematic illustration of a simple six-tube NCF with a separation between the cladding elements is shown in Figure 1.3 (a). The loss in such NCFs is reduced by placing a gap between the adjacent elements since the cladding nodes, in case of touching elements, will result in additional losses [23]. In the literature, NCFs with different numbers of cladding tubes are studied to investigate the change in transmission loss with the different number of cladding elements [23, 37, 38]. NCFs with nested cladding elements have been reported to have less transmission loss due to stronger confinement of the guided light from both the cladding and nested-cladding structures [23]. A schematic illustration of a Nested Antiresonant Nodeless Fibre (NANF) design which has tubular cladding and nested cladding elements with low loss at different transmission bands, is shown in Figure 1.3 (b) [39]. NCFs not only have low losses but also offer broadband guidance and good single-mode light guidance characteristics than the conventional SC-SOFs, PBGFs, and Kagome HCFs. Detailed analysis of different geometrical and optical properties of NCFs, such as the change in the transmission loss with different cladding structures, single-mode light guidance characteristics, bending loss, and dispersion performance, have been investigated in literature [23, 40, 41].

The absence of periodic cladding structure in NCFs, as found in PBGFs, not only simplifies its fabrication procedure but also expands the material selection set for fabricating such HCF. Although silica is the material of choice for designing low-loss NCFs with wide bandwidth in the visible and near-IR spectrum and has applications in telecommunication, sensing, and nonlinear optics due to their promising transmission properties, their transmission loss increases drastically after a wavelength of $4.5 \mu\text{m}$ and thus result in high attenuation while guiding the light in the mid-infrared (mid-IR) spectrum [21, 42, 43, 44, 45, 46, 47]. Alternative

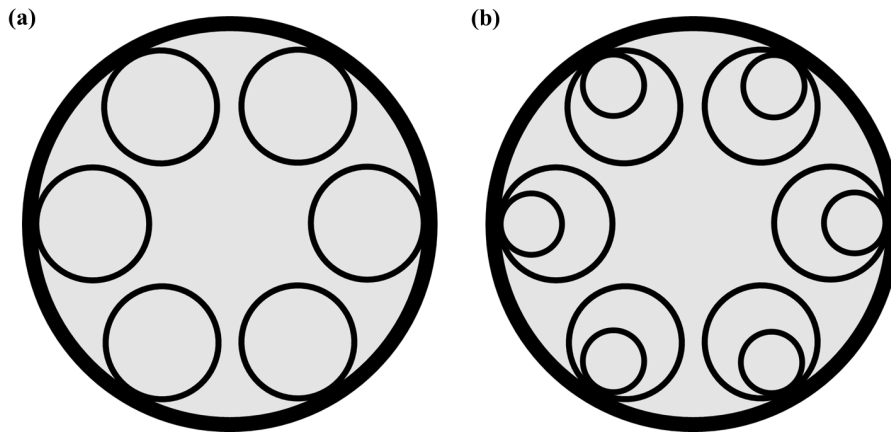


Figure 1.3: (a) A simple six-tube NCF with a gap between the cladding tubes. (b) a hollow-core NANF showing nodeless nested cladding tubes [39].

mid-IR transparent soft glasses such as chalcogenides, tellurite, and fluorides are mostly preferred to fabricate HCFs in the mid-IR region [42, 43, 44, 48, 46]. A $\text{Te}_{20}\text{As}_{30}\text{Se}_{50}$ (TAS) chalcogenide glass NCF for low-loss guidance of CO_2 laser is shown in Figure 1.4 [49].

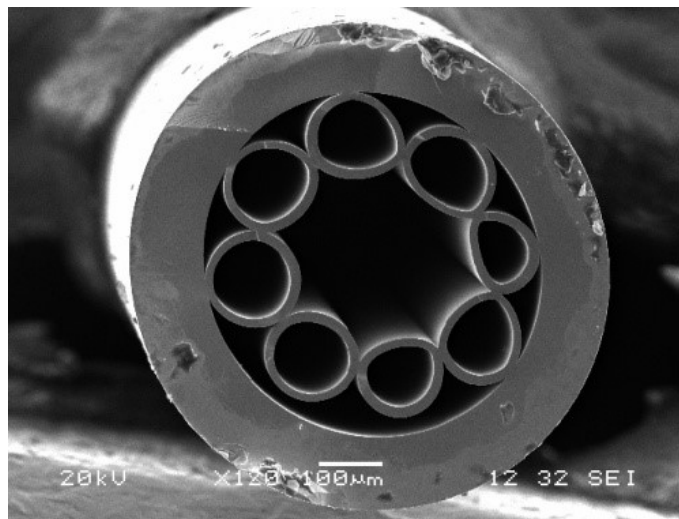


Figure 1.4: An electron microscope image of one of the earliest fabricated chalcogenide glass NCF. Reprinted with permission from [49].

Although in literature, there are numerous names for hollow-core negative curvature fibers, therefore, to avoid any confusion regarding the nomenclature of such HCFs, they will all be collectively referred to as the negative curvature

fibers (NCFs) in this thesis as they all have negative curvature surrounding the fiber core [27, 30, 50, 51, 52].

1.2 Applications of NCFs

NCFs are considered an ideal choice for many different optical fiber-based applications because of their attractive optical properties such as low-loss light transmission, broad bandwidth, low dispersion, high damage threshold and low nonlinearity, and thus have vast applications in different areas such as telecommunication, sensing, high power beam delivery, mid-IR lasers, non-linear optics, micromachining, defense and in surgical procedures as shown in Figure 1.5 [12, 27, 36, 52, 53, 54, 55, 56, 57, 58]. Some of the above-mentioned important applications of NCFs, as reported in different work literature, are discussed in the following section.

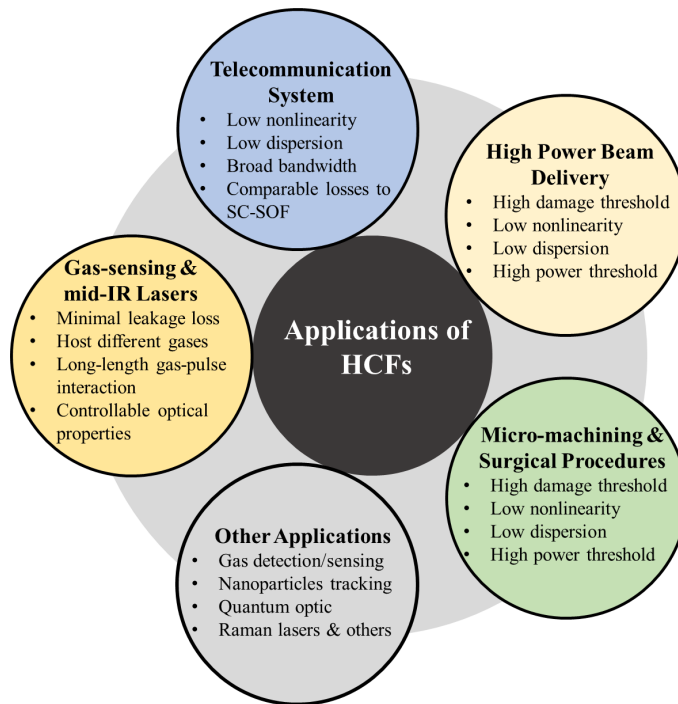


Figure 1.5: A schematic summarizing various applications of HCFs and their properties [12].

1.2.1 Telecommunication System

The transmission loss in conventional SC-SOFs is limited by the high material attenuation of silica and also have high nonlinearity and dispersion than the NCFs [39, 54, 59]. The high attenuation of silica glass limits further reduction in the transmission loss in conventional SC-SOFs [39, 54, 59]. NCFs offer a promising alternative for telecommunication since light is guided in the hollow air-core region, which not only propagates light faster than any other medium resulting in low latency but also have low nonlinearity and low dispersion with broad bandwidth and low attenuation [12, 13]. Several advanced NCF structures have been reported in the literature recording ultra-low loss values at different transmission bands with loss values comparable to the conventional solid-core optical fibers [36, 55, 60]. Recently a 5-tube NCF structure with tubular nested elements has reported a low loss of 0.174 dB/km in the C-band, similar to the loss of commercial SC-SOFs, and considering the ongoing rigorous research in this field, transmission loss can be further improved, and pushed to the theoretical achievable limit in NCFs [36, 60].

1.2.2 Gas Sensing and Mid-Infrared Fiber Lasers

NCFs are the ideal choice for different gas-sensing applications as they can be filled and host different gases [61, 62]. The long-length interaction between gas atoms and molecules with the ultrashort pulse in gas cells allows us to investigate the nonlinear phenomena involved in such gas-filled HCFs. It can detect and sense different gases using different spectroscopy techniques down to even order of parts per trillion (ppt) [54, 58, 61, 62, 63, 64]. The low-loss transmission, wide bandwidth, and high damage threshold of NCFs with the possibility to be filled with different gases favor designing novel high-power mid-IR gas-filled lasers at different wavelengths and optical regions [54, 65, 66]. Such lasers can be developed by carefully designing the fiber structure, its transmission properties, host gases, and the pump laser as reported in different works [58, 65, 67, 68].

1.2.3 High-power Beam Delivery

High damage threshold, low nonlinear effects, and low material loss of NCFs compared to the SC-SOFs make them a preferred choice for high-power beam delivery [69, 70]. NCFs transmitting very high-power nanosecond pulses have been reported in the literature with the promising capability of the fiber to maintain a very good output beam quality [69]. Recent studies on ultra-short pulse propagation in NCFs have reported an increase in the power threshold once the air in the fiber core is replaced and filled with some other inert gases. The ongoing rigorous work in this field may broaden the prospect of using NCFs for high-power beam delivery in different other optical spectrums [70, 71].

1.2.4 Micromachining

NCFs guide the light in the air-core region resulting in low material absorption. They also have lower nonlinearity and a higher damage threshold than the conventional SC-SOFs, and thus can be used to guide different high-power lasers [52, 72]. High-quality micromachining with very good precision and accuracy can be performed if such high-power lasers are guided in NCFs [52, 72]. Micromachining with NCFs result in minimum cracks and destruction of the sample under test, which are not achievable with the conventional solid-core fibers [52].

1.2.5 Surgical Procedures

Optical fibers-based mid-IR lasers are very effective, precise, and safe tools for minimally invasive surgical procedures [56]. They can be precisely directed to the targeted biological tissue for treatment with minimal pressure and damage to other tissues. They are widely preferred because of their small size, handling flexibility, and ability to operate on soft and hard tissues [73]. NCFs can also be potentially used to enhance drug delivery to damaged skin or tissues using laser ablation due to their optical properties not achievable with conventional

SC-SOFs [74, 75, 76].

1.3 Mid-Infrared NCFs

1.3.1 Comparison of Silica and Soft-glasses Based NCFs

SC-SOFs revolutionized the communication infrastructure when the first low-loss fiber was demonstrated in the 1970s [77]. The usage of the SC-SOFs was later expanded to other fields, and SC-SOFs have found applications in a wide variety of areas such as surgery, imaging, and sensing [78, 79, 80]. Due to the rapid increase of infrared absorption in silica, the usage of SC-SOFs are generally limited by the visible and near-infrared (IR) regions; thus, alternative fiber materials are necessary to guide the electromagnetic radiation in the mid-IR spectrum [45, 81]. The low-loss light guidance and broad bandwidth of NCFs have recently drawn interest for applications such as communication, sensing, high-power light delivery, material processing, and nonlinear optics in a broad spectral window, spanning from ultraviolet (UV) to terahertz (THz) [17, 21, 26, 65, 82, 83]. The high material transparency of air as the core medium allows for low-loss light guidance in silica NCFs compared to SC-SOFs in the mid-IR region [6, 84, 85]. Strong light confinement in the hollow-core is achieved through the negatively curved microstructured cladding elements by preventing the coupling of the core-guided modes and the cladding modes [9, 20]. Low spatial overlap and phase mismatch between the core and cladding modes, combined with the anti-resonant effect, is needed to confine the light inside the fiber core [9, 20]. Although the hollow-core structure allows silica-based NCFs to operate partially through the high-loss spectral regions, this advantage ends around $4.5 \mu\text{m}$, after which there is a drastic increase in the material absorption of silica, thus better mid-IR transparent material for the fibers is required for further guidance in the region [21, 23, 43, 47]. Due to their superior material properties, IR transparent glasses such as chalcogenides, tellurides, and fluorides are preferred for designing NCFs in the mid-IR spectrum as shown in Figure 1.6 [44, 45, 86].

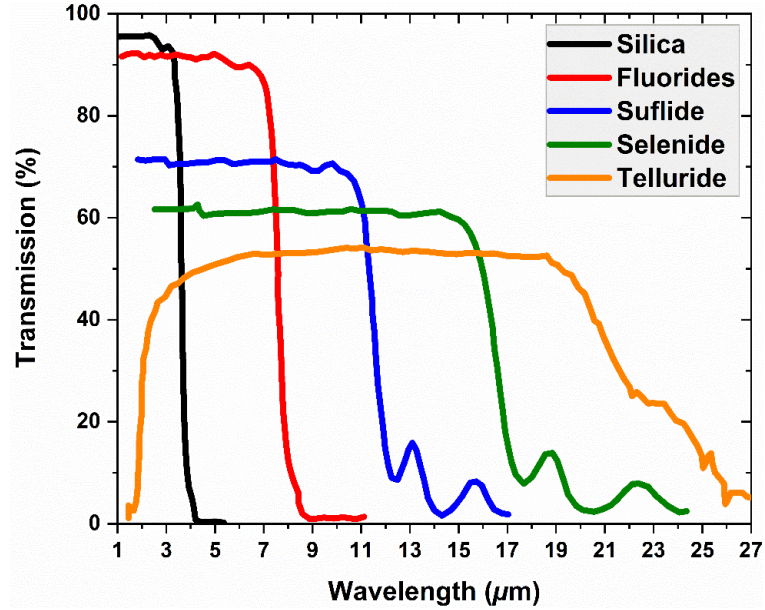


Figure 1.6: Bulk glass transmittance spectra comparison of silica, fluorides, selenide, sulfide, and tellurides between 1 μm to 27 μm . Adapted from [87].

Chalcogenide glasses are the combination of a chalcogen element and an additional element such as arsenic or germanium, and due to their attractive optical properties in the infrared region, have found applications in areas such as infrared detectors, optical sensors and optical fibers [87, 88, 89]. Arsenic trisulfide (As_2S_3) and arsenic triselenide (As_2Se_3) are well-known chalcogenide glasses and have low optical losses with wide material transparency windows in near- and mid-IR regimes. Due to these favorable optical properties of chalcogenide glasses along with good thermal stability, chalcogenide NCFs with various geometrical structures and elemental compositions can be fabricated using different fabrication techniques for mid-IR guidance [34, 45, 49, 84, 86, 90, 91, 92, 93]. NCF with a single ring of tubular cladding elements have recently gathered interest due to their simple design by maintaining low-loss light guidance. Adding the nested elements within the cladding structure significantly affects the losses [23]. In the literature, NCFs with different cladding structures such as tubular, elliptical, conjoined, semi-circular/elliptical, and tube/ellipse nested structures have been investigated in the IR region [23, 30, 33, 34, 55, 94, 95, 96, 97, 98, 99, 100, 101].

1.3.2 Historical Progress

An illustration and design characteristics of recently proposed NCFs in the mid-IR region are summarized in Figure 1.7. Table 1.1 includes both numerical and experimental works on NCFs.

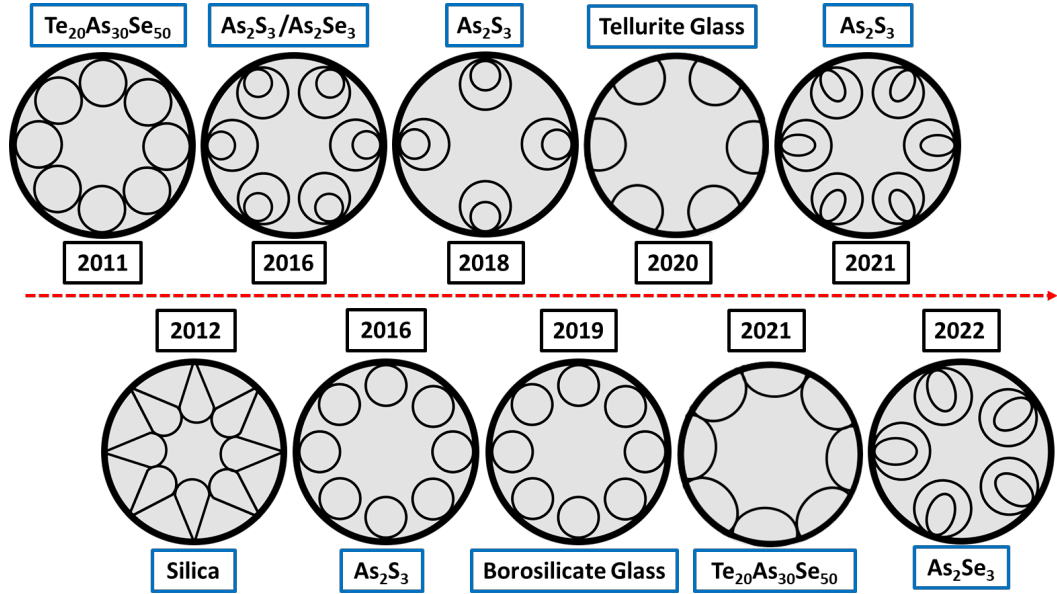


Figure 1.7: An illustration showing the historical overview and evolution of different NCF designs in the mid-IR spectrum [26, 34, 38, 45, 48, 49, 50, 86, 90, 93, 101].

One of the earliest chalcogenide NCF proposed by Kosolapov et al. and fabricated with the stack-and-draw technique demonstrated 11 dB/m measured loss at $10.6 \mu\text{m}$ [49]. As_2S_3 chalcogenide NCF with ellipse nested tubular structure show excellent transmission properties in the mid-IR region [34]. On the other hand, As_2Se_3 chalcogenide glass has better bulk material properties than As_2S_3 in the mid-IR region allowing low-loss guidance, especially at $10.6 \mu\text{m}$ [84, 102]. As_2S_3 tubular NCF with a core diameter range of $700\text{-}900 \mu\text{m}$ proposed by Shiryaev et al. reported a loss of 3 dB/m at $4.8 \mu\text{m}$ [92]. Similar experimental loss values were found by Gattas et al. in a tubular NCF fabricated by the extrusion method [86]. Although lower confinement and total losses were found by Wei et al., the spectral region of interest covers the shorter wavelengths of the mid-IR region [45].

Year/Ref.	Material	ϕ_{core} (μm)	λ (μm)	Confinement loss	Total/Experimental Loss	Application
2011	$\text{Te}_{20}\text{As}_{30}\text{Se}_{50}$	260 & 380	10.6	0.2~0.4 dB/m	~11 dB/m at 10.6 μm	Delivery of the CO_2 laser radiation.
2012	Silica	94	2-4	-	34 dB/km at 3.05 μm	In mid-IR laser sources for spectroscopy and medicine.
2014	As_2S_3	700-900	2-7	-	~3 dB/m at 4.8 μm	Low-loss delivery of mid-IR radiation for different applications.
2016	As_2S_3	~172	2-12	-	~2.0 dB/m at 5 μm ~2.1 dB/m at 10 μm	Low loss guidance near the CO_2 emission bands.
2016	$\text{As}_2\text{S}_3/\text{As}_2\text{Se}_3$	~60	2-6	~0.1 dB/km	~ 10^{-5} - 10^1 dB/km	In different mid-IR applications such as laser delivery.
2017	Silica	~70	1.5-3.35	-	100 dB/km at 2 μm 50 dB/km at 2.45 μm 130 dB/km at 3 μm	For mid-IR applications in military, industry and environmental science.
2018	As_2S_3	~220	10.6	~2.6 dB/km	-	Can be used for delivery of high-power CO_2 laser
2018	$\text{As}_2\text{S}_3/\text{As}_2\text{Se}_3$	300-500	10.6	-	>0.4 dB/km	In CO_2 laser transmission.
2019	Borosilicate glass	122	3.6-5.2	-	~4 dB/m between 5.0-5.2 μm	Cost-effective solution for devices requiring short fiber lengths.
2019	Silica	105 & 110	2.0-5.0	-	18 dB/km at 3 μm 40 dB/km at 4 μm	Can be used for high-power mid-IR laser beam delivery.
2020	Tellurite glass	139 & 187	4.9-6.0	-	~8.2 dB/m at 5 μm ~4.8 dB/m at 5.6 μm ~6.4 dB/m at 5.8 μm	In beam delivery from a CO laser.
2021	$\text{Te}_{20}\text{As}_{30}\text{Se}_{50}$	~217	2-12	-	~1 dB/m at 7.5 μm	-
Our work 2021	As_2S_3	150	9-12	~0.287 dB/km	~115 dB/km at 10.6 μm	Low-loss delivery of mid-IR lasers such as CO_2 laser
2021	$\text{Te}_{20}\text{As}_{30}\text{Se}_{50}$	-	1-12	-	-	Can be used in many chalcogenide glass-based optical devices
Our work 2022	As_2Se_3	150	9-12	~0.39 dB/km	~4.61 dB/km at 10.6 μm	Low-loss delivery of mid-IR lasers such as CO_2 laser

Table 1.1: A comparison of the recently proposed NCFs at the targeted mid-IR region [26, 34, 38, 45, 48, 49, 50, 84, 86, 90, 91, 92, 93, 103, 104].

Furthermore, sub-1 dB/km total loss was calculated for chalcogenide NCF with large core diameters (500 μm) [84]. Less interaction of the guided light and microstructured cladding reduces the confinement loss and is found in large-core fibers. However, the overall diameter of fiber becomes too big that practical usage can be challenging. Extrusion has been a successful fabrication method to fabricate such NCFs. Recently, an extruded tellurite six-tube HCF fabricated by Ventura et al. demonstrated a loss of 4.8 dB/m at 5.6 μm [48]. A recent work by Carcreff et al. demonstrated low-loss guidance with a NCF fabricated from a chalcogenide glass preform made with the 3D-printing technique [90]. Along with chalcogenide and telluride glasses, silica and borosilicate-based NCFs have been reported to guide mid-IR radiations. Belardi et al. measured a loss of 4 dB/m at 5.0 μm with an eight-tube borosilicate glass NCF [50]. A record low loss of 0.7 dB/m at 4.68 μm with a very low-loss transmission window between 4.3 and 5.2 μm was reported by Davidson et al., in a seven-tube silica glass NCF [105]. Although silica and borosilicate-based NCFs offer light transmission with attractive mechanical robustness and chemical durability, they mainly cover the shorter wavelengths of the mid-IR region, and they will have high attenuation due to an increase in the material absorption in the longer spectral region of the mid-IR spectrum [26, 43, 87, 106]. The spectral region centered at 10.6 μm is particularly important for the CO₂ laser, a widely used mid-IR light source for various applications such as material processing, surgery, and drug delivery [89, 49]. Rigorous efforts are still in progress to study the impact of different fiber parameters on the guidance performance of NCFs.

1.4 Objective

The rapid increase in the material absorption of silica glass after a wavelength of 4.5 μm restricts its usage as a fiber material in the mid-IR spectrum, which has several vital applications, as stated above. Alternative mid-IR transparent materials are needed to guide the electromagnetic radiation in this region, and chalcogenide glasses are one of the preferred materials for designing NCFs in

this region. This thesis is focused on discussing and proposing novel chalcogenide NCF designs for low-loss guidance in the mid-IR spectrum. As_2S_3 and As_2Se_3 chalcogenide glass NCF designs with different hybrid cladding structures are numerically explored for low-loss transmission in the mid-IR region. Optical properties such as transmission loss, single-model light guidance characteristics, bending loss, and dispersion performance of the proposed low-loss design are numerically explored, and the fiber designs are optimized at $10.6 \mu\text{m}$ for low-loss delivery of CO_2 laser. A six-tube As_2S_3 coated silica NCF is being proposed in this study which can potentially offer low-loss guidance in both near and mid-IR regions. Chalcogenide coating on silica glass-based NCF can offer low-loss transmission in regions where silica glass has high attenuation and thus paves the way for using silica glass NCFs in the mid-IR region. The proposed design is fabricated with the conventional stack-and-draw technique, and the chalcogenide solution is coated using a micro pump inside the cladding tubes. Successful fabrication and characterization of such NCF will enable the usage of such fibers for different applications in the mid-IR region.

Chapter 2

Theoretical Basis and Simulation Method

2.1 Guidance Mechanism

NCFs can remarkably suppress light leakage and guide light with very low transmission loss due to both the antiresonance effect inside the glass and through prevention of coupling of the core mode to the cladding mode due to wavenumber and phase mismatch [19, 107]. The core mode in NCF refers to the mode in which the guided light is confined in the hollow air-core region as demonstrated in Figure 2.1 (a). In contrast, the cladding modes are the modes that mainly exist either inside the hollow cladding elements referred to as the tube modes, as seen in Figure 2.1 (b), or the modes that exist in the dielectric cladding material called the dielectric mode as shown in Figure 2.1 (c). Small mode field overlap due to antiresonance condition and mismatch of wavenumbers or effective indices of the core-guided modes and the cladding modes reduce the coupling between the modes and thus allow for maximum light confinement in NCFs.

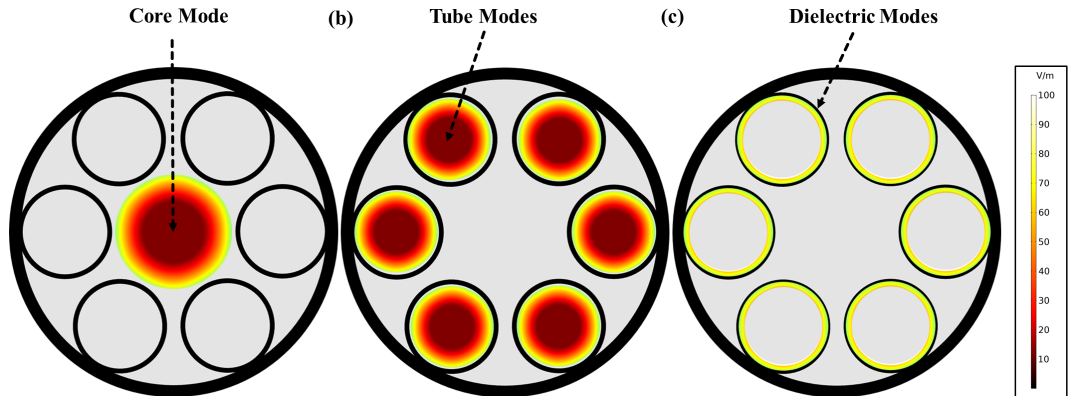


Figure 2.1: Schematics showing the electric field profiles of (a) fundamental core mode, (b) cladding tube modes, and (c) dielectric modes.

2.1.1 Antiresonant Reflection

The ARROW model, where each cladding tube layer acts as a Fabry-Pérot resonator, is used to understand the antiresonant light guidance mechanisms in such NCFs [9, 25]. Constructive interference occurs for resonant wavelengths, and light attenuates and leaks out from the core mode, whereas, for antiresonant wavelengths, destructive interference occurs, and light is confined in the hollow-core region of the NCF [9, 94]. Although the ARROW model can accurately predict the position of the high-loss resonant wavelengths, it does not consider the effect of the negative curvature on losses and thus can not be used to find the exact losses in NCFs. The low-loss transmission window between two high-loss resonant wavelengths in a NCF, which occurs due to strong core and cladding modes coupling, can be expressed with the following equation [9]:

$$\lambda_{res} = \frac{2t\sqrt{n_1^2 - n_0^2}}{m} \quad m = 1, 2, 3... \quad (2.1)$$

where λ_{res} is the high-loss resonant wavelength, t is the strut thickness of the high-index cladding elements, and n_1 and n_0 are the refractive indices of the high-index fiber cladding material, and air respectively. m is a positive integer number representing the resonance order that governs the low-loss transmission windows [9]. For any wavelength other than the high-loss resonant wavelength, λ_{res} , light is mostly guided and confined inside the hollow air-core region with minimum leakage to the outer cladding structure. The net effective refractive

index (n_{eff}) of the mode guiding in the air core is lower than the refractive index of the air, and for a mode to exist and guide in the cladding tubes, its n_{eff} is between that of the air and the microstructured cladding tubes.

2.1.2 Inhibited Coupling

Mode coupling results in an exchange of energy through the leaking of the core mode to the cladding mode leading to high confinement loss in NCFs. Coupling between the core modes and the cladding modes could happen when the cladding modes are near their cutoff frequencies resulting in a reduction in the index difference between the core mode and the cladding mode [53, 107]. Strong phase mismatch and small spatial mode overlap between the core and cladding modes are needed to restrict the light in the air-core region of such NCFs [9, 23, 25]. A weak or no coupling between modes results in maximum light being confined in the core of the NCF, as illustrated in Figure 2.1 (a), whereas a strong mode coupling will lead to the maximum leakage and minimum confinement of light in the core of the fiber due to leakage of energy from the guided modes in the fiber core to the cladding modes as illustrated in Figure 2.1 (b) and Figure 2.1 (c) respectively.

2.2 Simulation Method

Numerical simulations of the micro-structured fibers based on modal analyses were performed in a two-dimensional space dimension using COMSOL Multiphysics, a finite element method-based electromagnetic solver. The eigenmodes of NCFs are calculated using the Wave Optics Module in COMSOL with Electromagnetic Waves, Frequency Domain(ewfd) study. Refractive Index is selected in the Electric Displacement Field in COMSOL to perform the numerical studies. In our simulations, air is considered a non-dispersive material, and a constant refractive index of 1 was used for air in the hollow regions of the NCF. Wavelength-dependent real and imaginary parts of the refractive index are used for material

in the fiber cladding to calculate the confinement loss and to account for the material absorption of the guided light in the total loss calculations. Implementation of necessary boundary conditions is essential to achieve reliable results in numerical studies, and in our model, a circular perfectly matched layer (PML) was implemented at the outer cladding boundary of NCF to optimize the simulation area and time as shown in Figure 2.2 (a) [108]. Scattering boundary condition was used at the outer boundary of the NCF, and a perfect electric conductor layer was implemented whenever half geometry of the fiber was studied to reduce computational complexity and time. Accurate implementation of the mesh parameters is essential to achieve reliable results in COMSOL, and mesh parameters are optimized to reduce the computational load of the simulations. A schematic of a six-tube NCF with optimized mesh parameters in different regions of the fiber structure is shown in Figure 2.2 (b). Figure 2.2 (c) shows a simulated six-tube silica NCF structure with the electric field confinement in the fiber core.

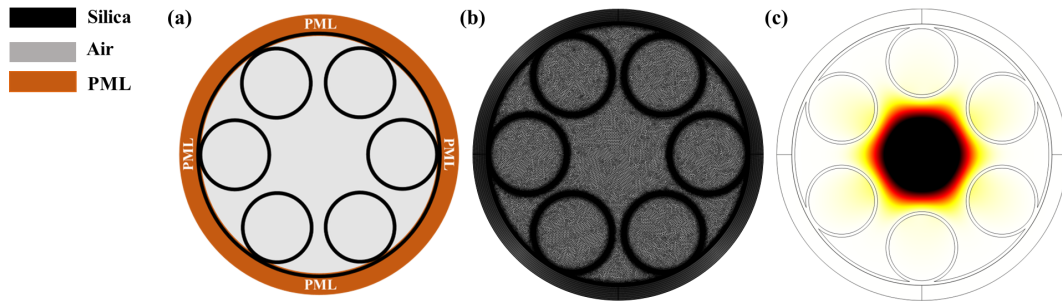


Figure 2.2: A schematic illustration of a six-tube silica NCF showing the (a) cylindrical PML surrounding the fiber cladding structure and (b) a custom meshed NCF showing different optimized mesh parameters employed in different fiber regions. (c) A simulated fiber structure showing the electric field confinement in the fiber core.

Convergence studies were performed to optimize the mesh size parameters and the PML thickness to achieve accurate and reliable results in our models. In Figure 2.3 (a), the relationship between the confinement losses and the maximum mesh size parameter, m , is shown. Here, m values greater than 12 leads to reliable calculations by limiting the maximum mesh size as λ/m . Based on the convergence study, reliable simulation results were obtained when the resolution at the narrow regions of the fiber was greater than 3; therefore, a minimum of

5 elements at the narrow regions of the cladding elements was used for all our numerical models. Moreover, the effect of PML thickness on the confinement losses is shown in Figure 2.3 (b). A PML thickness greater than 10 μm was sufficient for reliable results; thus, we selected 15 μm in all the models. Nevertheless, convergence studies for mesh parameters and PML thickness may vary for different types of fiber models with different design parameters; thus, convergence studies should be carried out whenever the fiber design is changed for reliable and accurate results.

A thorough investigation of the confinement loss that occurs due to the leakage of the guiding light in the fiber core is necessary when the effect of the geometrical configuration of NCF on the fiber losses is sought. The loss contribution due to material absorption is necessary when the transmission performance of the fiber is needed for practical realization. The approach in the following expression is used to calculate the fiber loss (in decibels per meter (dB/m)) [45, 109]:

$$\text{CL} = \frac{40\pi \times \text{Im}(n_{eff})}{\ln(10) \times \lambda} \times 10^6 \quad (2.2)$$

where $\text{Im}(n_{eff})$ is the imaginary part of the n_{eff} and λ is the wavelength of the guided light in micrometer (μm). The relationship between the absorption coefficient (α_{abs}) and extinction coefficient (k) was implemented in the simulations using the material properties of the fiber material.

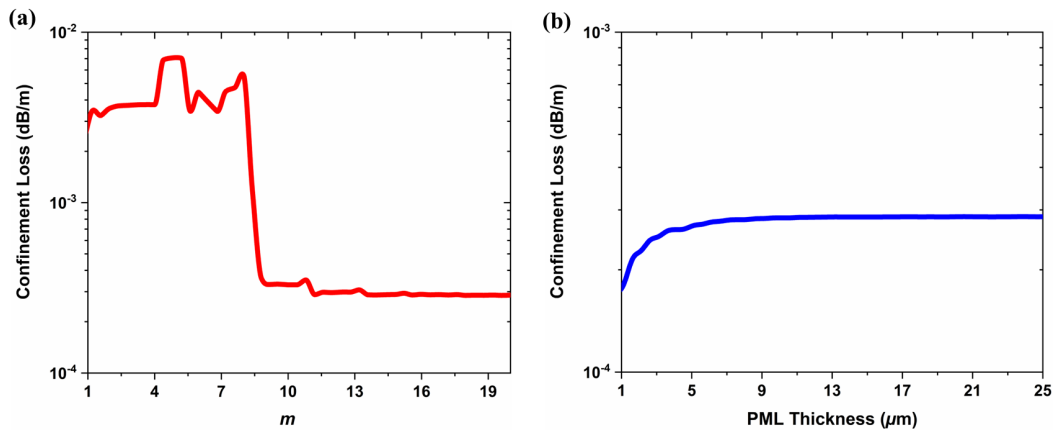


Figure 2.3: Convergence studies for (a) the mesh size parameter and (b) the PML thickness.

2.2.1 Model Validation

The COMSOL model was validated by reproducing numerical results from the literature and then comparing them with the measured transmission loss profiles of fabricated NCFs to realize the closeness of numerical calculations with the practical performance of the fiber [22, 23, 84]. Figure 2.4 compares the calculated and measured loss of a seven-tube silica NCF with our numerical model results [22]. The simulated confinement loss profile from the literature and our numerical model has an excellent match, and a very good agreement is found between the measured loss performance of the fabricated fiber and the numerical simulations, especially close to the low-loss wavelengths between $1.0 \mu\text{m}$ - $1.2 \mu\text{m}$ [22]. The divergence of the calculated confinement loss with the measured loss performance of the fiber at the start and end of the spectrum is due to the presence of multiple high-loss resonant peaks at that region.

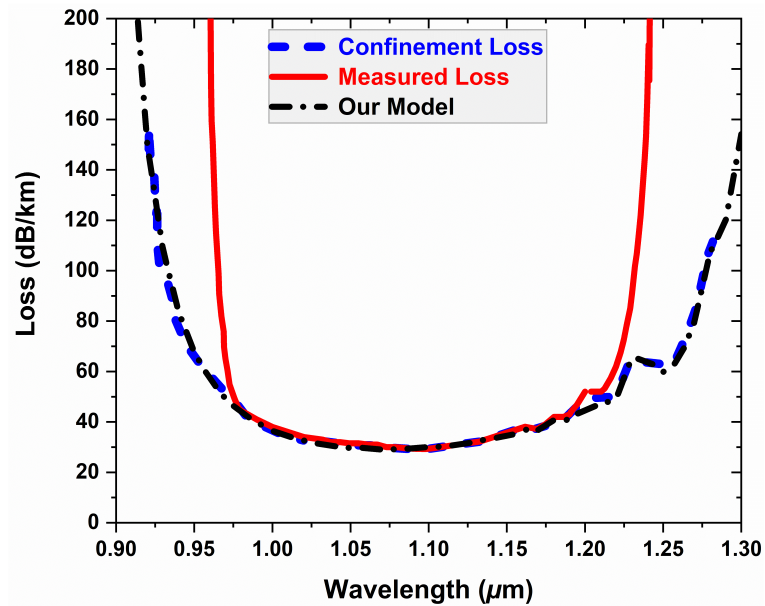


Figure 2.4: Comparison of the calculated confinement and measured loss performance of a silica glass NCF with our numerical model results. Adapted from [22].

2.3 Numerical Studies

Based on convergence studies, optimized mesh parameters and PML thickness was implemented in our numerical models to systemically optimize the primary design parameters of each proposed fiber structure. A confinement loss (also known as leakage loss) study was carried out to understand the effect of NCF geometry on light confinement in the hollow air-core region. A comparative study for total loss, which is the summation of the confinement loss and the loss originated from the guiding light and fiber material interaction, was carried out for the practical realization of our NCF structures. Single-mode light guidance performance was studied to analyze the suppression of higher-order modes (HOMs) in our proposed fiber structures. Moreover, the bending loss performance of our proposed fiber structure was numerically investigated to understand the fiber's sensitivity and mechanical robustness to different bending radii under different environmental conditions. A dispersion control study was performed to show how the design parameters of the fiber structure can be altered to achieve the desired dispersion performance for potential usage in communication applications. A fabrication tolerance study was performed to investigate the effects of common fabrication issues on the guidance properties of the proposed NCFs. In order to achieve a polarization-maintaining NCF, the core symmetry of the fiber should be broken to achieve orthogonal polarization states with high birefringence. Although polarization-maintaining NCFs are required for several vital applications, the numerical studies in this thesis are focused on NCF structures with the same symmetrical core design. More details about all these numerical studies are given in the following sections.

Chapter 3

Arsenic trisulfide (As_2S_3) NCFs

3.1 Introduction

As_2S_3 is a known mid-IR transparent chalcogenide glass with good transmission properties in the mid-IR region. Optical losses of As_2S_3 NCFs with hybrid cladding elements formed by the combination of tubular and elliptical elements are numerically investigated for low-loss operation in the mid-infrared spectrum [34, 101]. Primary design parameters such as the core diameter, strut thickness of cladding elements, cladding/nested tube diameter, and major and minor axes of the cladding/nested ellipse were systemically optimized for all fiber designs [34, 101]. Confinement loss with the proposed ENTF design is several orders of magnitude lower than the confinement losses of tubular/elliptical NCFs in the targeted spectrum [34, 101]. The effect of the material absorption to the total fiber losses was also investigated along with the confinement losses. Suppression on the HOMs by the proposed fiber was numerically studied, and a strong suppression on the HOMs shows that the fiber favors single-mode light guidance [34, 101]. A numerical study of the common fabrication errors during the drawing of such NCFs was carried out to realize the practical performance of our proposed fiber structure. The proposed NCF could be a promising choice for the low-loss guidance of CO_2 lasers that are widely used for various applications spanning

from material processing to surgery.

3.2 Fiber Design

Six different chalcogenide NCF designs that can be grouped in two by the main cladding element shape were modeled [34, 101]. Fibers with tubular elements; a simple-tubular (STF), a tube-nested tubular (TNTF), an ellipse-nested tubular (ENTF), and fibers with elliptical elements; a simple-elliptical (SEF), a tube-nested elliptical (TNEF) and an ellipse-nested elliptical (ENEF) [34, 101]. Arsenic trisulfide (As_2S_3) glass has low optical losses in the mid-IR region and thus was selected as the fiber material with a constant refractive index of 2.4 [84, 86]. Confinement losses for the proposed NCF with variable refractive indices of As_2S_3 were also calculated, and due to minor variation in refractive indices with wavelength, the results were similar to the constant refractive index of 2.4. Thus, we selected a constant refractive index to simplify the models further.

The schematic cross-sectional images of all the proposed chalcogenide fiber geometries, grouped as tubular and elliptical designs, are shown in Figure 3.1 (a) and Figure 3.1 (b) with annotated primary design parameters [34, 101]. All designs have six cladding elements to achieve single-mode light guidance with strong HOMs suppression. Here, the important design parameters are also defined: \mathcal{O}_{core} is the core diameter, \mathcal{O}_{tube} is the cladding tube diameter, and \mathcal{O}_{nest} is the nested-tube diameter. a , b , a_s , and b_s are the major and minor axis of the cladding and nested-cladding ellipses, respectively. A constant \mathcal{O}_{core} of $150 \mu\text{m}$ was used for all fiber designs. According to equation 2.1, a uniform strut thickness, t , of $4.0 \mu\text{m}$ allows low-loss operation in a wide transmission window of the NCF, and thus was selected as the strut thickness and kept constant for both cladding and nested-cladding elements through all the models. Several thicker struts were also found for low-loss operation at the wavelength of $10.6 \mu\text{m}$. However, due to the higher resonance order, the low-loss window becomes narrower with the increased thickness of the struts. Thus, $4.0 \mu\text{m}$ ensures low confinement loss with a wide transmission window.

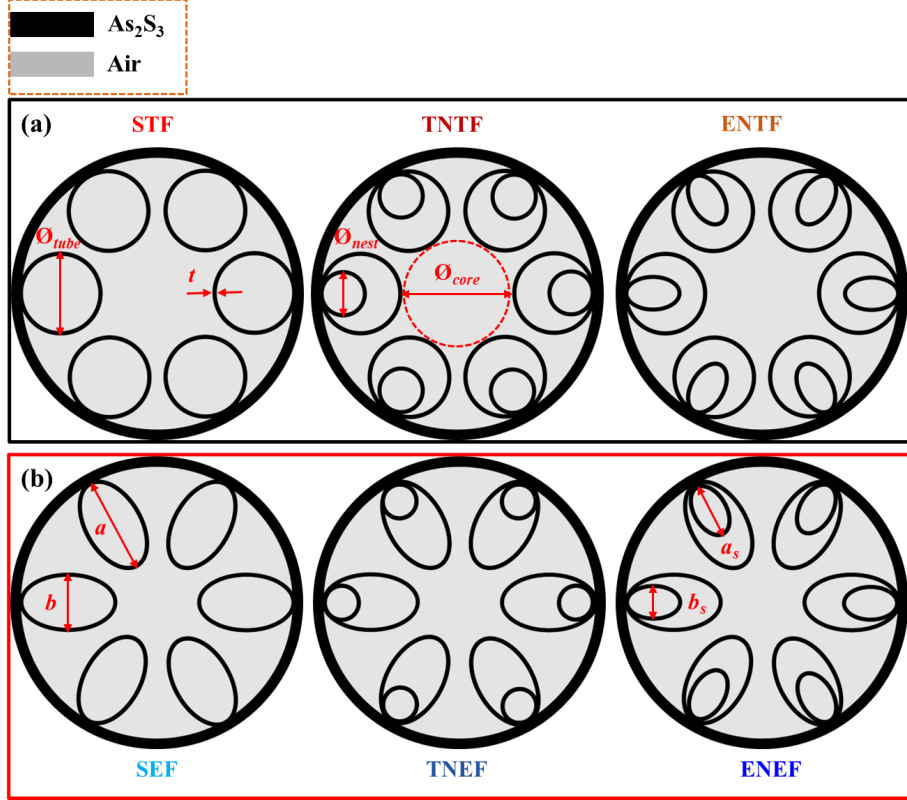


Figure 3.1: The schematic cross-sectional images of the proposed chalcogenide NCFs with (a) tubular (black outline) and (b) elliptical cladding elements (red outline) and their primary design parameters. Six sets of elements were used for both elliptical and tubular cladding NCFs while maintaining the same core diameter (\varnothing_{core}) and strut thickness (t) for all the designs.

3.3 Numerical Results and Discussions

3.3.1 Design Optimization

The primary design parameters of the proposed NCF were systematically obtained by the simulations at $10.6 \mu\text{m}$. The gaps between the tubular cladding elements of the NCFs (designs in Figure 3.1 (a)) were determined for each design to optimize the light confinement. On the other hand, the gaps between the elliptical cladding elements (designs in Figure 3.1 (b)) were calculated and kept the same for the elliptical NCFs. The nested elements of TNTF, ENTF, TNEF, and ENEF were independently investigated, and the nested elements were determined

for each design at the targeted spectrum.

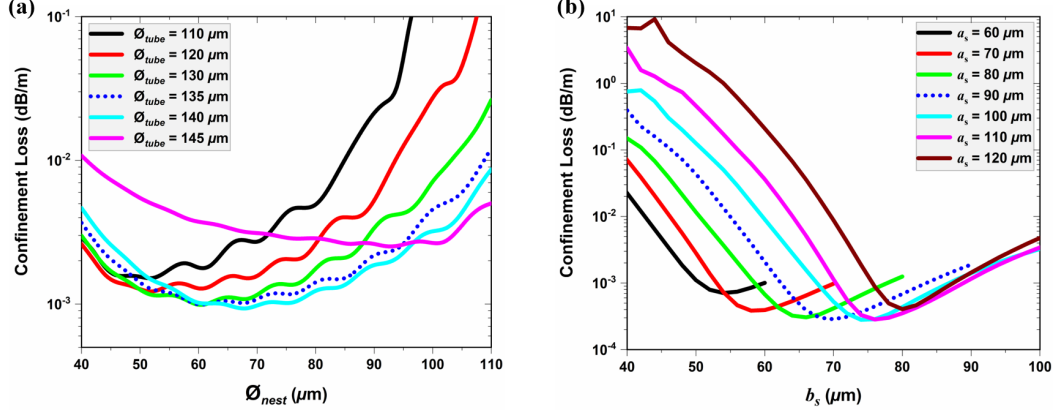


Figure 3.2: (a) The effect of \varnothing_{nest} to the confinement loss of TNTF for several sizes of \varnothing_{tube} at 10.6 μm . (b) The change in the confinement loss of the ENTFF with the major and minor axis of elliptical nested elements.

The confinement losses' dependence on the \varnothing_{tube} of STF was investigated in the range of 50 to 145 μm at 10.6 μm . The tube diameter of 95 μm was found for the lowest confinement loss with the simple tubular structure. Figure 5.4 (a) shows the effect of the cladding tube and the nested tube on the transmission losses of TNTF. The minimum losses were achieved when $\varnothing_{tube} = 135 \mu\text{m}$ and $\varnothing_{nest} = 60 \mu\text{m}$. It is worth mentioning that even though the confinement loss of TNTF with $\varnothing_{tube} = 140 \mu\text{m}$ and $\varnothing_{nest} = 68 \mu\text{m}$ is lower than the selected values at 10.6 μm , the overall losses in the spectral region of 9 μm - 12 μm are higher and show multiple resonant points that splits the low-loss window into smaller bands. Figure 5.4 (b) shows the dependence of confinement losses to the nested ellipses of ENTFF. When $a_s = 90 \mu\text{m}$ and $b_s = 70 \mu\text{m}$, the confinement becomes optimum with minimal resonance points through the targeted spectral region. Moreover, the missing points of incomplete lines are the values that the b_s becomes larger than the a_s of the nested elements. It is important to mention that the investigation of ENTFF was focused on the designs with the major axis of nested ellipses directed to the fiber center. Therefore, the simulations did not cover the fiber geometries where $b_s > a_s$. Also, the confinement losses of ENTFF rapidly increase due to the formation of additional coupling points for the guiding light when $b_s > a_s$.

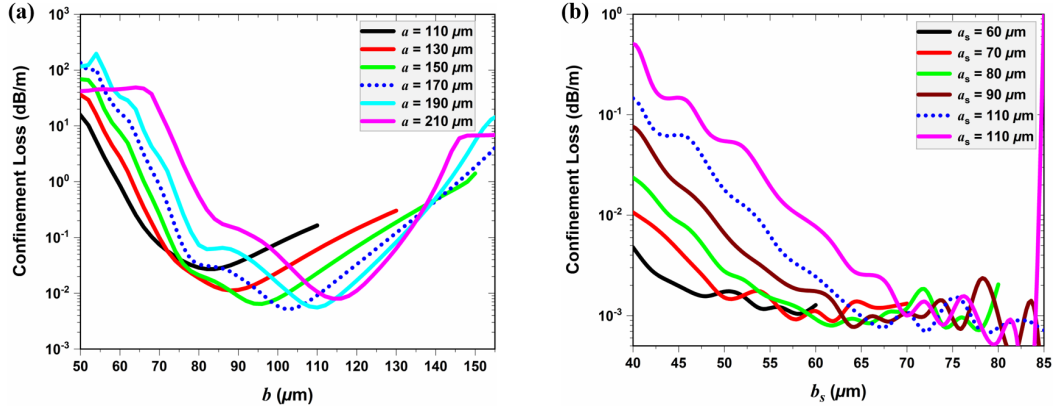


Figure 3.3: (a) Relationship of the confinement loss and ellipticity of cladding elements of SEF. (b) Confinement loss versus nested ellipse minor axis of ENEF with selected major axis.

In the case of the NCFs with the elliptical cladding elements, the transmission properties alter positively with the help of the oval-shaped elements around the fiber core. Figure 3.3 (a) shows the confinement losses against the nested-tube ellipticity for the SEF. The minimum confinement loss was found with an optimal value of a and b , as 170 μm and 104 μm , respectively. The optimal \mathcal{O}_{nest} for the TNEF was found to be 58 μm by keeping the elliptical elements the same as SEF. The dependence of confinement losses to the nested ellipse of the ENEF is shown in Figure 3.3 (b). At 10.6 μm , the minimum confinement loss was achieved, when a_s and b_s were selected as 100 μm and 68 μm , respectively. Although some greater b_s values show improved confinement, the resonance distorts the transmission through the targeted spectrum. Moreover, an increase in confinement losses of the ENEF is visible when the values of b_s become similar to a_s . This is due to the additional resonance caused by overlapping the nested ellipse and cladding ellipses. Table 3.1 summarizes the optimized primary design parameters obtained in this study for the wavelength of 10.6 μm . All the fibers are designed with As_2S_3 and have the same \mathcal{O}_{core} and t .

<i>Parameter</i>	\varnothing_{tube}	\varnothing_{nest}	a	b	a_s	b_s
<i>Design</i>						
STF	95	-	-	-	-	-
TNTF	135	60	-	-	-	-
ENTF	140	-	-	-	90	70
SEF	-	-	170	104	-	-
TNEF	-	58	170	104	-	-
ENEF	-	-	170	104	100	68

Table 3.1: Optimized primary design parameters for all the proposed chalcogenide NCFs at 10.6 μm . The parameters are given in micrometer (μm).

3.3.2 Confinement and Total Loss

A comparative study for confinement loss with different geometrical configurations of the NCFs is important when the effect of NCF geometry to the guided light is sought. On the other hand, a comparative study for total loss, which is the summation of the confinement loss and the loss originated from the guided light and fiber material interaction is essential to anticipate the loss performance of the fiber for fabrication feasibility. A comparison of the confinement losses of the three tubular NCFs in the mid-IR region is shown in Figure 3.4 (a). The confinement losses of STF, TNTF, and ENTF were calculated as 142 dB/km, 0.975 dB/km, and 0.287 dB/km, respectively, at 10.6 μm . Among tubular designs, ENTF shows the best guidance performance at the design wavelength by the effect of nested ellipses. As it can be seen from the electric field contour plots depicted in Figure 3.4 (b), the percentage of the electric field coupled to the outer chalcogenide cladding is considerable for STF. On the other hand, in the case of fibers with nested elements (ENTF), the field intensity at the outer cladding is reduced by keeping the light in the core, and thus a significant reduction of the confinement loss is achieved, as shown in Figure 3.4 (a) [23].

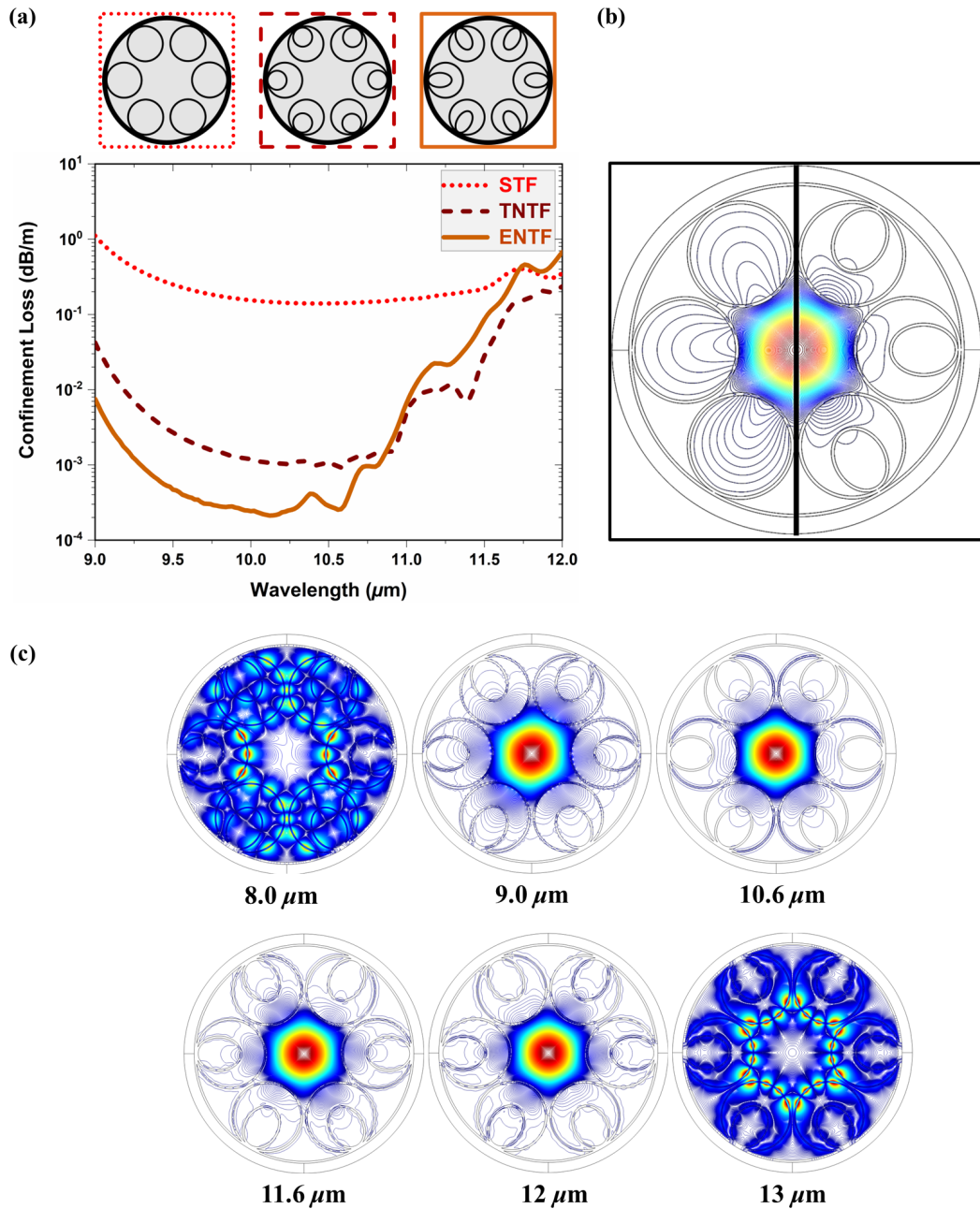


Figure 3.4: (a) The comparison of confinement losses for STF, TNTF, and ENTF. The overall performance of the ENTF is more favorable than the other fibers. (b) Electric field contour plots for STF (left) and ENTF (right) show that ENTF strongly confines the field within the core region with the help of additional elliptical nested elements. (c) Contour plots showing the field confinement and light leakage at different wavelengths for ENTF design.

For an explicit comparison, we simulated STF and ENTF with the same tube diameter ($140 \mu\text{m}$). The result for the optimum \varnothing_{tube} of STF, $95 \mu\text{m}$, shows similar field patterns. Thus, the nested elements are the main reason behind the difference in the losses between the two designs. Figure 3.4 (c) shows the electric field confinement and light leakage from the fiber core at different wavelengths of ENTF design. The confinement of the guided light is maximum at the centered wavelength of $10.6 \mu\text{m}$, and the light leakage from the core to the outer cladding is maximum at the high-loss resonant wavelengths of $8 \mu\text{m}$ and $13 \mu\text{m}$, as can be seen from the contour plots in Figure 3.4 (c).

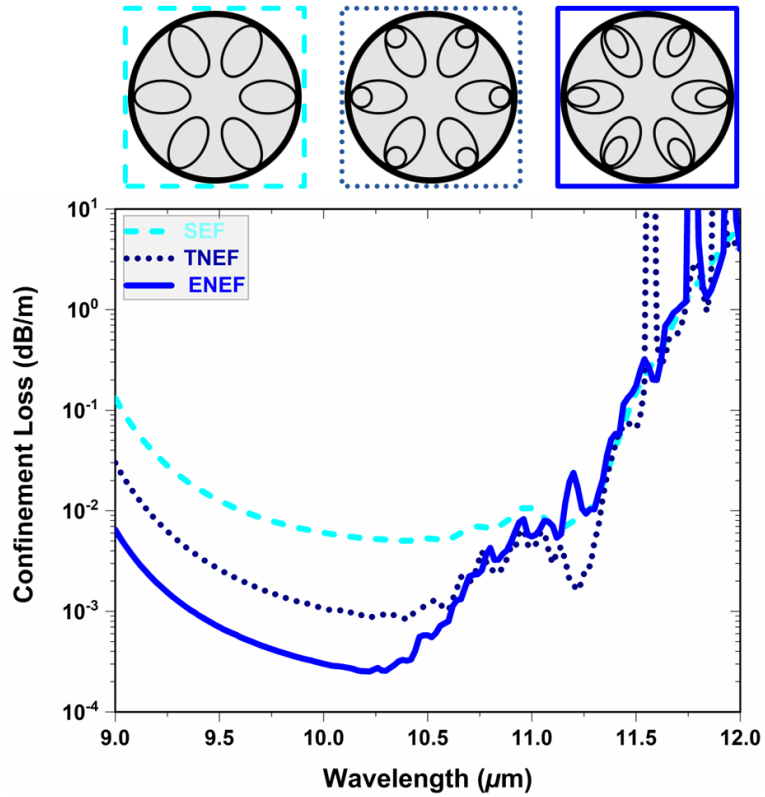


Figure 3.5: A confinement loss comparison for SEF (cyan), TNEF (navy), and ENEF (blue). ENEF shows the best overall performance and lowest confinement loss at the $10.6 \mu\text{m}$ among the elliptical cladding designs.

A comparison of the confinement losses of SEF, TNEF, and ENEF for the targeted spectrum is shown in Figure 3.5. ENEF shows the lowest confinement loss at the design wavelength, and the loss was calculated as 0.798 dB/km .

The confinement losses of TNEF and SEF were found as 1.01 dB/km and 5.28 dB/km, respectively. Even though the TNEF has comparable loss performance with ENEF after 10.6 μm , ENEF has the lowest confinement loss with less resonance in the targeted spectral region. It is worth mentioning that the simple elliptical structure performs better than the simple tubular by the extended strut length surrounding the hollow core. Among the six proposed chalcogenide NCFs, ENTTF provides the lowest confinement loss, two orders of magnitude less than simple tubular/elliptical structures, and approximately one order of magnitude less than nested designs within the studied spectral region. Although the addition of nested elements in elliptical cladding fibers decreases the confinement losses, the overall difference in loss values between the simple and nested structures is much more significant in tubular cladding NCFs, as can be seen in Figure 3.4 (a) and Figure 3.5.

The losses originated by material absorption become essential, especially at the wavelength regions where the material's transparency decreases. Confinement loss study excludes the interaction of the material and the guiding light, and although As_2S_3 is a transparent material within the targeted spectral range, the calculation of losses caused by the material absorption is beneficial to predict the total losses of the proposed design for any experimental demonstration. The total loss, defined as the summation of confinement and material losses, is considered in this section. The relationship between the material absorption coefficient (α_{abs}) and the extinction coefficient (k) was used to include the material absorption of the chalcogenide glass used for the fiber material in the models [23, 34, 110]. Furthermore, the calculated total losses were also verified by the method in [45, 109]. The bulk material losses of As_2S_3 were found as 180 – 480 dB/m between 9 -12 μm . The transmittance of As_2S_3 varies in the targeted spectrum; therefore, constant refractive indices were not used in the total loss calculations. Figure 3.6 compares confinement losses and total losses, stating that the effect of the material absorption within the total loss is substantial. The total loss at 10.6 μm is 115 dB/km, whereas the confinement loss is only 0.287 dB/km, around three orders of magnitude difference. Lastly, it is worth mentioning that, even though transmission of As_2S_3 decreases after 10.6 μm , the ENTTF losses are lower than

the bulk material losses. This shows the advantage of using NCFs for guidance at the lossy regions [86, 110].

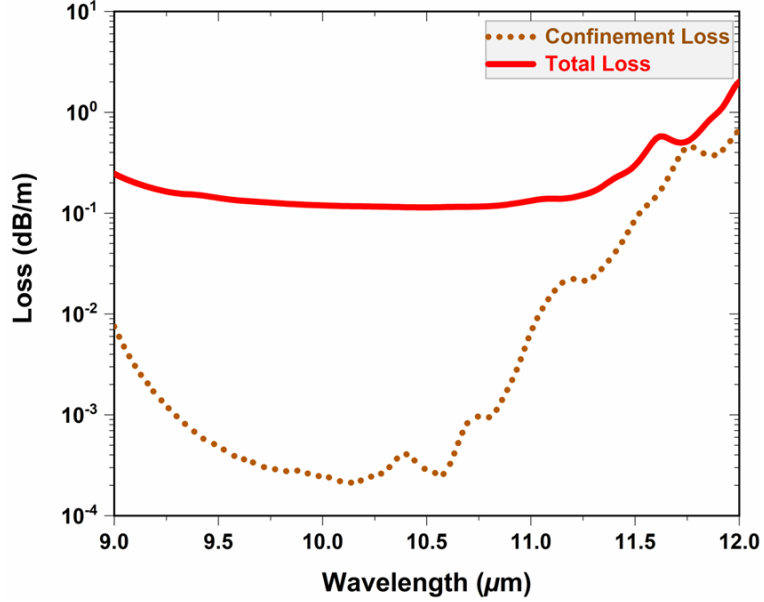


Figure 3.6: comparison of the confinement loss and total loss (confinement and material losses) of the ENTTF at the targeted spectrum.

3.3.3 Single-Mode Performance

In step-index SC-SOFs, the Normalized Frequency Parameters (V-number) determine the single-mode and multi-mode characteristics of the fiber; in contrast, in NCFs, the higher-order mode extinction ratio (HOMER: the ratio of the confinement loss of first HOM and FM) defines the single-mode light guidance performance of the fiber. HOMER shows the light leakage from the HOMs compared to the FM, and a NCF can effectively guide light with single-mode when the HOMER is greater than 10 [111]. Single-mode light guidance performance of the proposed ENTTF design was investigated, and the confinement losses of the core-guided fundamental mode (FM) and the first four HOMs were calculated.

Figure 3.7 (a) shows the confinement losses of the FM and the first four HOMs, namely: HE_{11} , TE_{01} , $HE_{21_{even}}$, and $HE_{21_{odd}}$, and TM_{01} . HOMER was found as

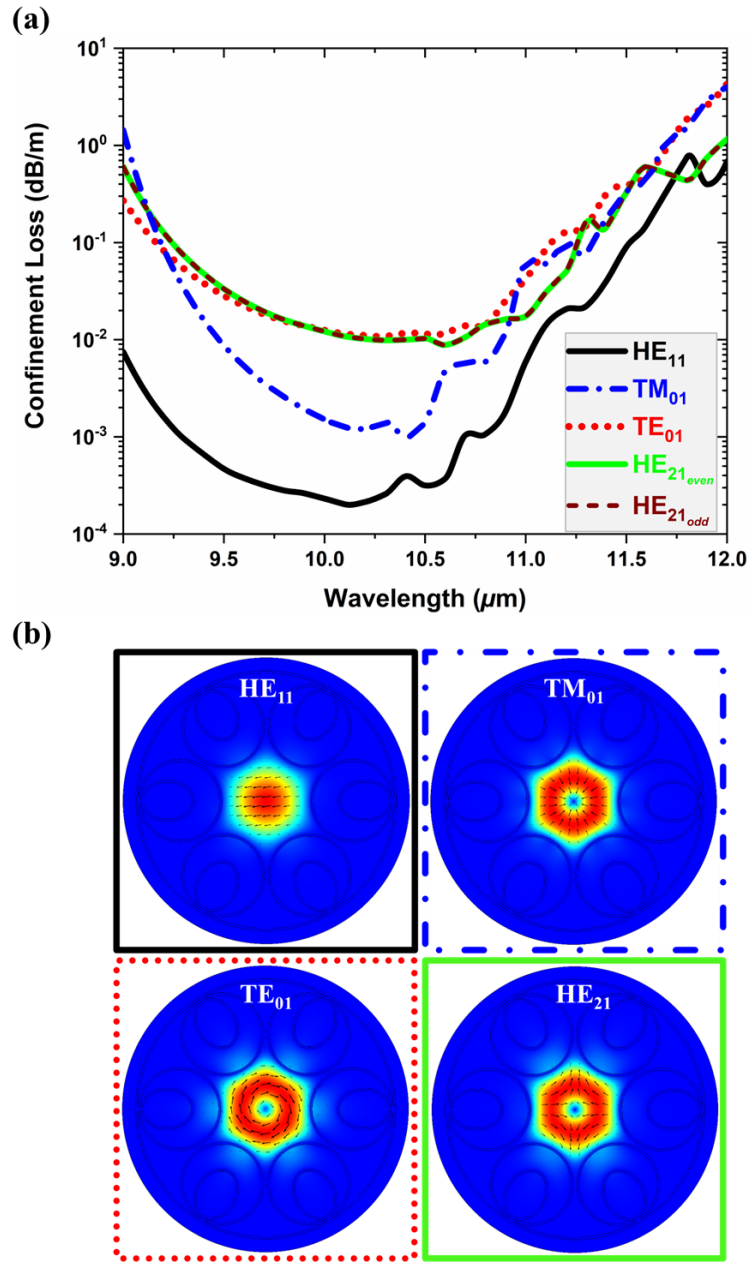


Figure 3.7: (a) Confinement loss of the ENTF for the FM and four HOMs. The HOMER is calculated as high as 100. (b) Electric field mode profiles of the FM and three HOMs at $10.6 \mu\text{m}$.

high as ~ 100 at the scanned spectrum. The coupling of the FM to HOMs results in fluctuations, as seen in the loss performance for several HOMs [23]. The electric field profile at $10.6 \mu\text{m}$ for FM and all four HOMs are shown in Figure 3.7 (b) along with the field arrows.

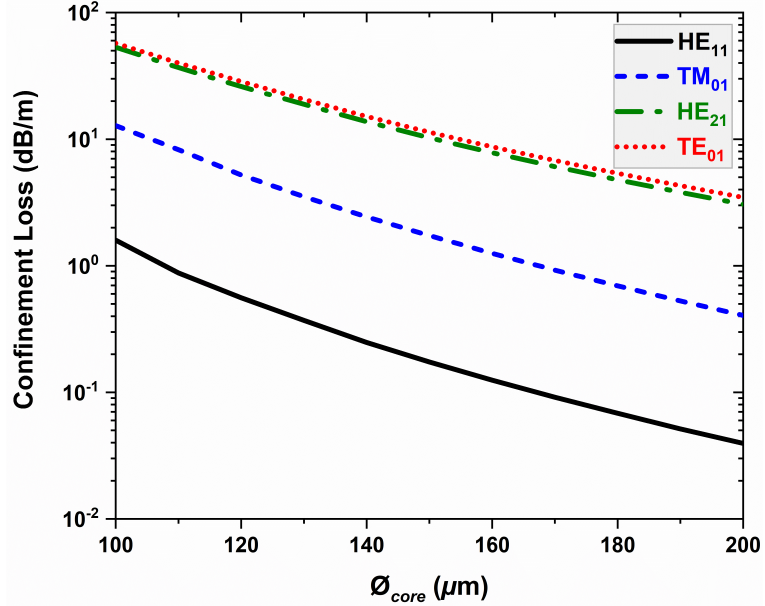


Figure 3.8: The effect of changing Ø_{core} on the confinement loss of the FM and three HOMs of STF at $10.6 \mu\text{m}$.

The effect of the Ø_{core} on the single-mode light guidance performance of STF was investigated. The primary design parameters, such as the strut thickness of the cladding tubes and the optimized ratio of the Ø_{tube} to Ø_{core} ($\text{Ø}_{tube}/\text{Ø}_{core}$) were kept the same for better comparison of the numerical results. The confinement loss of the FM and three HOMs of STF at $10.6 \mu\text{m}$ with different Ø_{core} is shown in Figure 3.8. As expected, the confinement loss of the FM and the HOMs decreases monotonically as the Ø_{core} of the fiber is increased. The change in Ø_{core} shows an insignificant effect on the single-mode light guidance characteristic of the STF design as the HOMER stays around the same, i.e., between 8-10 with changing the diameter of the fiber core.

3.3.4 Fabrication Feasibility

Various fabrication techniques, such as the well-known stack-and-draw, extrusion, and even a recently proposed 3-D printing technique, can be used to fabricate the proposed ENTF [86, 90, 49, 92]. The low drawing temperature of chalcogenide glasses can be used as an advantage for realizing such structures during the fiber drawing since preform manipulation would be more foreseeable in low-temperature processes. First, in the stack-and-draw method, although fabrication of the nested elliptical elements will be challenging, it can be achieved by initially forming the elliptical capillaries. One potential method to draw elliptical capillaries is to apply external forces at the furnace outlet while the chalcogenide glass is still in a low-viscosity state. Positioning these elliptical elements tightly in a preform tube using small supporting tubes/ellipses/rods to prevent any possible displacement of the cladding elements is necessary for a successful draw. Optimized core and cladding pressurization within an inert gas atmosphere, drawing tension of the fiber, and precise control of the drawing temperature will be crucial to achieve the desired fiber dimensions when drawing the fiber by preventing the physical/chemical deformation of the cladding elements.

The extrusion method is an alternative fabrication technique that can be used to fabricate chalcogenide glass NCFs [86]. Initially, the preform of the proposed ENTF can be extruded through a custom-made die that has a scaled cross-sectional design of ENTF. Then the extruded preform will be later used in a standard fiber draw tower to draw the desired fiber. A polymer coating may be required to preserve the mechanical strength and flexibility of chalcogenide fibers. A detailed die cleaning after the extrusion could be necessary to prevent any contamination in the system. Although extrusion is a fast way to fabricate NCFs as the initial capillary drawing and stacking are not needed in this technique, obtaining a long preform length is challenging [48, 86]. Furthermore, the 3D printers can be exploited for fabricating chalcogenide preforms by modifying the specifications of the devices [90, 91]. NCFs can be drawn using the 3D printed preform in a draw tower. However, the measured losses of the drawn fibers are

generally higher than the NCFs made with the aforementioned methods. Further improvements in all of the fabrication methods will be beneficial to fabricate better chalcogenide glass NCFs to form the ultimate IR fibers.

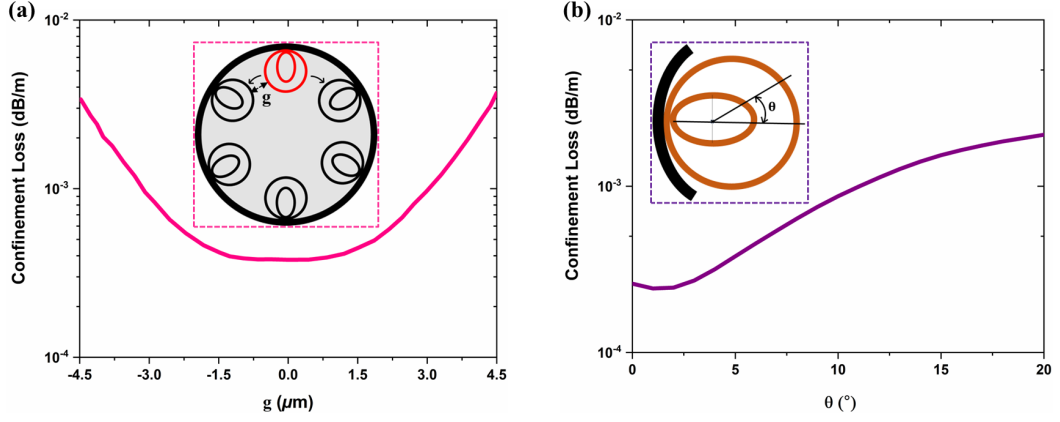


Figure 3.9: Fabrication errors for (a) the angular position of the cladding elements and (b) the rotation of nested cladding elements. A considerable increase in confinement loss was found when the symmetry of the ENTF was broken. The insets schematically show the fabrication error.

Furthermore, a study on the fabrication tolerance was performed for the cladding structures of the proposed design. Common fabrication issues such as alternating gap (g) between the elements and the rotation (θ) of the cladding elements were investigated at the wavelength of $10.6 \mu\text{m}$. The angular position of one cladding tube was shifted to break the symmetry, and the calculation was shown in Figure 3.9 (a). The losses increased one order of magnitude when the tube was shifted $\pm 4.5 \mu\text{m}$, which is a 90 % change from the initial position. The rotation of the nested cladding elements was investigated in Figure 3.9 (b). Two sets of the nested cladding elements were rotated up to 20° . The loss reaches 2.04 dB/km with a maximum rotation angle of 20° . The increase of the losses at the extreme fabrication issues is on the order of one magnitude. Therefore, the proposed design shows good fabrication tolerance at the targeted spectral region.

Chapter 4

Arsenic triselenide (As_2Se_3) NCFs

4.1 Introduction

As_2S_3 and As_2Se_3 are well-known mid-IR transparent chalcogenide glasses [34, 38, 101]. Although As_2S_3 chalcogenide NCF with 6-tube ENTF structure shows good transmission performance in the mid-IR spectrum, a detailed numerical study on the change in the transmission loss with different numbers of the cladding elements of the ENTF structure will be significant to propose a low-loss chalcogenide NCF in this region [34, 101]. As_2Se_3 chalcogenide glass has much better bulk material properties than As_2S_3 in the mid-IR region allowing low-loss guidance, especially at $10.6 \mu\text{m}$ [38]. Thus a numerical study on the cladding designs of As_2Se_3 NCFs with the same ENTF cladding elements was carried out for low-loss light transmission in the mid-IR region [38]. Primary design parameters such as the core diameter, strut thickness of cladding elements, tube diameter, and major and minor axes of the nested ellipse were systemically investigated to achieve low confinement losses in the targeted spectral window centered at $10.6 \mu\text{m}$ [38]. The change in the confinement and total loss with 5, 6, and 7 cladding tube ENTF designs were studied, and the optical performance of the proposed

fiber was compared with the previously reported NCFs in the mid-IR spectrum [38]. The single-mode light guidance performance of the proposed design was investigated, and a strong suppression on the HOMs shows that the fiber design favors the light guidance with the fundamental mode [38]. A dispersion control study was carried out to show the effect of primary design parameters on the zero-dispersion wavelength. The bending loss of our proposed design was analyzed to investigate and understand our proposed fiber structure’s sensitivity and mechanical robustness in the targeted spectrum [38]. The fabrication feasibility of the proposed design was also studied for the practical realization of the structure [38]. The proposed NCF could be potentially used in low-loss guidance for high-power lasers and could also be utilized for several other applications, such as surgery and drug delivery in the mid-IR spectrum.

4.2 Fiber Design

Figure 4.1 illustrates the schematic cross-section of the proposed 5, 6, and 7-tube ellipse-nested tubular (5-ENTF, 6-ENTF, and 7-ENTF, respectively) with annotated primary design parameters [38]. Here, \varnothing_{core} is the core diameter, \varnothing_{tube} is the diameter of the cladding tubes, t , is the strut thickness, and a and b are the major and minor axes of the nested ellipses, respectively. Although confinement loss decreases with increasing core diameter, a constant optimized \varnothing_{core} of $150 \mu\text{m}$ was chosen for all the proposed fibers to limit the total fiber diameter under $500 \mu\text{m}$ [112].

As_2Se_3 , a well-known chalcogenide glass with low material absorption in the mid-IR region, was selected as the fiber material [84, 102]. As_2Se_3 has a minor change in the refractive index real part, n_1 , in the proposed regime; therefore, a constant refractive index of 2.78 was used in our simulations for the confinement losses [102, 113]. In the case of material absorption, wavelength-dependent real and imaginary parts of refractive indices were included in the models. According to 2.1, a strut thickness (t) of $3.2 \mu\text{m}$ forms a low-loss window for the desired operation region of the proposed fiber between the first and second resonant

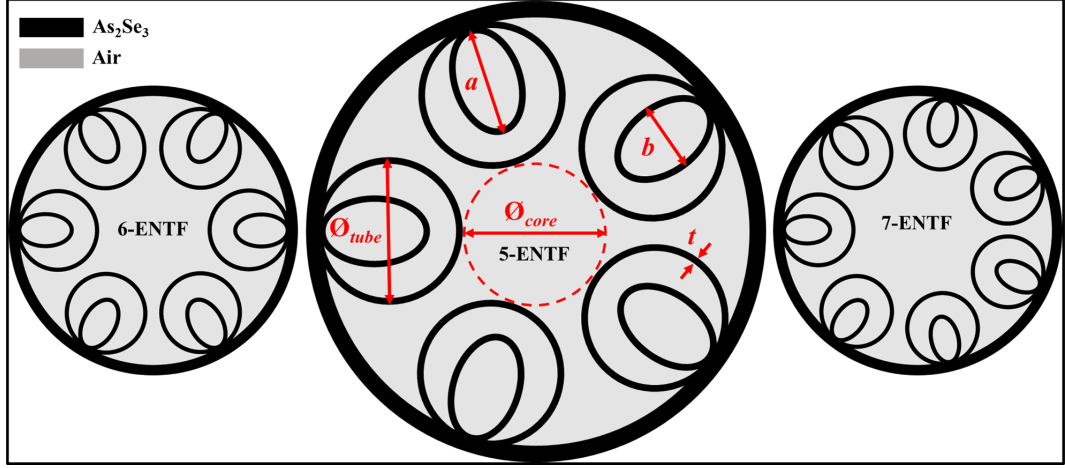


Figure 4.1: Cross-sectional schematic of the proposed As_2Se_3 chalcogenide 5-, 6- and 7-ENTF with annotated primary design parameters. A constant core diameter (Ø_{core}) of $150 \mu\text{m}$ and strut thickness (t) of $3.2 \mu\text{m}$ was used for all the elements in the fibers. Here, Ø_{tube} is the cladding tube diameter, and a and b are the nested ellipses' major and minor axes.

orders. Therefore, $3.2 \mu\text{m}$ was used as t for all the simulated fibers in this work.

4.3 Numerical Results and Discussions

4.3.1 Design Optimization

The primary design parameters of all proposed ENTf structures were systematically optimized by iteratively sweeping each design parameter at the centered wavelength of $10.6 \mu\text{m}$ [38]. The gaps between the tubular cladding elements and the parameters for the nested ellipses were determined to achieve maximum light confinement in the fiber core and, thus, minimum confinement losses. a and b of the nested ellipses of the proposed NCF were iteratively swept at different Ø_{tube} , and primary design parameters with minimum confinement losses were found. The same optimization steps were performed for all three designs (5-ENTf, 6-ENTf, and 7-ENTf). Here, it is important to mention that all the numerical studies of the ENTf were focused on the nested-ellipse designs that

have their major axis directed toward the fiber core, and the major axis of the nested ellipse is always greater than its minor axis ($a \geq b$). Additional coupling of the core-guided modes to the cladding modes increased the confinement loss of ENTF when $b > a$. Moreover, all the numerical studies were focused on ENTF with optimized tubular cladding elements, as the cladding elements with elliptical designs have been previously reported to have slightly higher transmission losses than the tubular cladding design [34].

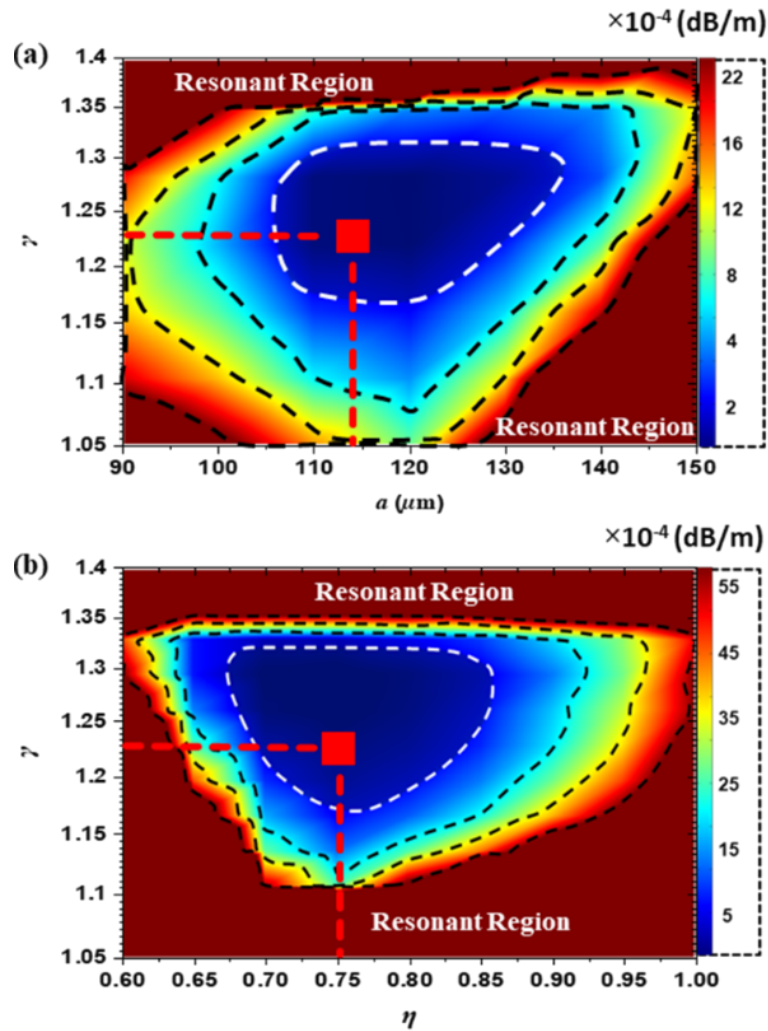


Figure 4.2: Parametric optimization of 5-ENTF. Contour plots show (a) the relationship between the γ versus a , and (b) γ versus η . The optimized ranges for the design parameters are indicated with the white dotted lines.

	γ	η	a (μm)	b (μm)
5-ENTF	1.23	0.75	114	86
6-ENTF	0.8	0.98	66	67
7-ENTF	0.66	0.96	72	69

Table 4.1: The optimized primary design parameters for 5-ENTF, 6-ENTF, and 7-ENTF at $10.6 \mu\text{m}$.

Figure 4.2 shows two contour plots for the parametric optimization of the 5-ENTF. γ denotes the size of the \varnothing_{tube} , and \varnothing_{tube} is defined as $\gamma \times \varnothing_{core}$. The confinement losses of ENTf become minimum when the γ falls between $1.18 < \gamma < 1.28$, and a is between $110 < a < 120$, as shown with the white dashed innermost curve in Figure 4.2 (a). Minimum confinement losses are achieved when the ellipticity factor (η), which is the ratio of the major axis to the minor axis of the nested ellipse ($\eta = b/a$), is between $0.70 < \eta < 0.80$, as indicated with the white innermost dashed curve in Figure 4.2 (b). The optimized design parameters (γ , a , and η) for 5-ENTF are indicated with the red dashed lines in Figure 4.2 (a) and Figure 4.2 (b). The high-loss resonant regions where the confinement loss is very high either due to the additional resonance when the cladding tubes are about to touch each other or when there is an extreme gap causing additional electric field leakage are indicated in Figure 4.2 (a) and Figure 4.2 (b). Similar optimization procedures were followed for 6- and 7-ENTFs, and the primary design parameters (γ , η , a , and b) for all three fibers are summarized in Table 4.1. Here, it is important to mention that, unlike 5-ENTF, 6-ENTF and 7-ENTF have minimum confinement losses when η were close to 1. Thus, the nested elements were almost tubular leading to designs similar to the tubular nested tubular fiber (TNTF).

4.3.2 Confinement and Total Loss

Figure 4.3 compares the confinement loss and the total loss of 5-ENTF, 6-ENTF, and 7-ENTF at the targeted mid-IR spectrum. Confinement losses of the NCF at $10.6 \mu\text{m}$ were calculated as 0.34 dB/km , 4.17 dB/km , and 60.2 dB/km , respectively. The overall guidance performance of 5-ENTF is more favorable than the 6 and 7 designs, and it shows the best light guidance with the lowest confinement loss at the centered wavelength with more than an order of magnitude improvement over the confinement losses of 6-ENTF and 7-ENTF. The improvement of the losses in 5-ENTF could be attributed to the greater separation of the guided light and outer cladding that can further prevent light leakage through the outer cladding [96].

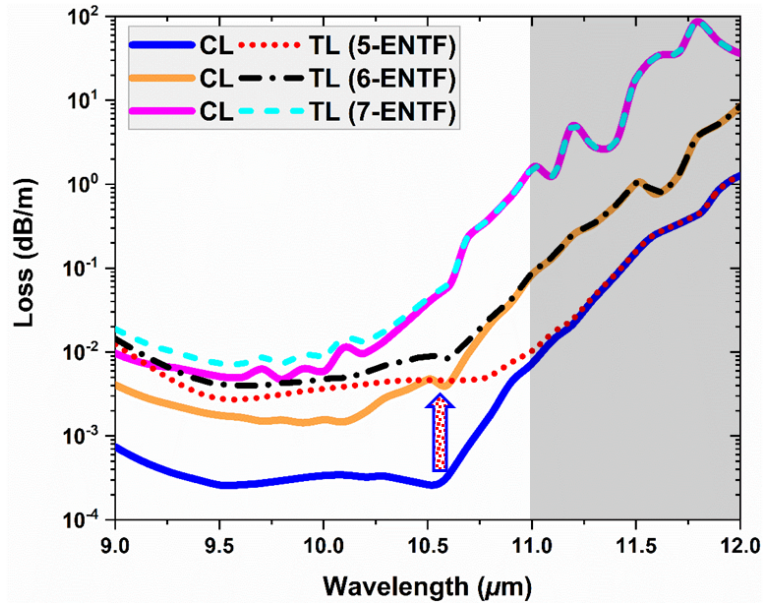


Figure 4.3: Confinement and total losses comparison for 5-ENTF, 6-ENTF, and 7-ENTF at the targeted spectrum. 5-ENTF offers the best light guidance with lower confinement and total losses than other fibers. The shaded region shows the spectrum where confinement losses are the dominant loss mechanism. The arrow shows the change in the confinement losses when the material absorption is considered for 5-ENTF.

The total losses for 5-, 6-, and 7-ENTF were calculated as 4.55 dB/km , 8.50 dB/km , and 64.8 dB/km , respectively. The total loss for 5-ENTF is around an

order of magnitude higher than its confinement loss, and this change is depicted with the arrow in Figure 4.3. The material absorption dominates the total losses up to $\sim 11 \mu\text{m}$, and confinement losses are the dominant loss mechanism for the ENTFs between $11 \mu\text{m}$ to $12 \mu\text{m}$, as shown with the shaded region. Although As_2Se_3 is transparent in the mid-IR region, the total losses of all ENTFs are still significantly lower than the bulk material loss of As_2Se_3 , which shows the advantage of using NCF to guide the electromagnetic radiation in the mid-IR spectrum [102]. Here, it is worth mentioning that any further change in the number of cladding tubes did not improve the confinement loss, and thus NCF with a 5-tube structure offers the best light guidance performance.

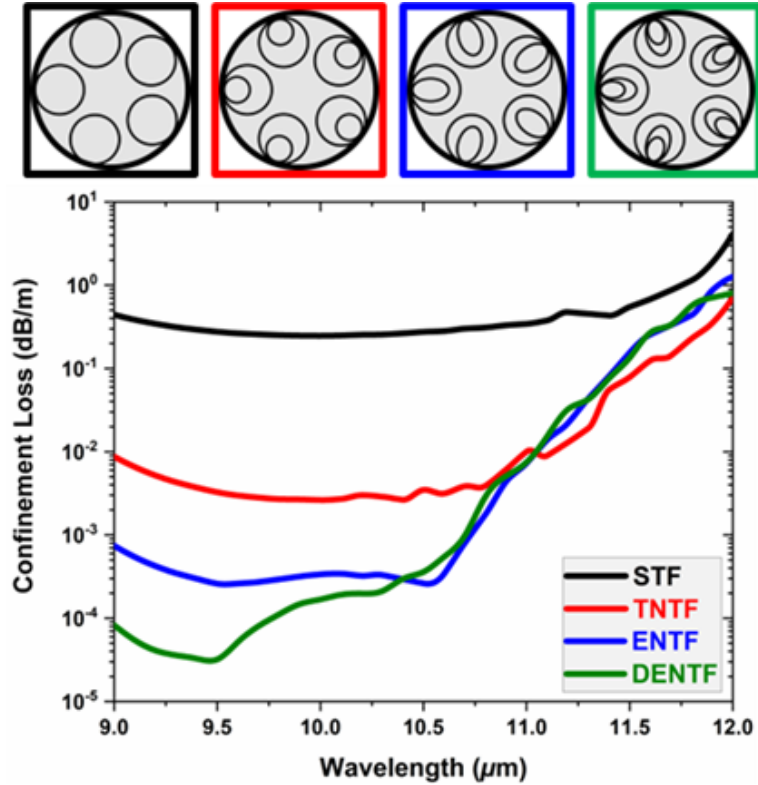


Figure 4.4: Comparison of the confinement loss of STF, TNTF, ENTf, and DENTf in the proposed mid-IR spectrum.

Figure 4.4 shows the confinement loss comparison of the proposed 5-ENTf, TNTF, double ellipse-nested tubular fiber (DENTf), and simple tubular fiber (STF) designs. To have a clear confinement loss comparison, only η of the nested

ellipse in 5-ENTF was changed to 1, i.e., $a = b$, to achieve the TNTF geometry while keeping all other design parameters the same. A nested ellipse with an optimized major axis of $65 \mu\text{m}$ and an ellipticity factor of 0.75 was inserted inside the ENTF geometry to achieve the DENTF fiber design while keeping all the other design parameters the same as for the 5-ENTF design. STF with an optimized tube diameter of $104 \mu\text{m}$ was used for better performance. Confinement losses increase by more than an order of magnitude when the fiber geometry is changed from ENTF to TNTF. Although DENTF offers comparatively lower confinement losses than ENTF at the targeted region, it has multiple sharp high-loss peaks over the spectrum and increased design complexities. Thus, it might be obtrusive to name the DENTF as the optimum design for low-loss mid-IR guidance. Furthermore, the change in the confinement loss with the addition of nested elements can be clearly seen from the loss comparison between STF and nested fibers.

4.3.3 Single Mode Performance

The single-mode light guidance characteristic of the proposed 5-ENTF was carried out in the targeted spectrum, and the loss performance of the FM and the first four HOMs is shown in Figure 4.5 (a). The electric field mode profile of all the investigated modes, namely, HE_{11} and TE_{01} , $\text{HE}_{21_{\text{even}}}$, $\text{HE}_{21_{\text{odd}}}$, and TM_{01} , respectively, are shown on top of the Figure 4.5 (a). The suppression over the HOMs is calculated, and according to the simulations, HOMER was found ~ 600 at $10.6 \mu\text{m}$ and as high as 1500 in the lower wavelengths. Multiple resonant points were found for the 6-ENTF and 7-ENTF due to the coupling between the core and cladding modes. Thus, 5-ENTF has better single-mode guidance performance than the 6- and 7-ENTFs [23]. The effect of the nested ellipse's η on the single-mode light guidance performance of the proposed 5-ENTF design was investigated. It was seen that $\eta = 0.75$ not only gives a high HOMER, but the proposed design also has good tolerance in terms of nested ellipse's η , to support single-mode light guidance characteristics while keeping the HOMER high, as shown with the dashed rectangle in Figure 4.5 (b).

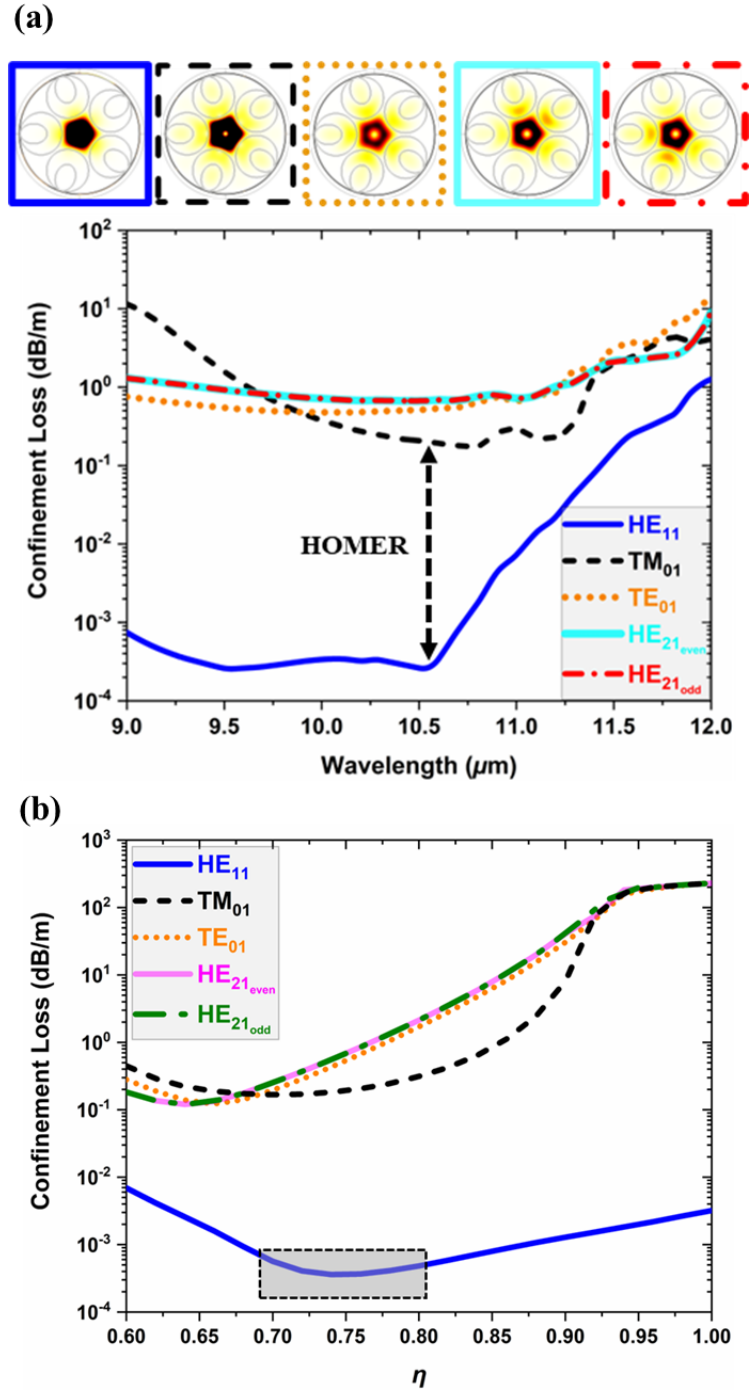


Figure 4.5: (a) The confinement losses of the FM and the first four HOMs with the electric field profiles at $10.6 \mu\text{m}$ are shown on the top. The suppression over the HOMs is found to be around 600. (b) The change in the confinement losses of the FM and HOMs of 5-ENTF with different η of the nested ellipse at $10.6 \mu\text{m}$.

4.3.4 Dispersion Control

Dispersion is an important fiber parameter for data transmission and ultra-short pulse propagation. Maintaining low dispersion around the operational wavelength(s) prevents signal and pulse mixing [39, 51, 114]. The waveguide group-velocity dispersion (GVD) defines the effect of the medium on the propagation time of a pulse, and the phenomenon can be explained with the following formulation [115, 116]:

$$\text{GVD} = -\frac{\lambda}{c} \frac{\partial^2 n_{eff}}{\partial \lambda^2} \quad (4.1)$$

where n_{eff} is the effective refractive index, λ is the wavelength and c being the light velocity in vacuum.

Although this study is focused on designing a low-loss fiber for mid-IR applications, especially for high-power laser delivery, the dispersion control was performed to show how the design parameters of the fiber structure can be altered to achieve the desired performance for potential usage in communication applications. The primary design parameters were investigated to achieve a zero-dispersion wavelength (λ_{zd}) close to the centered design wavelength of the proposed 5-ENTF. Fitted n_{eff} curves were used to calculate the GVD curves, and the results were validated by reproducing GVD curves from the literature (Appendix A) [51]. The n_{eff} of the proposed 5-ENTF structure with different t is shown in Figure 4.6 (a).

Narrow transmission windows with high confinement losses were seen in much of the proposed mid-IR spectrum for t values below $3.1 \mu\text{m}$ and above $3.5 \mu\text{m}$; therefore, t of $3.2 \mu\text{m}$ and $3.3 \mu\text{m}$ were chosen for the dispersion investigation. Figure 4.6 (b) shows the second-order dispersion curves of 5-ENTF with the proposed thickness values. Here, the shift in λ_{zd} from $9.6 \mu\text{m}$ to $10 \mu\text{m}$, close to the centered wavelength of $10.6 \mu\text{m}$, is seen when t is changed from $3.2 \mu\text{m}$ to $3.3 \mu\text{m}$. Even though the loss of $3.3 \mu\text{m}$ strut thickness design is similar to the proposed design with $3.2 \mu\text{m}$ strut thickness at $10.6 \mu\text{m}$, the overall loss profile in the targeted spectral window increases when the t is $3.3 \mu\text{m}$. Therefore, fiber with $3.2 \mu\text{m}$ strut thickness is ideal for low-loss operation, whereas $3.3 \mu\text{m}$ is better

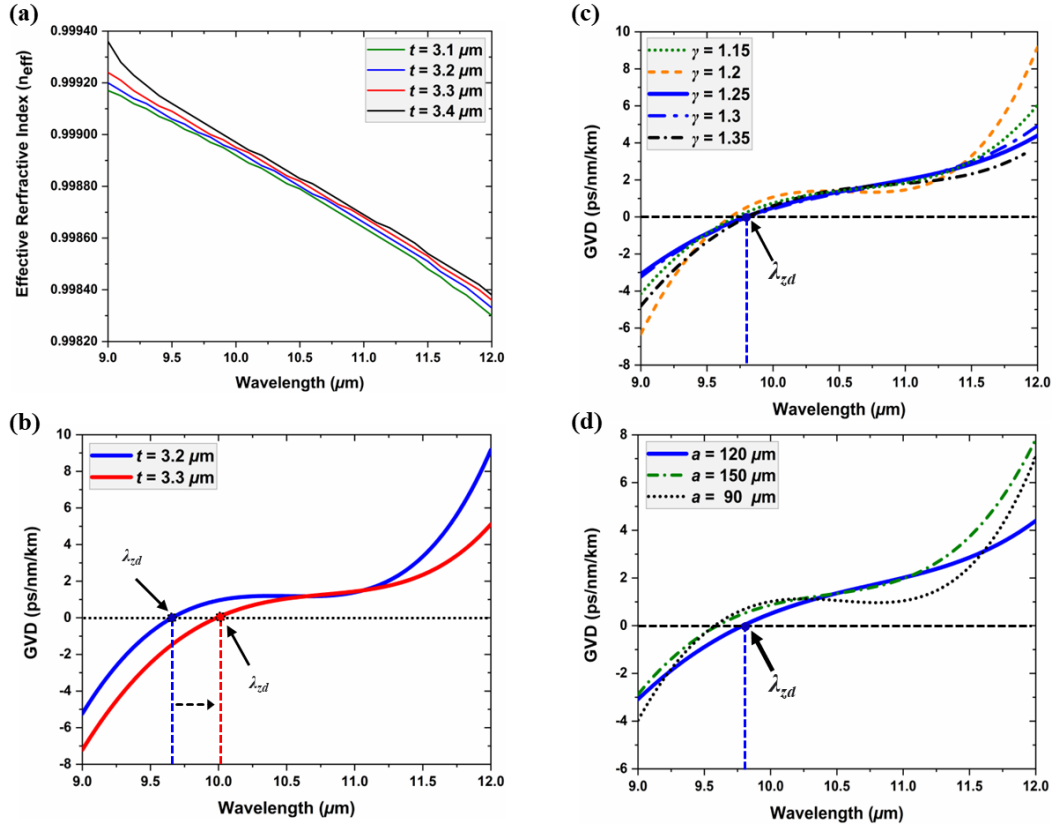


Figure 4.6: (a) n_{eff} of the proposed 5-ENTF with different values of the t . (b) GVD curves of the proposed fiber with strut thickness (t) of $3.2 \mu\text{m}$ to and $3.3 \mu\text{m}$. The zero-dispersion point is indicated with the black dotted line, whereas the change in GVD is shown with the black dashed arrow when the strut thickness is changed from $3.2 \mu\text{m}$ to $3.2 \mu\text{m}$. (c) GVD curves of 5-ENTF structure with different γ and (d) major axis of the nested ellipse (a).

for low-dispersion operation by maintaining relatively low confinement losses. Further numerical studies were carried out with different sizes of the cladding tube or nested ellipses to move λ_{zd} closer to $10.6 \mu\text{m}$. However, the results were not better than the proposed design. Thus, the proposed parameters for 5-ENTF not only offer low confinement losses but also has the desired dispersion performance.

4.3.5 Bending Loss

Generally, two types of bending can lead to a loss in optical fibers: macro-bending and micro-bending [117, 118]. Bending loss due to micro-bend can occur because of the microscopic imperfection and deformations in the fiber manufacturing or any rough contact of the fiber with any surface due to any applied tensile force [117, 118]. On the other hand, bending loss due to macro-bending occurs when there is a bent in the fiber resulting in the coupling of the core-guided modes and the cladding modes [117, 118]. The numerical studies in this thesis mainly focus on the macro-bending loss of our fiber design to investigate and understand the sensitivity and mechanical robustness of our proposed 5-ENTF structure to different bending radii under different environmental effects [30]. The straight fiber refractive index was manipulated for different bending radii in our validated numerical model to calculate the equivalent refractive index of the bent fiber using the approach in the following formulation [23]:

$$n_b = n.(1 + \frac{x}{R_b}) \quad (4.2)$$

where n_b and n are the refractive indices of the fiber with and without any bend, respectively, R_b is the bending radius, and x is the direction of bending. Figure 4.7 (a) shows the change in bending loss with different bending radii of the fiber.

The bending loss value at the critical bending radius (R_{cr}) is double the value of the loss of the straight fiber, and for our fiber design, the R_{cr} was found to be around 28 cm for our proposed design. The change in bending losses is consistent with constant lower losses after the critical bending radius. Moreover, we investigated the change in bending loss with the different radial positions of cladding elements as shown in the inset of Figure 4.7 (a). Similar results were found when the position of the cladding elements was shifted from 0° to 180° , which is the oppositely positioned cladding element. Figure 4.7 (b) compares the bending loss performance with different bending radii in the targeted spectrum. The losses of all three cases, namely straight (0 cm), 28 cm, and 50 cm, stay below 7.9 dB/km between 9.0 and 11 μm . The bending effect becomes insignificant after

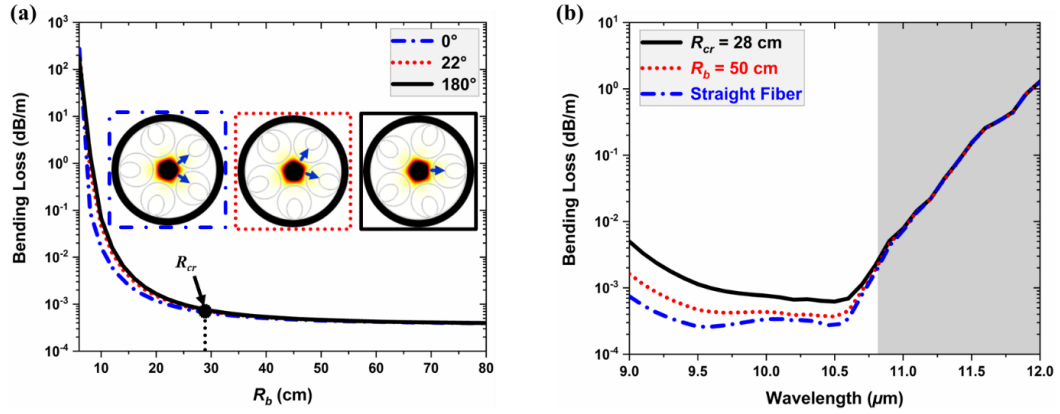


Figure 4.7: (a) The change in bending loss with different bending radii of the proposed 5-ENTF at $10.6 \mu\text{m}$. The bending loss decrease with a constant rate after the critical bending radius (R_{cr}) of 28 cm. (b) Confinement loss comparison of the straight fiber with 28 cm and 50 cm bending radii.

$10.8 \mu\text{m}$, where the resonance dominates the fiber losses, as shown with the gray region in Figure 4.7 (b).

4.3.6 Fabrication Feasibility

To further analyze the proposed fiber, a fabrication tolerance study was performed to investigate the effects of common fabrication issues to the guidance properties of the 5-ENTF. Issues such as enlarging/shrinking of cladding elements, rotation of the cladding elements, and varying strut thickness are commonly observed during the fiber drawings. In the first step, only one of the nested ellipses was changed in shape by increasing its major axis (a_0) from $60 \mu\text{m}$ to $178 \mu\text{m}$ while keeping the η to the optimized value of 0.75 for 5-ENTF. The a_0 reached a maximum value before touching the cladding tube and the effect of the shape change on the confinement losses is shown in Figure 4.8 (a).

The losses increased more than an order of magnitude when either the ellipses are too small or about to touch the cladding tube. The optimized region for a_0 , which offers low confinement losses, is indicated with the dashed rectangle in the Figure 4.8 (a), where a_0 is between $90 < a_0 < 170$. In the second step

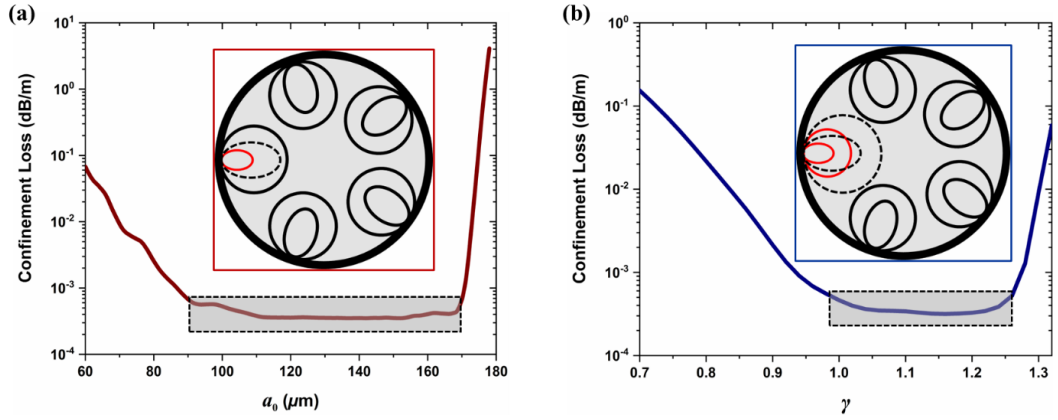


Figure 4.8: Fabrication feasibility study of the proposed 5-ENTF for (a) different sizes of one of the nested ellipses and (b) changing the size of one set of the cladding elements. Both the fabrication error studies investigated are shown schematically in the insets. The dashed rectangular regions indicate the tolerance regions for the proposed 5-ENTF design.

of the analysis, the change in the confinement loss by changing one set of the cladding and nested cladding elements was investigated, and the results are shown in Figure 4.8 (b). Here it is important to mention that the cladding tube and nested ellipse were changed by a constant ratio to have a clear confinement loss comparison. The schematic of the ellipse-nested tubular cladding element when $\gamma = 0.7$ and $\gamma = 1.32$ are shown with solid and dashed lines, respectively, in the inset of Figure 4.8 (b). The confinement loss is high when $\gamma < 0.9$ due to additional electric field leakage from the big gap between the cladding elements. The optimized design dimension for the cladding element is indicated with the dashed rectangle in Figure 4.8 (b), that is when the cladding tube is between $0.98 < \gamma < 1.26$. Further increase in the loss was observed due to the resonances when $\gamma > 1.26$ where cladding elements touch each other. The wide fabrication tolerance range provides the potential of the proposed 5-ENTF's performance against the fabrication-related disturbances in the proposed mid-IR spectrum. The growing interest in high-performance IR fibers is leading to more studies dedicated to these fibers. Presently, chalcogenide fibers have been fabricated with various methods, and their optical performance is constantly being improved to meet the demands. Commercially available chalcogenide solid-core and HCFs show the maturity of the materials and fibers. However, issues such as long-term

material stability, mechanical robustness, and cost of the fibers are still awaiting to be addressed for wider usage of chalcogenide fibers.

Chapter 5

Chalcogenide-Coated Silica NCF

5.1 Introduction

Chalcogenides are mid-IR transparent glasses with attractive optical transparency; in contrast, silica glass has a drastic increase in the transmission losses in the mid-IR region, so a hybrid chalcogenide glass-coated silica NCF is being proposed in this thesis which can guide light with less transmission losses than simple silica and simple chalcogenide NCF in the near and mid-IR region [21, 27, 43, 47, 89]. The proposed coated structure can shift the high-loss resonant peaks in both the near and mid-IR region and thus can offer a low-loss transmission window with losses much lower than the transmission losses of simple NCF structures. The preferred choice for the chalcogenide material for the proposed coated structure is As_2S_3 due to its high material transparency in the mid-IR spectrum [84, 87]. Two types of coated structures are being considered in this work, a six-tube silica NCF with As_2S_3 coating only on the outside of the cladding tubes (one-sided coating) as shown in Figure 5.1 (a), and Figure 5.1 (b) shows the As_2S_3 coating both inside and outside of the cladding tubes (double-sided coating). The core diameter, cladding tube diameter, strut thickness of the tubes, and coated thickness of the chalcogenide glass are numerically optimized, and the proposed six-tube silica NCF structure was then fabricated with the

stack-and-draw technique. Micropump was then used to coat the As_2S_3 chalcogenide solution uniformly to achieve the desired coated thickness on the cladding tubes of silica NCF. Fabrication challenges during the fiber draw are discussed in this chapter, and further modifications in the fabrication of the proposed NCF were realized for a thorough comparison with the numerical investigations.

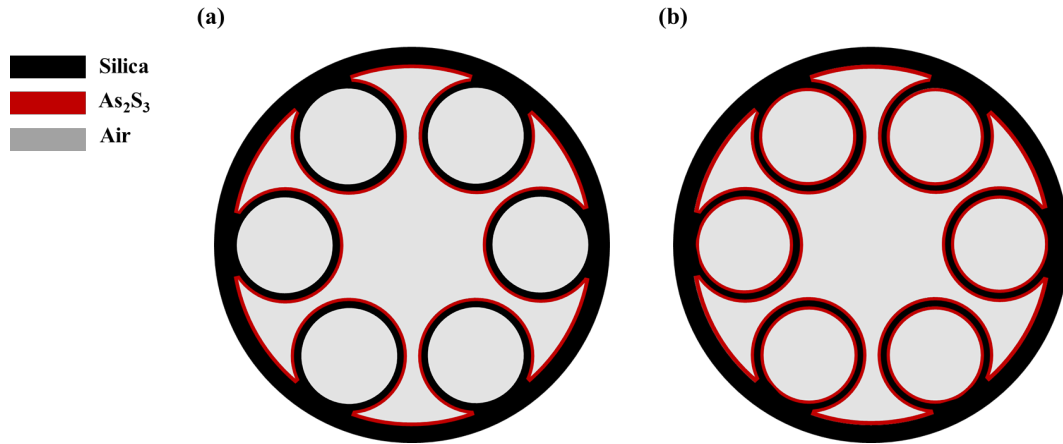


Figure 5.1: Schematics of the As_2S_3 chalcogenide glass-coated silica NCF with (a) one-sided and (b) double-sided coating of the silica cladding tubes.

5.1.1 Guidance Mechanism

The ARROW model explains the Fabry-Pérot resonator, which is formed between a chalcogenide-coated silica hollow-core capillary as illustrated in Figure 5.2. The resonator will be transparent at resonant wavelengths where constructive interference occurs, and light leaks from the air-core region [119, 120, 121]. The resonator reflects light at the antiresonant wavelengths where destructive interference occurs [119, 120, 121]. An introduction of a cladding layer that results in the phase matching of modes will lead to the coupling of core modes to the cladding modes; thus, leakage of radiations to the outer cladding [119, 121, 122]. Therefore, a strong phase mismatch and weak interaction between the fundamental core mode and the cladding modes are needed for low-loss light guidance in such NCFs [119, 121, 122].

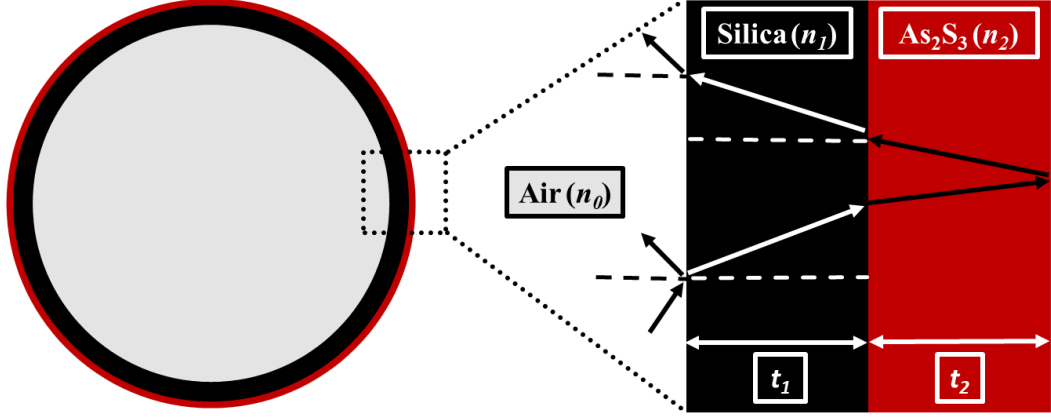


Figure 5.2: A schematic of a one-sided As_2S_3 coated silica hollow-core capillary showing the path the guided light takes at the air-silica glass interface.

The location of the resonant wavelength that is not transmitted by this type of resonator is described by the following formulation [120].

$$\lambda_{res} = \frac{2(t_1 \sqrt{n_1^2 - n_0^2} + t_2 \sqrt{n_2^2 - n_0^2})}{m} \quad m = 1, 2, 3... \quad (5.1)$$

Where λ_{res} is the resonant wavelength, t_1 is the strut thickness of the silica cladding tubes, t_2 is As_2S_3 coated thickness, n_0 , n_1 , and n_2 are the refractive indices of air, silica glass, and As_2S_3 respectively. The resonance order is represented by the integer m , which can take any integer value. According to the above formulation, the cladding material's thickness (t_1 and t_2) and material indices (n_1 and n_2) are the key determinants of the resonant wavelengths for such resonators.

5.1.2 Numerical Results and Discussions

Primary design parameters of the proposed 6-tube NCF were systematically optimized to design a As_2S_3 coated silica simple-tubular fiber (STF) design for low transmission loss in both near and mid-IR spectrum. An optimized core diameter (\varnothing_{core}) of $150 \mu\text{m}$ and a tube diameter (\varnothing_{tube}) of $95 \mu\text{m}$ are used for all the proposed STF designs. A strut thickness (t) of $4.0 \mu\text{m}$ shows minimum losses for As_2S_3 NCF in the proposed mid-IR spectrum of $9.5\text{-}13 \mu\text{m}$, and thus a constant

overall total thickness of $4.0 \mu\text{m}$ is used for all the fiber structures for a clear fiber loss comparison.

Total loss comparison of simple As_2S_3 , simple silica, and one-sided As_2S_3 coated silica STF is shown in Figure 5.3. An increase in the total loss is seen when the coating thickness of As_2S_3 on the silica cladding tube is decreased from $3.8 \mu\text{m}$ to $0.1 \mu\text{m}$, which is mainly because of the high material absorption of silica in the proposed mid-IR spectrum [21, 23, 43, 47]. A thin $0.1 \mu\text{m}$ As_2S_3 coated silica STF has almost the same high losses as the simple $4.0 \mu\text{m}$ silica STF, showing the importance of using an optimized thick chalcogenide coating to decrease the transmission losses of silica STF in the mid-IR spectrum. A $3.8 \mu\text{m}$ coating of As_2S_3 on $0.2 \mu\text{m}$ silica STF can significantly reduce the total losses from 1101 dB/m in the case of $4 \mu\text{m}$ silica NCF to 13.6 dB/m at $11.5 \mu\text{m}$ as can be seen in Figure 5.3.

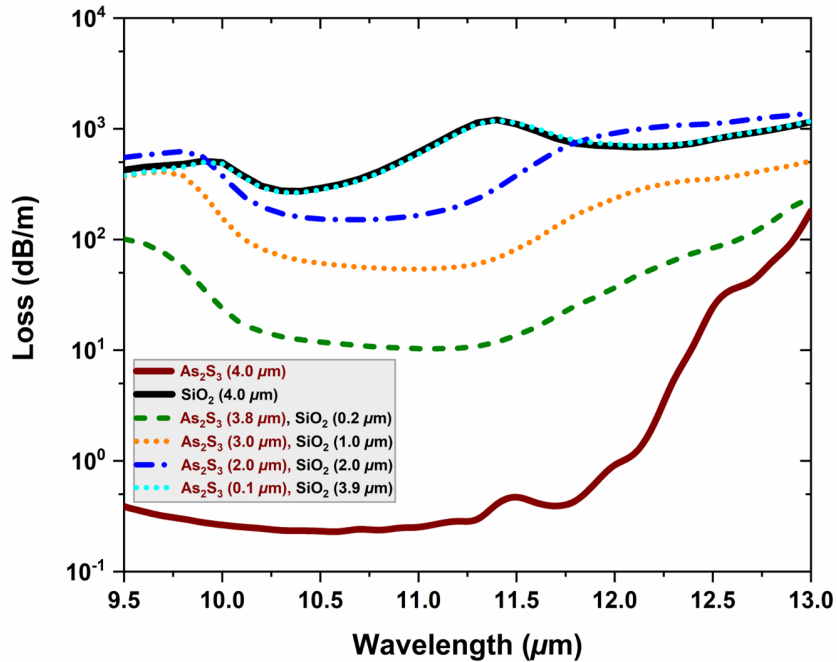


Figure 5.3: A comparison of the total loss of simple As_2S_3 , simple silica, and one-sided As_2S_3 coated silica STF in the proposed mid-IR region.

A comparison of the total loss of the tube-nested tubular fiber (TNTF) design with simple As_2S_3 , simple silica, and one-sided As_2S_3 coated silica was carried

out to study the effect of chalcogenide coating on transmission loss in nested cladding NCF structures. Here it is important to mention that both the cladding tubes and the nested cladding tubes in the TNTF designs were coated for this analysis. The \varnothing_{core} was kept the same and an optimized \varnothing_{tube} of $135\ \mu\text{m}$ and \varnothing_{nest} of $60\ \mu\text{m}$ were used. A $3.8\ \mu\text{m}$ coating of As_2S_3 on $0.2\ \mu\text{m}$ silica TNTF design significantly reduced the total losses from $1135\ \text{dB/m}$ to $12.6\ \text{dB/m}$ at $11.5\ \mu\text{m}$ as can be inferred from Figure 5.4. There is no significant change in the reduction in total loss with TNTF structure compared to the STF-coated design because the material absorption of silica glass dominates the total loss performance; therefore, a thick coating of As_2S_3 is needed to reduce the transmission loss significantly.

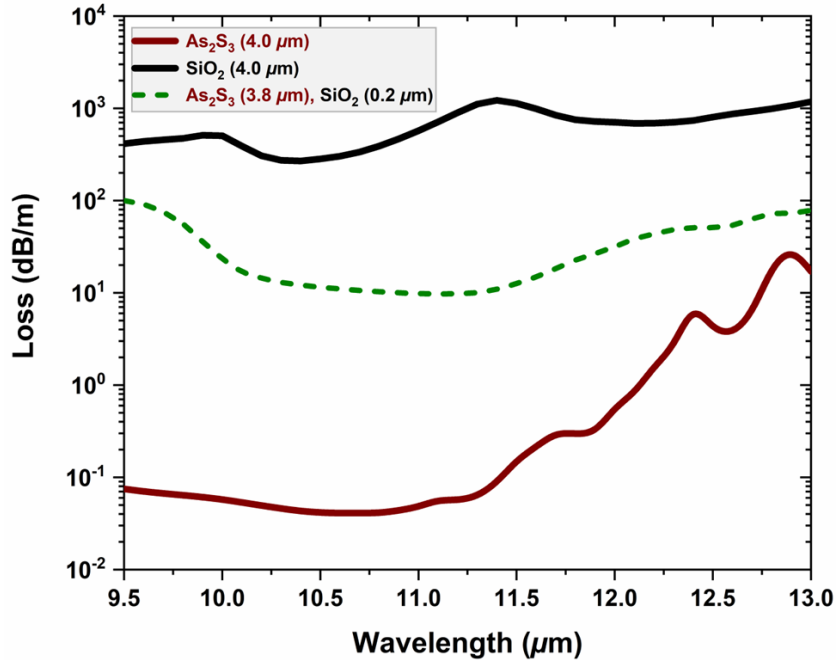


Figure 5.4: A comparison of the total loss for TNTF design with simple As_2S_3 , simple silica, and one-sided As_2S_3 coated silica fiber in the proposed mid-IR region.

The total loss comparison of one-sided and double-sided As_2S_3 coated silica STF structures is shown in Figure 5.5. Although the total fiber loss increases in both cases as the thickness of the chalcogenide coating on silica STF is decreased, the overall total loss of double-sided coated structures is much higher than the one-sided coated structures in the proposed spectrum. Thus, the double-sided

coated structures are not favorable for low-loss operation in the proposed mid-IR region, and only one-sided chalcogenide coated structures are considered for the remaining numerical analysis in this chapter.

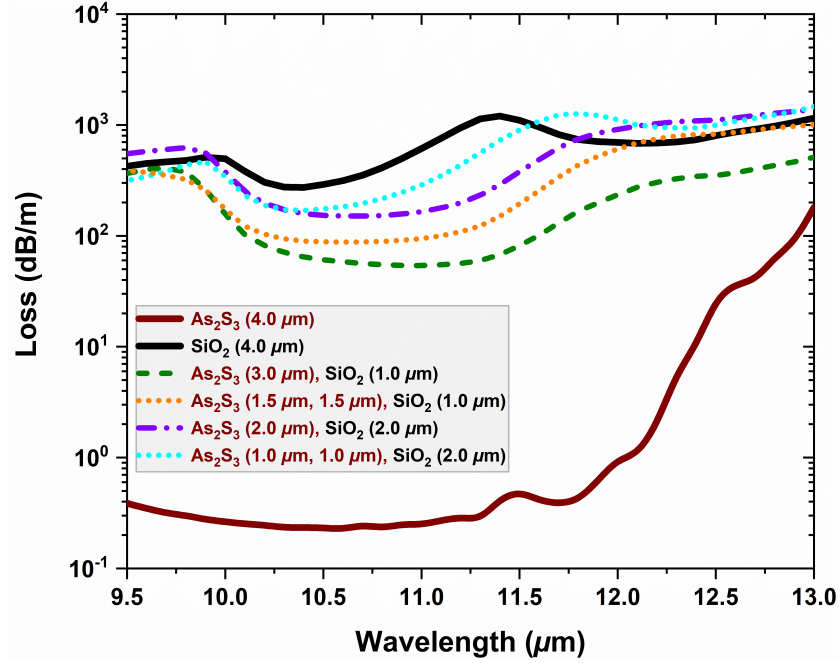


Figure 5.5: Total loss comparison of simple As_2S_3 , simple silica, and one and double-sided As_2S_3 coated silica STF in the proposed mid-IR region. The overall total loss of double-sided coated structures is higher than the one-sided structures in the proposed region.

Figure 5.6 shows the total loss performance of simple As_2S_3 , simple silica glass, and As_2S_3 coated silica STF in the near-IR and mid-IR region. The minimum loss curves for simple As_2S_3 and simple silica STF were calculated by simulating the STF structure with different strut thicknesses of the cladding elements and then plotting the minimum loss values for each respective thickness in the proposed spectrum. A thin coating of As_2S_3 does not reduce the transmission loss as shown in the case of $0.5 \mu\text{m}$ As_2S_3 coating on $1.0 \mu\text{m}$ silica STF in Figure 5.6, where the loss profile for the coated structure touches the minimum loss curve of simple silica STF. A thick coating is needed to reduce the loss of the silica-coated STF due to the high material absorption of silica in the mid-IR region. The loss decreases from 2.39 dB/m at $0.42 \mu\text{m}$ at $5.5 \mu\text{m}$ in the case of silica STF with a

cladding tube strut thickness of $0.2 \mu\text{m}$ and a thick As_2S_3 coating of $1.8 \mu\text{m}$.

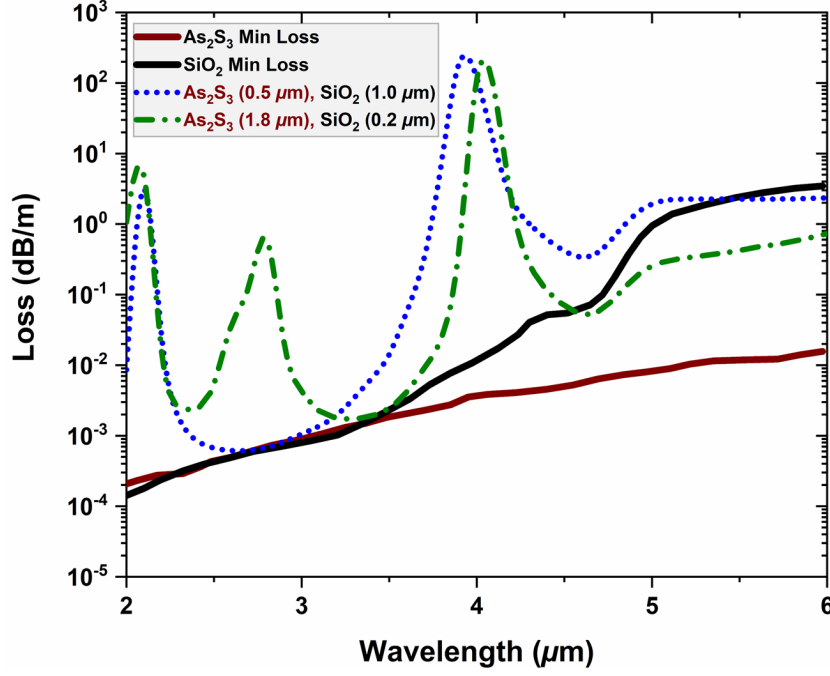


Figure 5.6: Total loss comparison of simple silica, simple As_2S_3 and As_2S_3 coated silica STF with different coated thicknesses.

These results show that careful optimization of design parameters of a chalcogenide-coated silica NCF can not only offer a low-loss transmission in regions where silica glass has very high material losses, such as in the mid-IR region between $9.5 \mu\text{m}$ to $13 \mu\text{m}$, but can also shift the high-loss resonant peaks in both the near and mid-IR region, and thus can offers a low-loss transmission window with losses much lower than the transmission losses of simple silica and simple As_2S_3 NCF. The high material absorption of silica glass in the mid-IR region requires a thick coating of the chalcogenide glass to reduce the transmission loss significantly.

5.2 Fiber Fabrication

Fabrication techniques such as the stack-and-draw method, extrusion, and the recently proposed 3D printing technique can be used to fabricate NCFs [48, 90, 123, 124, 125]. The stack-and-draw fabrication technique was used in this work to fabricate our six-tube silica NCF, which is the most commonly employed fabrication method for fabricating such fibers. This technique's fabrication procedure can be divided into different steps, as shown in Figure 5.7. This section divides the detailed explanation of fiber fabrication into subsections; preform preparation, cane drawing, and final fiber drawing.

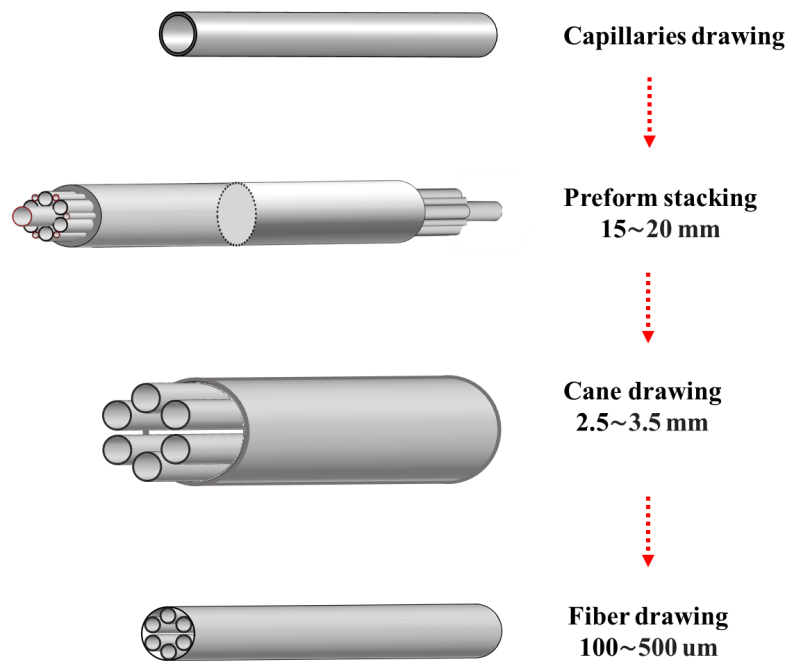


Figure 5.7: A schematic showing different steps employed in the stack-and-draw fabrication technique for NCF.

5.2.1 Preform Preparation

Before starting the cane and fiber drawing procedures in the fiber tower, a preform design based on the structure of our desired fiber is stacked using the cladding capillaries, supporting capillaries, and an outer jacket tube to stack all the capillaries inside together. Detailed numerical studies are carried out before designing the final preform to optimize the primary design parameters of our proposed fiber such as the core radius, strut thickness, and diameter of the microstructured cladding tubes in order to achieve low transmission loss in a broad bandwidth with a very good single mode light guidance characteristic. The size of the cladding capillaries drawn from the silica tubes is calculated based on the final fiber structure and the size of the outer jacket tube where these capillaries will be manually stacked. A considerable error in the size of calculated and actual capillaries may lead to a preform that is either not stacked firmly or, if the capillaries have a larger diameter than the calculated ones, it may result in either damaging or breaking of the capillaries during stacking.

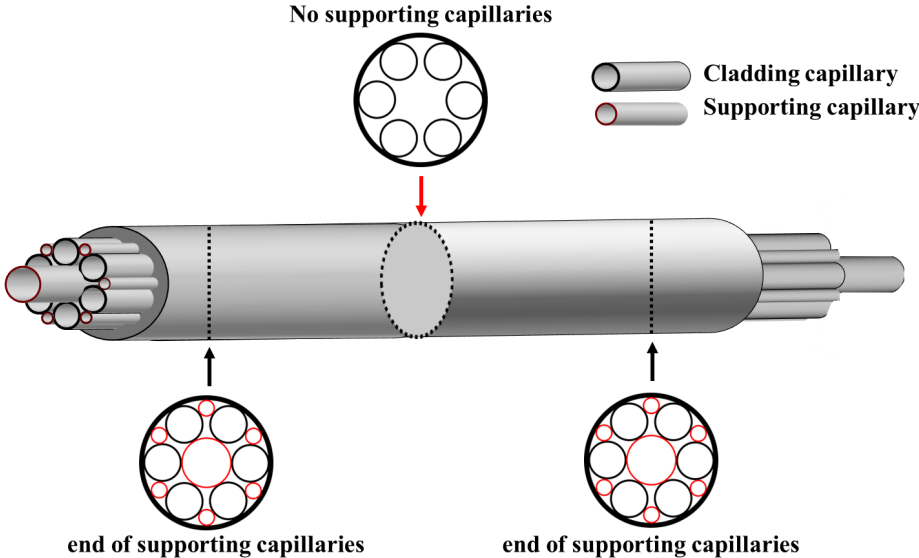


Figure 5.8: A schematic of a 6-tube stacked preform. Supporting capillaries are only used at both ends of the preform, as indicated in the schematic, and are not present in much of the preform length.

A schematic of a sample stacked preform is shown in Figure 5.8. Supporting capillaries are stacked between the gaps in the cladding capillaries to support the structure and keep it intact to avoid any structure collapse during the draw. The cladding capillaries will serve as the cladding tubes when the preform is scaled down in the fiber drawing tower. The gap between the cladding capillaries should always be kept constant since uniform gaps between the cladding tubes or touching cladding tubes will lead to additional transmission loss [23, 25]. The supporting capillaries are only used at both ends of the fiber, and they are not present in much of the preform length, which will eventually be used to draw the cane and then the final fiber as shown in Figure 5.8 [125]. Figure 5.9 shows the cross-section of a stacked preform with six cladding capillaries and supporting capillaries. In our work, due to the difficulty in fusing the stacked preform properly, the center support is inserted throughout the preform length to avoid any collapse of the preform structure during the cane and fiber drawing.

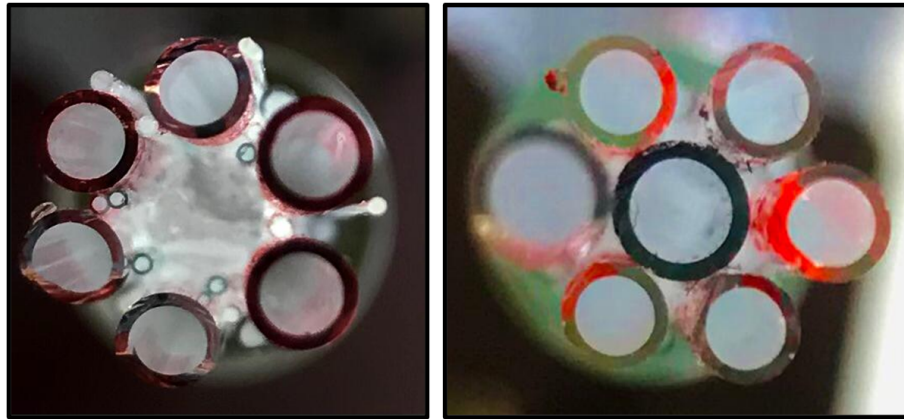


Figure 5.9: Cross-section images of 6-tube silica glass stacked preform showing the cladding capillaries and the support capillaries used to stack the preform structure firmly.

5.2.2 Cane Drawing

Once the preform is stacked firmly, the next step is to fuse the stacked preform with a precise feed rate and temperature in the fiber tower to avoid any deformation or necking of the preform during fusing. Fusing the cladding tubes to the

outer jacket is necessary to avoid any collapse of the fiber structure during the draw. Cane is then drawn from the fused preform in the fiber tower. Figure 5.10 shows a detailed schematical view of the fiber drawing tower. The main components of the tower include the preform feed unit, furnace to heat the preform, diameter gauge, fiber coating cup, UV lamps, pressure chamber, tension wheels, capstan drive to pull the fiber, and spooling wheel to collect the final fiber drawn. Cane is a macroscopic form of the final fiber, and it can vary in diameter, typically ranging from 2.5-5 mm.

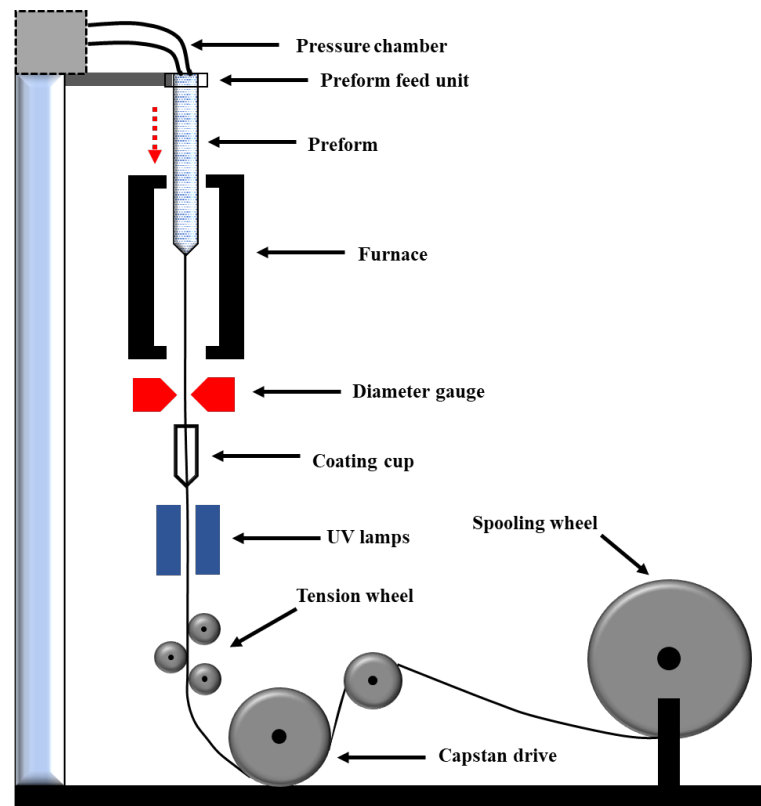


Figure 5.10: A schematic showing different parts and components of a fiber drawing tower.

During our fiber fabrication, due to the difficulty in properly fusing the cladding tubes in the stacked preform to the outer silica jacket, the cane drawing from the preform mostly resulted in the fusing of cladding capillaries with each other, resulting in an undesired collapsed cladding structure as can be seen in Figure 5.11. Such fabrication issues also lead to minor changes or deformation of

the cladding tube geometrical shape during the cane draw. To avoid such collapse of the cladding structure and achieve a desired uniform separation between the tubes, the center support was then inserted throughout the fiber length, as seen in the microscopic images of the drawn cane in Figure 5.11.

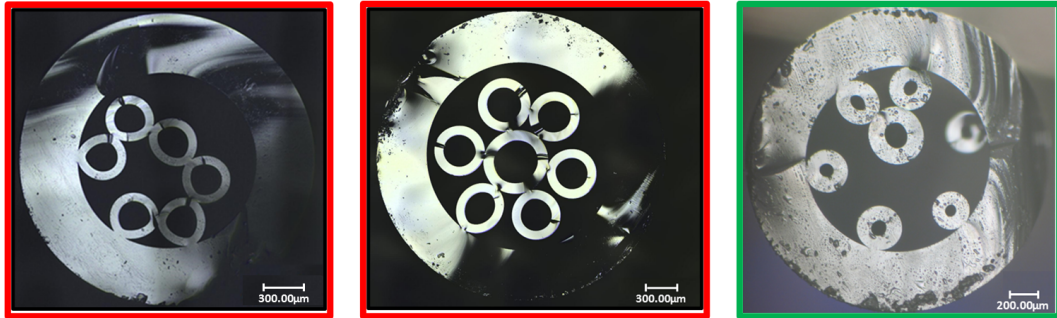


Figure 5.11: Microscopic images of the unsuccessful (red outline) and successful (green outline) canes drawn from the stacked preform. The center support tube was inserted all along the fiber length to avoid the collapse of the cladding structure.

A successful cane or fiber with desired dimensions can only be fabricated if the fluid dynamics of the furnace in the fiber tower are fully understood and controlled. The three main drawing parameters influencing the structure of the cane and fiber are the drawing temperature, feed speed of the preform, and the capstan drawing speed applied. A careful understanding and control of all these three crucial drawing parameters are essential to successfully fabricate a cane or fiber with desired cladding structure, and dimensions [123]. The main drawing parameters are optimized and chosen considering different fluid dynamics phenomena inside the tower furnace and the geometrical parameters of the preform used, such as the viscosity of the preform material and the surface tension, and the size of the preform and the cane used to draw the final fiber, etc. [123]. A low drawing temperature increases the viscosity of the preform and thus increases the tension in the fiber, which may lead to fiber breaking; so, although a low drawing temperature can reduce the surface tension, care must be taken to choose the drawing temperature so as not to break the final fiber [123]. The furnace time of the preform and the surface tension is reduced when high feed speed is used; hence, all these crucial drawing parameters should be controlled to draw cane and

fiber with the desired shape, and dimensions [123]. During our fiber draw, efforts were made to carefully control all these crucial drawing parameters to achieve the desired fiber structure.

5.2.3 Fiber Drawing

Once the cane is drawn, it is placed inside an outer silica jacket tube to provide the mechanical strength needed when the final fiber is drawn from the cane. Pressure is applied to the cladding tubes and core while drawing the fiber to expand the cladding elements and to avoid any collapse of the cladding structure. Precise control of the pressure applied is essential since a very high or low pressure may result in an undesired shape and size of the final cladding tube structure.

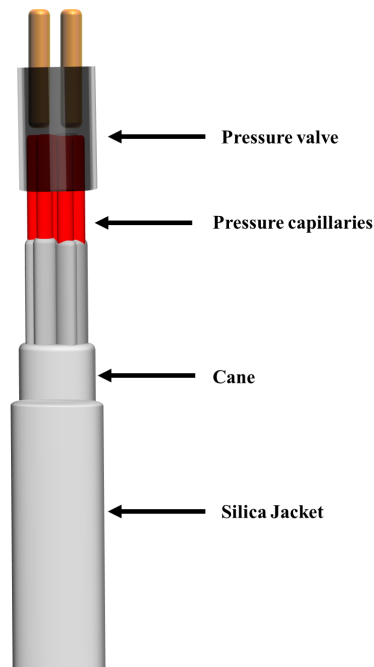


Figure 5.12: A schematic cross-section illustrating the pressure applied to the cladding capillaries and core of the cane to draw the final fiber in the draw tower.

During our fiber draw, external capillaries were first inserted into the cladding tubes and the cane structure's core. Then, epoxy was used to glue and fill the remaining hollow parts of the cladding to avoid any leakage of the gas pressure

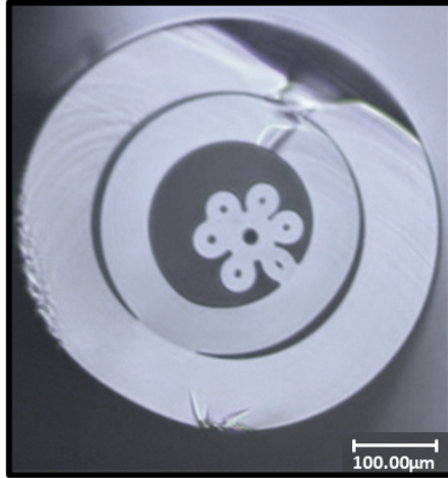


Figure 5.13: A microscopic image of the final fiber drawn from the cane. The cane was first inserted in an outer jacket to provide mechanical strength during the fiber draw.

applied. The cane was then installed in the preform feed unit of the tower with a pressure chamber connected to the pressure valve, as can be inferred from the schematic in Figure 5.12. During our fiber draw, the main drawing parameters, such as the drawing temperature, feed speed of the preform, draw speed, and the pressure applied to the cladding tubes and core, were adjusted and controlled to achieve the desired shape and size of our final fiber. The diameter of our drawn fiber is between $100\ \mu\text{m}$ to $500\ \mu\text{m}$ with a very large scale-down ratio from the initial preform of around 30 to 200. A microscopic image of the final fiber drawn is shown in Figure 5.13.

5.3 Chalcogenide Coating

A chalcogenide solution of As_2S_3 was uniformly coated on the inside of the cladding tubes using a micropump as shown in Figure 5.14 (a). The presence of coating was further validated with the elemental composition analysis technique, Energy Dispersive X-Ray Analysis (EDX), where elemental composition peaks of As_2S_3 were detected on the EDX spectra as shown in Figure 5.14 (b).

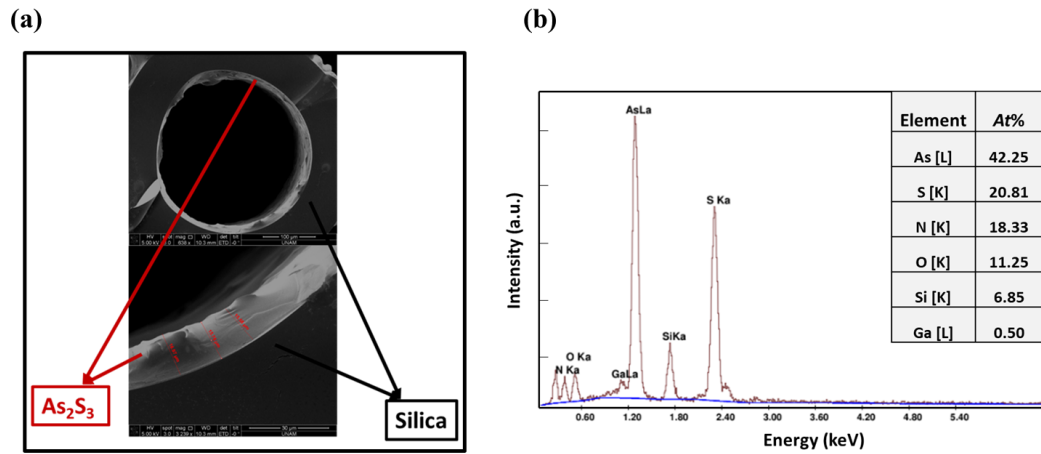


Figure 5.14: (a) A microscopic image showing the coating of As_2S_3 solution on the inside of the silica cladding tubes. (b) EDX analysis of the coated solution showing the elemental composition and atomic % of As and S.

5.4 Fabrication Challenges and Solutions

The cladding tubes could not properly fuse to the outer jacket tube during the preform fusing stage, resulting in a uniform gap between the cladding capillaries and, in some cases, capillaries touching each other, thus resulting in a collapsed cladding structure as can be seen in Figure 5.15. Some of the challenges faced during fiber fabrication and possible ways to solve them are explained below:

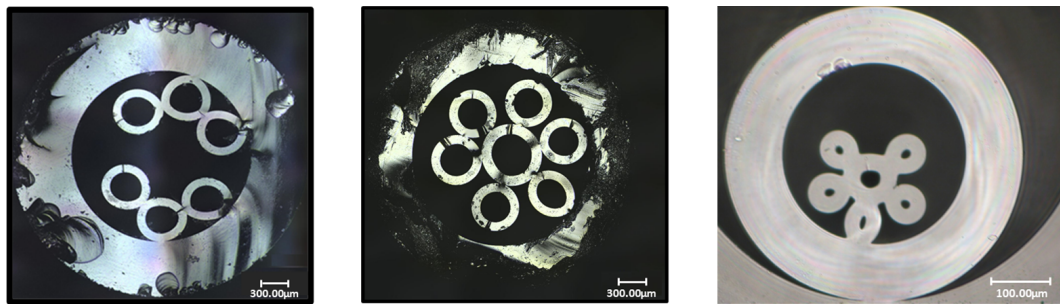


Figure 5.15: Microscopic images showing different fabrication challenges which can potentially occur during the cane and fiber draw of a silica NCF.

- During the preform stacking, the supporting capillaries between the cladding tubes and in the center should only be used at the very beginning and end part of the preform and must not be used in much of the

remaining length of the preform, which will be used to draw the cane and the final fiber. Due to the difficulty in properly fusing the stacked preform in the fusing and cane draw stage, the center support capillary in our preform was used throughout the fiber length since the absence of the center support capillary led to a significant shift of the stacked capillaries from its initial original stacked position during the cane and fiber draw. It resulted in an ununiform gap between the cladding tubes or, in some cases, the touching of adjacent tubes with each other and, thus, a collapsed cane and fiber structure as shown in Figure 5.15. To achieve a nodeless NCF without any center support capillary and significant deformation of the cladding structure, the initially stacked preform must be fused properly during the fusing stage, with each cladding tube touching the outer jacket.

- An unprecise control of differential pressure inside the cladding capillaries and the fiber core may result in an undesired fiber cladding structure. In case of excessive pressure, the cladding capillaries may expand massively, resulting in either touching the adjacent tubes or microstructure cladding elements with very thinner membranes. Using excessive pressure will also shrink the fiber core and thus will result in a cladding structure with dimensions significantly varying from the optimized parameters, which are necessary to achieve low-loss transmission. A similar phenomenon can occur in the case of using very low pressure. Thus, it is vital to supply a precise adequate pressure to the cladding capillaries and core to achieve the desired dimensions of the fiber core, cladding tubes, and membrane thickness, which are critical for achieving confined light guidance due to antiresonant reflection with low-loss transmission.
- To successfully fabricate the desired fiber structure, primary drawing parameters should be precisely optimized, adjusted, and controlled. Primary fiber design parameters, such as the strut thickness of the microstructured cladding tubes, are essential for achieving the antiresonant reflection needed for low-loss transmission in the desired spectrum. Thus uniformity of the fiber structure is essential and must be maintained throughout the fiber

length. Nevertheless, numerical fabrication tolerance studies should be carried out to allow for a wide margin of fabrication tolerance considering the different fabrication issues and errors discussed above, which can be realized during the fiber drawing.

Chapter 6

Conclusion

The low-loss light guidance and wide bandwidth of NCFs have recently gathered great interest and have found applications in different areas such as communication, sensing, high-power beam delivery, and nonlinear optics. Although silica is a material of choice for low-loss light guidance in the visible and near-IR region, the rapid increase of infrared absorption in silica NCFs limits its usage in the mid-IR spectrum. Light guidance in the mid-IR spectrum has many vital applications, and thus, alternative mid-IR transparent materials such as chalcogenide glasses are preferred for low-loss light guidance in this region. Various NCF designs with different cladding structures have been proposed using IR transparent materials to guide light with transmission loss in the mid-IR region.

As₂S₃ chalcogenide glass NCFs with tubular/elliptical cladding structures were studied for low-loss light guidance in the mid-IR region. The primary design parameters of all the six-tube fiber designs were systemically optimized to achieve low-loss light guidance in the mid-IR region with a centered wavelength of 10.6 μm . The confinement loss of ellipse-nested tubular negative curvature fiber (ENTF) was significantly lesser than the other proposed tubular or elliptical NCFs, and it was calculated as 0.287dB/km at 10.6 μm . The single-mode guidance of the proposed design was investigated, and it was found that the structure favors the guidance with the fundamental mode. The low-loss performance of the proposed fiber design

shows the strong potential of its usage for low-loss CO₂ laser transmission. As₂Se₃ chalcogenide glass has better bulk material properties than As₂S₃ in the mid-IR region. A systematic numerical study on the impact of the number of cladding tubes on the confinement losses of As₂Se₃ chalcogenide glass NCF with ENTF design was presented for low-loss mid-IR transmission. The primary design parameters of the proposed fiber design were systematically optimized, and the confinement and total loss of the proposed 5-ENTF were calculated as 0.34 dB/km and 4.55 dB/km, respectively, which are significantly lesser than the 6- and 7-ENTF at the centered wavelength of 10.6 μm. The single-mode light guidance performance of the proposed design was studied, and a strong suppression over the HOMs shows that the proposed design favors light guidance with the fundamental mode. A bending loss study was carried out to study the effect of different bending radii on the total loss of the proposed fiber. A dispersion control study was performed to shift the zero-dispersion wavelength close to 10.6 μm by optimizing the primary design parameters. The proposed ENTF can potentially offer low-loss guidance performance in the mid-IR spectrum with single-mode light guidance characteristics and low dispersion properties for applications with infrared lasers such as CO₂ lasers.

Silica glass has high attenuation in the mid-IR region; therefore, an As₂S₃ coated silica simple-tubular NCF was proposed for low-loss light transmission in the near and mid-IR region. A careful numerical investigation of the fiber design parameters, such as the thickness of the coated chalcogenide solution on the silica cladding tubes, decreased the transmission losses from 2.39 dB/m to 0.42 dB/m at 5.5 μm and from 1101 dB/m to 13.6 dB/m at 11.5 μm.

The six-tube silica NCF was fabricated using the stack-and-draw fabrication technique. The silica capillaries with desired dimensions were first drawn and then stacked and fused to be drawn to a cane in the fiber tower. The final fiber was then drawn from the cane and coated with As₂S₃ chalcogenide solution. The coating of the chalcogenide solution was validated with the EDX analysis. Further modifications in the fabrication of the NCF were

realized to successfully fabricate the final fiber structure and compare the experimental performance with the numerical investigations.

Future work will focus on first successfully fabricating the proposed NCF structure and then coating it with the chalcogenide solution to achieve the desired transmission performance. The successful fabrication of such NCF in our laboratory with desired dimensions will pave the way for the fabrication of many other complex structures in the coming days. The proposed low-loss chalcogenide NCF structure will be numerically studied and designed with other mid-IR transparent materials, such as telluride and fluorides, to further reduce the transmission loss and to compare their performance with the simple silica and chalcogenide NCF in the proposed spectrum. Novel NCFs for near-IR, mid-IR, and THz regions will be designed to address various applications in areas such as gas-sensing and spectrometry, low-loss guidance of different IR lasers, communications, medical diagnosis, and micromachining. To investigate such fibers more comprehensively, the numerical analysis of these fibers will be broadened to include various other studies, such as polarization-maintaining NCFs and different nonlinear optical effects and phenomenons.

In conclusion, the attractive material transparency of chalcogenide glasses makes them an ideal candidate for low-loss light guidance in NCFs in the IR region, which has applications in sensing, biomedical surgery, and low-loss laser delivery.

Bibliography

- [1] K. C. Kao and G. A. Hockham, “Dielectric-fibre surface waveguides for optical frequencies,” in *Proceedings of the Institution of Electrical Engineers*, vol. 113, pp. 1151–1158, IET.
- [2] P. Russell, “Photonic crystal fibres,” in *Optical Fiber Communication Conference*, p. OTuC1, Optical Society of America.
- [3] G.-D. Peng, *Handbook of Optical Fibers*. Springer, 2019.
- [4] F. Benabid, J. C. Knight, G. Antonopoulos, and P. S. J. Russell, “Stimulated raman scattering in hydrogen-filled hollow-core photonic crystal fiber,” *Science*, vol. 298, no. 5592, pp. 399–402, 2002.
- [5] S. Brustlein, P. Berto, R. Hostein, P. Ferrand, C. Billaudeau, D. Marguet, A. Muir, J. Knight, and H. Rigneault, “Double-clad hollow core photonic crystal fiber for coherent raman endoscope,” *Optics express*, vol. 19, no. 13, pp. 12562–12568, 2011.
- [6] F. Poletti, M. N. Petrovich, and D. J. Richardson, “Hollow-core photonic bandgap fibers: technology and applications,” *Nanophotonics*, vol. 2, no. 5-6, pp. 315–340, 2013.
- [7] P. Roberts, F. Couny, H. Sabert, B. Mangan, D. Williams, L. Farr, M. Mason, A. Tomlinson, T. Birks, and J. Knight, “Ultimate low loss of hollow-core photonic crystal fibres,” *Optics express*, vol. 13, no. 1, pp. 236–244, 2005.

- [8] J. C. Knight, J. Broeng, T. A. Birks, and P. S. J. Russell, “Photonic band gap guidance in optical fibers,” *Science*, vol. 282, no. 5393, pp. 1476–1478, 1998.
- [9] N. Litchinitser, A. Abeeluck, C. Headley, and B. Eggleton, “Antiresonant reflecting photonic crystal optical waveguides,” *Optics letters*, vol. 27, no. 18, pp. 1592–1594, 2002.
- [10] R. Cregan, B. Mangan, J. Knight, T. Birks, P. S. J. Russell, P. Roberts, and D. Allan, “Single-mode photonic band gap guidance of light in air,” *science*, vol. 285, no. 5433, pp. 1537–1539, 1999.
- [11] B. Mangan, L. Farr, A. Langford, P. J. Roberts, D. P. Williams, F. Couny, M. Lawman, M. Mason, S. Coupland, and R. Flea, “Low loss (1.7 db/km) hollow core photonic bandgap fiber,” in *Optical Fiber Communication Conference*, p. PD24, Optical Society of America.
- [12] W. YUXI, *Light guiding properties of negative-curvature hollow-core fiber*. Thesis, 2021.
- [13] F. e. Poletti, N. Wheeler, M. Petrovich, N. Baddela, E. Numkam Fokoua, J. Hayes, D. Gray, Z. Li, R. Slavík, and D. Richardson, “Towards high-capacity fibre-optic communications at the speed of light in vacuum,” *Nature Photonics*, vol. 7, no. 4, pp. 279–284, 2013.
- [14] A. W. Snyder and J. Love, *Optical waveguide theory*. Springer Science & Business Media, 2012.
- [15] G. Renversez, P. Boyer, and A. Sagrini, “Antiresonant reflecting optical waveguide microstructured fibers revisited: a new analysis based on leaky mode coupling,” *Optics Express*, vol. 14, no. 12, pp. 5682–5687, 2006.
- [16] F. Couny, F. Benabid, and P. Light, “Large-pitch kagome-structured hollow-core photonic crystal fiber,” *Optics letters*, vol. 31, no. 24, pp. 3574–3576, 2006.

- [17] F. Couny, F. Benabid, P. Roberts, P. Light, and M. Raymer, “Generation and photonic guidance of multi-octave optical-frequency combs,” *Science*, vol. 318, no. 5853, pp. 1118–1121, 2007.
- [18] G. Pearce, G. Wiederhecker, C. G. Poulton, S. Burger, and P. S. J. Russell, “Models for guidance in kagome-structured hollow-core photonic crystal fibres,” *Optics express*, vol. 15, no. 20, pp. 12680–12685, 2007.
- [19] Y. Wang, F. Couny, P. Roberts, and F. Benabid, “Low loss broadband transmission in optimized core-shape kagome hollow-core pcf,” in *Conference on Lasers and Electro-Optics*, p. CPDB4, Optical Society of America.
- [20] C. Wei, R. J. Weiblen, C. R. Menyuk, and J. Hu, “Negative curvature fibers,” *Advances in Optics and Photonics*, vol. 9, no. 3, pp. 504–561, 2017.
- [21] A. N. Kolyadin, A. F. Kosolapov, A. D. Pryamikov, A. S. Biriukov, V. G. Plotnichenko, and E. M. Dianov, “Light transmission in negative curvature hollow core fiber in extremely high material loss region,” *Optics express*, vol. 21, no. 8, pp. 9514–9519, 2013.
- [22] M. Michieletto, J. K. Lyngsø, C. Jakobsen, J. Lægsgaard, O. Bang, and T. T. Alkeskjold, “Hollow-core fibers for high power pulse delivery,” *Optics express*, vol. 24, no. 7, pp. 7103–7119, 2016.
- [23] F. Poletti, “Nested antiresonant nodeless hollow core fiber,” *Optics express*, vol. 22, no. 20, pp. 23807–23828, 2014.
- [24] Y. Wang, N. V. Wheeler, F. Couny, P. Roberts, and F. Benabid, “Low loss broadband transmission in hypocycloid-core kagome hollow-core photonic crystal fiber,” *Optics letters*, vol. 36, no. 5, pp. 669–671, 2011.
- [25] F. Yu and J. C. Knight, “Negative curvature hollow-core optical fiber,” *IEEE J. Sel. Top. Quantum Electron*, vol. 22, no. 2, pp. 146–155, 2016.

- [26] F. Yu, W. J. Wadsworth, and J. C. Knight, “Low loss silica hollow core fibers for 3–4 μ m spectral region,” *Optics express*, vol. 20, no. 10, pp. 11153–11158, 2012.
- [27] C. Wei, *Chalcogenide-glass Negative Curvature Fibers*. Thesis, 2018.
- [28] W. Belardi, “Design and properties of hollow antiresonant fibers for the visible and near infrared spectral range,” *Journal of Lightwave Technology*, vol. 33, no. 21, pp. 4497–4503, 2015.
- [29] T. D. Bradley, J. R. Hayes, Y. Chen, G. T. Jasion, S. R. Sandoghchi, R. Slavík, E. N. Fokoua, S. Bawn, H. Sakr, and I. A. Davidson, “Record low-loss 1.3 db/km data transmitting antiresonant hollow core fibre,” in *2018 European Conference on Optical Communication (ECOC)*, pp. 1–3, IEEE.
- [30] A. E. Akosman and M. Ordu, “Nested compound negative curvature hollow-core fiber for single-mode operation in the infrared region,” *Optics Communications*, p. 127194, 2021.
- [31] G. Alagashev, A. Pryamikov, A. Kosolapov, A. Kolyadin, A. Y. Lukovkin, and A. Biriukov, “Impact of geometrical parameters on the optical properties of negative curvature hollow-core fibers,” *Laser Physics*, vol. 25, no. 5, p. 055101, 2015.
- [32] W. Belardi and J. C. Knight, “Effect of core boundary curvature on the confinement losses of hollow antiresonant fibers,” *Optics Express*, vol. 21, no. 19, pp. 21912–21917, 2013.
- [33] M. S. Habib, O. Bang, and M. Bache, “Low-loss single-mode hollow-core fiber with anisotropic anti-resonant elements,” *Optics express*, vol. 24, no. 8, pp. 8429–8436, 2016.
- [34] A. Khan and M. Ordu, “Exploration of hybrid cladding elements in chalcogenide hollow-core fibers for low-loss mid-infrared transmission,” *Optik*, vol. 248, p. 168226, 2021.

- [35] M. Ordu, “Hollow-core optical fiber with eight-pointed star cladding structure for low-loss transmission in telecom bands,” *Turkish Journal of Physics*, vol. 45, no. 2, pp. 82–89, 2021.
- [36] H. Sakr, T. D. Bradley, G. T. Jasion, E. N. Fokoua, S. R. Sandoghchi, I. A. Davidson, A. Taranta, G. Guerra, W. Shere, and Y. Chen, “Hollow core nanfs with five nested tubes and record low loss at 850, 1060, 1300 and 1625nm,” in *Optical Fiber Communication Conference*, p. F3A. 4, Optica Publishing Group.
- [37] M. S. Habib, C. Markos, and R. Amezcua-Correa, “Impact of cladding elements on the loss performance of hollow-core anti-resonant fibers,” *Optics Express*, vol. 29, no. 3, pp. 3359–3374, 2021.
- [38] A. Khan and M. Ordu, “Mid-infrared negative curvature hollow-core fiber with elliptically nested tubular structure,” *Optics Communications*, p. 129227, 2022.
- [39] H. Sakr, Y. Chen, G. T. Jasion, T. D. Bradley, J. R. Hayes, H. C. H. Mulvad, I. A. Davidson, E. Numkam Fokoua, and F. Poletti, “Hollow core optical fibres with comparable attenuation to silica fibres between 600 and 1100 nm,” *Nature communications*, vol. 11, no. 1, pp. 1–10, 2020.
- [40] A. E. Akosman and M. Ordu, “Nested compound negative curvature hollow-core fiber for single-mode operation in the infrared region,” *Optics Communications*, vol. 497, p. 127194, 2021.
- [41] H. Liu, Y. Wang, Y. Zhou, Z. Guan, Z. Yu, Q. Ling, S. Luo, J. Shao, D. Huang, and D. Chen, “Low bending loss few-mode hollow-core anti-resonant fiber with glass-sheet conjoined nested tubes,” *Optics Express*, vol. 30, no. 12, pp. 21833–21842, 2022.
- [42] J. Bei, T. M. Monro, A. Hemming, and H. Ebendorff-Heidepriem, “Fabrication of extruded fluoroindate optical fibers,” *Optical Materials Express*, vol. 3, no. 3, pp. 318–328, 2013.

- [43] R. Kitamura, L. Pilon, and M. Jonasz, “Optical constants of silica glass from extreme ultraviolet to far infrared at near room temperature,” *Applied optics*, vol. 46, no. 33, pp. 8118–8133, 2007.
- [44] G. Tao, H. Ebendorff-Heidepriem, A. M. Stolyarov, S. Danto, J. V. Badding, Y. Fink, J. Ballato, and A. F. Abouraddy, “Infrared fibers,” *Advances in Optics and Photonics*, vol. 7, no. 2, pp. 379–458, 2015.
- [45] C. Wei, J. Hu, and C. R. Menyuk, “Comparison of loss in silica and chalcogenide negative curvature fibers as the wavelength varies,” *Frontiers in Physics*, vol. 4, p. 30, 2016.
- [46] F. Yu and J. C. Knight, “Limits of hollow core negative curvature fiber,” in *CLEO: 2013*, pp. 1–2, IEEE.
- [47] F. Yu and J. C. Knight, “Spectral attenuation limits of silica hollow core negative curvature fiber,” *Optics Express*, vol. 21, no. 18, pp. 21466–21471, 2013.
- [48] A. Ventura, J. G. Hayashi, J. Cimek, G. Jasion, P. Janicek, F. B. Slimen, N. White, Q. Fu, L. Xu, and H. Sakr, “Extruded tellurite antiresonant hollow core fiber for mid-ir operation,” *Optics Express*, vol. 28, no. 11, pp. 16542–16553, 2020.
- [49] A. F. Kosolapov, A. D. Pryamikov, A. S. Biriukov, V. S. Shiryaev, M. S. Astapovich, G. E. Snopatin, V. G. Plotnichenko, M. F. Churbanov, and E. M. Dianov, “Demonstration of co 2-laser power delivery through chalcogenide-glass fiber with negative-curvature hollow core,” *Optics express*, vol. 19, no. 25, pp. 25723–25728, 2011.
- [50] W. Belardi and P. J. Sazio, “Borosilicate based hollow-core optical fibers,” *Fibers*, vol. 7, no. 8, p. 73, 2019.
- [51] X. Huang, K.-T. Yong, and S. Yoo, “A method to process hollow-core anti-resonant fibers into fiber filters,” *Fibers*, vol. 6, no. 4, p. 89, 2018.
- [52] P. Jaworski, F. Yu, R. R. Maier, W. J. Wadsworth, J. C. Knight, J. D. Shephard, and D. P. Hand, “Picosecond and nanosecond pulse

- delivery through a hollow-core negative curvature fiber for micro-machining applications,” *Optics Express*, vol. 21, no. 19, pp. 22742–22753, 2013.
- [53] M. I. Hasan, *Antiresonant Guiding Hollow-core Fibers and Their Applications in Nonlinear Optics*. Thesis, 2019.
- [54] B. Debord, F. Amrani, L. Vincetti, F. Gérôme, and F. Benabid, “Hollow-core fiber technology: the rising of “gas photonics”,” *Fibers*, vol. 7, no. 2, p. 16, 2019.
- [55] S.-f. Gao, Y.-y. Wang, W. Ding, D.-l. Jiang, S. Gu, X. Zhang, and P. Wang, “Hollow-core conjoined-tube negative-curvature fibre with ultralow loss,” *Nature communications*, vol. 9, no. 1, pp. 1–6, 2018.
- [56] T. G. Polanyi, H. Bredemeier, and T. Davis, “A co2 laser for surgical research,” *Medical and biological engineering*, vol. 8, no. 6, pp. 541–548, 1970.
- [57] Y. Wang, M. Alharbi, T. D. Bradley, C. Fourcade-Dutin, B. Debord, B. Beaudou, F. Gerôme, and F. Benabid, “Hollow-core photonic crystal fibre for high power laser beam delivery,” *High Power Laser Science and Engineering*, vol. 1, no. 1, pp. 17–28, 2013.
- [58] Z. Wang, W. Belardi, F. Yu, W. J. Wadsworth, and J. C. Knight, “Efficient diode-pumped mid-infrared emission from acetylene-filled hollow-core fiber,” *Optics express*, vol. 22, no. 18, pp. 21872–21878, 2014.
- [59] F. Koch, S. Chernikov, and J. Taylor, “Dispersion measurement in optical fibres over the entire spectral range from 1.1 μm to 1.7 μm ,” *Optics communications*, vol. 175, no. 1-3, pp. 209–214, 2000.
- [60] G. T. Jasion, H. Sakr, J. R. Hayes, S. R. Sandoghchi, L. Hooper, E. N. Fokoua, A. Saljoghei, H. C. Mulvad, M. Alonso, and A. Taranta, “0.174 db/km hollow core double nested antiresonant nodeless fiber (dnanf),” in *2022 Optical Fiber Communications Conference and Exhibition (OFC)*, pp. 1–3, IEEE.

- [61] P. Jaworski, K. Krzempek, G. Dudzik, P. J. Sazio, and W. Belardi, “Nitrous oxide detection at 5.26 μm with a compound glass antiresonant hollow-core optical fiber,” *Optics letters*, vol. 45, no. 6, pp. 1326–1329, 2020.
- [62] P. Zhang, M. Tang, F. Gao, B. Zhu, Z. Zhao, L. Duan, S. Fu, J. Ouyang, H. Wei, and P. P. Shum, “Simplified hollow-core fiber-based fabry–perot interferometer with modified vernier effect for highly sensitive high-temperature measurement,” *IEEE Photonics Journal*, vol. 7, no. 1, pp. 1–10, 2015.
- [63] A. V. Nampoothiri, A. M. Jones, C. Fourcade-Dutin, C. Mao, N. Dadashzadeh, B. Baumgart, Y. Wang, M. Alharbi, T. Bradley, and N. Campbell, “Hollow-core optical fiber gas lasers (hofglas): a review,” *Optical Materials Express*, vol. 2, no. 7, pp. 948–961, 2012.
- [64] P. Zhao, Y. Zhao, H. Bao, H. L. Ho, W. Jin, S. Fan, S. Gao, Y. Wang, and P. Wang, “Mode-phase-difference photothermal spectroscopy for gas detection with an anti-resonant hollow-core optical fiber,” *Nature communications*, vol. 11, no. 1, pp. 1–8, 2020.
- [65] F. Aghbolagh, V. Nampoothiri, B. Debord, F. G er ome, L. Vincetti, F. Benabid, and W. Rudolph, “Mid ir hollow core fiber gas laser emitting at 4.6 μm ,” *Optics Letters*, vol. 44, no. 2, pp. 383–386, 2019.
- [66] P. S. J. Russell, P. H olzer, W. Chang, A. Abdolvand, and J. Travers, “Hollow-core photonic crystal fibres for gas-based nonlinear optics,” *Nature Photonics*, vol. 8, no. 4, pp. 278–286, 2014.
- [67] M. R. A. Hassan, F. Yu, W. J. Wadsworth, and J. C. Knight, “Cavity-based mid-ir fiber gas laser pumped by a diode laser,” *Optica*, vol. 3, no. 3, pp. 218–221, 2016.
- [68] Y. Wang, M. K. Dasa, A. I. Adamu, J. Antonio-Lopez, M. S. Habib, R. Amezcua-Correa, O. Bang, and C. Markos, “High pulse energy and quantum efficiency mid-infrared gas raman fiber laser targeting CO_2 ,” *Optics Letters*, vol. 43, no. 12, pp. 2800–2803, 2018.

absorption at 4.2 μm ,” *Optics Letters*, vol. 45, no. 7, pp. 1938–1941, 2020.

- [69] E. Lee, J. Luo, B. Sun, V. L. Ramalingam, X. Yu, Q. Wang, F. Yu, and J. C. Knight, “45w 2 m nanosecond pulse delivery using antiresonant hollow-core fiber,” in *2018 Conference on Lasers and Electro-Optics (CLEO)*, pp. 1–2, IEEE.
- [70] S. Wu, B. Siwicki, R. M. Carter, F. Biancalana, J. D. Shephard, and D. P. Hand, “Impact of nonlinear effects on transmission losses of hollow-core antiresonant negative curvature optical fiber,” *Applied Optics*, vol. 59, no. 16, pp. 4988–4996, 2020.
- [71] F. Yu, M. Cann, A. Brunton, W. Wadsworth, and J. Knight, “Single-mode solarization-free hollow-core fiber for ultraviolet pulse delivery,” *Optics express*, vol. 26, no. 8, pp. 10879–10887, 2018.
- [72] B. Debord, M. Alharbi, L. Vincetti, A. Husakou, C. Fourcade-Dutin, C. Hoenninger, E. Mottay, F. G er ome, and F. Benabid, “Multi-meter fiber-delivery and pulse self-compression of milli-joule femtosecond laser and fiber-aided laser-micromachining,” *Optics express*, vol. 22, no. 9, pp. 10735–10746, 2014.
- [73] S. Amini-Nik, D. Kraemer, M. L. Cowan, K. Gunaratne, P. Nadesan, B. A. Alman, and R. D. Miller, “Ultrafast mid-ir laser scalpel: protein signals of the fundamental limits to minimally invasive surgery,” *PLoS one*, vol. 5, no. 9, p. e13053, 2010.
- [74] G.-C. Hazel, *Novel (Trans) dermal drug delivery strategies: micro-and nano-scale assessments*. Springer, 2016.
- [75] A. Urich, R. R. J. Maier, F. Yu, J. C. Knight, D. P. Hand, and J. D. Shephard, “Flexible delivery of er: Yag radiation at 2.94 μm with negative curvature silica glass fibers: a new solution for minimally invasive surgical procedures,” *Biomedical optics express*, vol. 4, no. 2, pp. 193–205, 2013.

- [76] Y. P. Yatsenko, A. A. Krylov, A. D. Pryamikov, A. F. Kosolapov, A. N. Kolyadin, A. V. Gladyshev, and I. Bufetov, “Propagation of femtosecond pulses in a hollow-core revolver fibre,” *Quantum Electronics*, vol. 46, no. 7, p. 617, 2016.
- [77] F. Kapron, D. B. Keck, and R. D. Maurer, “Radiation losses in glass optical waveguides,” *Applied Physics Letters*, vol. 17, no. 10, pp. 423–425, 1970.
- [78] S. Kang, G. Dong, J. Qiu, and Z. Yang, “Hybrid glass optical fibers—novel fiber materials for optoelectronic application,” *Optical Materials: X*, vol. 6, p. 100051, 2020.
- [79] G. Keiser, F. Xiong, Y. Cui, and P. P. Shum, “Review of diverse optical fibers used in biomedical research and clinical practice,” *Journal of biomedical optics*, vol. 19, no. 8, p. 080902, 2014.
- [80] Y. Koike and K. Koike, *Optical Fibers*, pp. 283–304. Elsevier, 2012.
- [81] K. Tsujikawa, K. Tajima, and J. Zhou, “Intrinsic loss of optical fibers,” *Optical Fiber Technology*, vol. 11, no. 4, pp. 319–331, 2005.
- [82] I. M. Ankan, M. A. Mollah, J. Sultana, and M. S. Islam, “Negative curvature hollow-core anti-resonant fiber for terahertz sensing,” *Applied Optics*, vol. 59, no. 28, pp. 8519–8525, 2020.
- [83] N. Dadashzadeh, M. P. Thirugnanasambandam, H. K. Weerasinghe, B. Debord, M. Chafer, F. Gerome, F. Benabid, B. R. Washburn, and K. L. Corwin, “Near diffraction-limited performance of an opa pumped acetylene-filled hollow-core fiber laser in the mid-ir,” *Optics Express*, vol. 25, no. 12, pp. 13351–13358, 2017.
- [84] C. Wei, C. R. Menyuk, and J. Hu, “Geometry of chalcogenide negative curvature fibers for co2 laser transmission,” *Fibers*, vol. 6, no. 4, p. 74, 2018.

- [85] N. Wheeler, T. Bradley, J. Hayes, M. Gouveia, S. Liang, Y. Chen, S. Sandoghchi, S. A. Mousavi, F. Poletti, and M. Petrovich, “Low-loss kagome hollow-core fibers operating from the near-to the mid-ir,” *Optics Letters*, vol. 42, no. 13, pp. 2571–2574, 2017.
- [86] R. R. Gattass, D. Rhonehouse, D. Gibson, C. C. McClain, R. Thapa, V. Q. Nguyen, S. S. Bayya, R. J. Weiblen, C. R. Menyuk, and L. B. Shaw, “Infrared glass-based negative-curvature anti-resonant fibers fabricated through extrusion,” *Optics express*, vol. 24, no. 22, pp. 25697–25703, 2016.
- [87] S. Cui, R. Chahal, C. Boussard-Plédel, V. Nazabal, J.-L. Doualan, J. Troles, J. Lucas, and B. Bureau, “From selenium-to tellurium-based glass optical fibers for infrared spectroscopies,” *Molecules*, vol. 18, no. 5, pp. 5373–5388, 2013.
- [88] P. Lucas, M. R. Riley, C. Boussard-Plédel, and B. Bureau, “Advances in chalcogenide fiber evanescent wave biochemical sensing,” *Analytical biochemistry*, vol. 351, no. 1, pp. 1–10, 2005.
- [89] J. S. Sanghera, L. B. Shaw, and I. D. Aggarwal, “Applications of chalcogenide glass optical fibers,” *Comptes Rendus Chimie*, vol. 5, no. 12, pp. 873–883, 2002.
- [90] J. Carcreff, F. Cheviré, E. Galdo, R. Lebullenger, A. Gautier, J. L. Adam, D. Le Coq, L. Brilland, R. Chahal, and G. Renversez, “Mid-infrared hollow core fiber drawn from a 3d printed chalcogenide glass preform,” *Optical Materials Express*, vol. 11, no. 1, pp. 198–209, 2021.
- [91] J. Carcreff, F. Cheviré, R. Lebullenger, A. Gautier, R. Chahal, J. L. Adam, L. Calvez, L. Brilland, E. Galdo, and D. Le Coq, “Investigation on chalcogenide glass additive manufacturing for shaping mid-infrared optical components and microstructured optical fibers,” *Crystals*, vol. 11, no. 3, p. 228, 2021.
- [92] V. Shiryaev, A. Kosolapov, A. Pryamikov, G. Snopatin, M. Churbanov, A. Biriukov, T. Kotereva, S. Mishinov, G. Alagashev, and

- A. Kolyadin, “Development of technique for preparation of as₂s₃ glass preforms for hollow core microstructured optical fibers,” *J. Optoelectron. Adv. Mater.*, vol. 16, no. 9-10, pp. 1020–1025, 2014.
- [93] J. Tu, B. Zhang, Z. Liu, X. Zhou, K. Long, Z. Li, C. Lu, and C. Yu, “Chalcogenide-glass nested anti-resonant nodeless fibers in mid-infrared region,” *Journal of Lightwave Technology*, vol. 36, no. 22, pp. 5244–5253, 2018.
- [94] A. D. Pryamikov, A. S. Biriukov, A. F. Kosolapov, V. G. Plotnichenko, S. L. Semjonov, and E. M. Dianov, “Demonstration of a waveguide regime for a silica hollow-core microstructured optical fiber with a negative curvature of the core boundary in the spectral region λ 3.5 μ m,” *Optics express*, vol. 19, no. 2, pp. 1441–1448, 2011.
- [95] F.-C. Meng, B.-W. Liu, Y.-F. Li, C.-Y. Wang, and M.-L. Hu, “Low loss hollow-core antiresonant fiber with nested elliptical cladding elements,” *IEEE Photonics Journal*, vol. 9, no. 1, pp. 1–11, 2016.
- [96] M. S. Habib, J. Antonio-Lopez, C. Markos, A. Schülzgen, and R. Amezcua-Correa, “Single-mode, low loss hollow-core anti-resonant fiber designs,” *Optics express*, vol. 27, no. 4, pp. 3824–3836, 2019.
- [97] M. I. Hasan, N. Akhmediev, and W. Chang, “Positive and negative curvatures nested in an antiresonant hollow-core fiber,” *Optics Letters*, vol. 42, no. 4, pp. 703–706, 2017.
- [98] K. S. R. Shaha, A. Khaleque, and I. Hasan, “Low loss double cladding nested hollow core antiresonant fiber,” *OSA Continuum*, vol. 3, no. 9, pp. 2512–2524, 2020.
- [99] K. S. R. Shaha, A. Khaleque, and M. S. Hosen, “Wideband low loss hollow core fiber with nested hybrid cladding elements,” *Journal of Lightwave Technology*, vol. 39, no. 20, pp. 6585–6591, 2021.
- [100] J. Zhang, J. Cao, B. Yang, X. Liu, Y. Cheng, C. Bao, S. Xie, L. Dong, and Q. Hao, “Ultralow loss hollow-core negative curvature fibers with

- nested elliptical antiresonance tubes,” *Optics Express*, vol. 30, no. 10, pp. 17437–17450, 2022.
- [101] A. Khan and M. Ordu, “Effect of the nested elements to the confinement losses in chalcogenide hollow-core fibers,” in *2021 IEEE Photonics Conference (IPC)*, pp. 1–2, IEEE.
- [102] L. Zhang, A. M. Agarwal, L. C. Kimerling, and J. Michel, “Nonlinear group iv photonics based on silicon and germanium: from near-infrared to mid-infrared,” *Nanophotonics*, vol. 3, no. 4-5, pp. 247–268, 2014.
- [103] S. Gao, Y. Wang, and P. Wang, “Silica-based nodeless hollow-core fiber for broadband mid-ir guidance,” in *Conference on Lasers and Electro-Optics/Pacific Rim*, p. s2024, Optica Publishing Group.
- [104] F. Yu, P. Song, D. Wu, T. Birks, D. Bird, and J. Knight, “Attenuation limit of silica-based hollow-core fiber at mid-ir wavelengths,” *APL Photonics*, vol. 4, no. 8, p. 080803, 2019.
- [105] I. A. Davidson, S. Rikimi, H. Sakr, G. T. Jasion, T. D. Bradley, N. V. Wheeler, F. Poletti, and D. J. Richardson, “Anti-resonant, mid-infrared silica hollow-core fiber,” in *Specialty Optical Fibers*, p. SoW1H. 7, Optical Society of America.
- [106] C. Wei, J. Hu, and C. R. Menyuk, “Comparison of loss in silica and chalcogenide negative curvature fibers as the wavelength varies,” *Frontiers in Physics*, vol. 4, p. 30, 2016.
- [107] L. Vincetti and V. Setti, “Waveguiding mechanism in tube lattice fibers,” *Optics express*, vol. 18, no. 22, pp. 23133–23146, 2010.
- [108] S. M. A. Mousavi, *Exploring Optical Nonlinearity In Gas-Filled Hollow Core Fibers*. Thesis, 2018.
- [109] T. White, B. Kuhlmeier, R. McPhedran, D. Maystre, G. Renversez,

- C. M. De Sterke, and L. Botten, “Multipole method for microstructured optical fibers. i. formulation,” *JOSA B*, vol. 19, no. 10, pp. 2322–2330, 2002.
- [110] P. Klocek, *Handbook of infrared optical materials*. CRC Press, 2017.
- [111] Y. Wang, M. I. Hasan, M. R. A. Hassan, and W. Chang, “Effect of the second ring of antiresonant tubes in negative-curvature fibers,” *Optics express*, vol. 28, no. 2, pp. 1168–1176, 2020.
- [112] F. Poletti, J. Hayes, and D. Richardson, “Optimising the performances of hollow antiresonant fibres,” in *European Conference and Exposition on Optical Communications*, p. Mo. 2. LeCervin. 2, Optica Publishing Group.
- [113] C. Caillaud, G. Renversez, L. Brilland, D. Mechin, L. Calvez, J.-L. Adam, and J. Troles, “Photonic bandgap propagation in all-solid chalcogenide microstructured optical fibers,” *Materials*, vol. 7, no. 9, pp. 6120–6129, 2014.
- [114] T. Grigorova, R. Sollapur, A. Hoffmann, D. Kartashov, M. Zürich, A. Härtung, A. Schwuchow, J. Bierlich, J. Kobelke, and M. Schmidt, “Dispersion measurement of engineered antiresonant hollow-core fibers with spectral interferometry,” in *2017 Conference on Lasers and Electro-Optics Europe & European Quantum Electronics Conference (CLEO/Europe-EQEC)*, pp. 1–1, IEEE.
- [115] G. P. Agrawal, *Nonlinear fiber optics*, pp. 195–211. Springer, 2000.
- [116] K. Saitoh and M. Koshiba, “Leakage loss and group velocity dispersion in air-core photonic bandgap fibers,” *Optics Express*, vol. 11, no. 23, pp. 3100–3109, 2003.
- [117] S.-F. Gao, Y.-Y. Wang, X.-L. Liu, W. Ding, and P. Wang, “Bending loss characterization in nodeless hollow-core anti-resonant fiber,” *Optics express*, vol. 24, no. 13, pp. 14801–14811, 2016.

- [118] J. A. Buck, *Fundamentals of optical fibers*, vol. 50. John Wiley & Sons, 2004.
- [119] R. Gao, D.-F. Lu, M. Zhang, and Z.-M. Qi, “Vibration sensor based on the resonance power leakage in a tapered capillary fiber,” *IEEE Sensors Journal*, vol. 17, no. 24, pp. 8332–8337, 2017.
- [120] R. Gao and J. Ye, *The antiresonant reflecting optical waveguide fiber sensor*. IntechOpen, 2020.
- [121] A. Zheltikov, “Ray-optic analysis of the (bio) sensing ability of ring-cladding hollow waveguides,” *Applied optics*, vol. 47, no. 3, pp. 474–479, 2008.
- [122] S. Liu, Y. Wang, M. Hou, J. Guo, Z. Li, and P. Lu, “Anti-resonant reflecting guidance in alcohol-filled hollow core photonic crystal fiber for sensing applications,” *Optics Express*, vol. 21, no. 25, pp. 31690–31697, 2013.
- [123] G. T. Jasion, J. R. Hayes, N. V. Wheeler, Y. Chen, T. D. Bradley, D. J. Richardson, and F. Poletti, “Fabrication of tubular anti-resonant hollow core fibers: modelling, draw dynamics and process optimization,” *Optics Express*, vol. 27, no. 15, pp. 20567–20582, 2019.
- [124] A. F. Kosolapov, G. K. Alagashev, A. N. Kolyadin, A. D. Pryamikov, A. Biryukov, I. Bufetov, and E. M. Dianov, “Hollow-core revolver fibre with a double-capillary reflective cladding,” *Quantum Electronics*, vol. 46, no. 3, p. 267, 2016.
- [125] L. R. Murphy, S. Yerolatsitis, T. A. Birks, and J. M. Stone, “Stack, seal, evacuate, draw: a method for drawing hollow-core fiber stacks under positive and negative pressure,” *Optics Express*, vol. 30, no. 21, pp. 37303–37313, 2022.

Appendix A

Code

The following simple MATLAB code is used to find the GVD curves in Figure 4.6 from the fitted effective refractive index curves.

```
clc
clear
filename = uigetfile('file.xlsx');
data = readmatrix(filename);
wavelength = (data(:,1))*1e-6;
index = real(data(:,2));
c = 2.99792458e8;
wavelength-fine = linspace(wavelength(1,1),wavelength(size(wavelength,1)),300)';
N = 5;
fit = polyfit(wavelength, index,N);
fit2 = polyder(fit);
fit3 = polyder(fit2);
gvd = -(wavelength-fine/c).*(polyval(fit3,wavelength-fine));
hold on
figure(1)
```

```
plot(wavelength-fine*1e6,gvd.*(1e6))
title('Group Velocity Dispersion (GVD)')
xlabel('Wavelength (um)')
ylabel('GVD (ps/nm/km)')
legend(filename);
```